Dissertation
submitted to the
Combined Faculties for the Natural Sciences and for Mathematics
of the Ruperto-Carola University of Heidelberg, Germany
for the degree of
Doctor of Natural Sciences

presented by

Michael Albiez
born in: Freiburg i.Br., Germany

Oral examination: October 19, 2005

Observation of nonlinear tunneling of a Bose-Einstein condensate in a single Josephson junction

Referees: Prof. Dr. Markus K. Oberthaler
Prof. Dr. Jörg Schmiedmayer

Beobachtung von nichtlinearer Tunneldynamik eines Bose-Einstein Kondensates in einem Josephsonkontakt

In der vorliegenden Arbeit wird die erste experimentelle Realisierung eines Josephsonkontaktes für Bose-Einstein Kondensate beschrieben. Das physikalische System zweier schwach gekoppelter BECs steht in enger Analogie zu den bekannten Josephsonkontakten in Supraleitern und Suprafluiden. Die schwache Kopplung wird in unserem Experiment mit Hilfe eines optischen Doppelmuldenpotentials realisiert, in das das BEC hinein geladen wird. Es entsteht durch die Superposition eines eindimensionalen optischen Gitters und zweier gekreuzter fokussierten Laserstrahls, die einen dreidimensionalen harmonischen Einschluß erzeugt. Die Tunneldynamik in diesem bosonischen Josephson Kontakt zeigt zwei deutlich unterscheidbare dynamische Regimes. Für kleine anfängliche Besetzungzahlunterschiede der beiden Potentialminima werden nahezu sinusförmige Josephson-Oszillationen beobachtet, die sowohl durch eine oszillierende Besetzung als auch durch eine oszillierende relative Phase der beiden BECs charakterisiert ist. Wird der anfängliche Besetzungsunterschied größer gewählt als ein kritischer Wert, beobachtet man, daß sich die Besetzung im Laufe der Zeit kaum mehr ändert, wohingegen die relative Phase der beiden Wellenpakete linear anwächst. Dieses dynamische Verhalten, das als „macroscopic self-trapping“bezeichnet wird, wird dadurch verursacht, daß resonantes Tunneln aufgrund stark unterschiedlicher Wechselwirkungsenergien in den beiden Potentialtöpfen unterdrückt ist und hat keine direkte Analogie in supraleitenden Josephsonkontakten.

Observation of nonlinear tunneling of a Bose-Einstein condensate in a single Josephson junction

In this thesis, I present the first experimental implementation of a Josephson junction for Bose-Einstein condensates. The weak link between two BECs constitutes the nonlinear generalization of the well known Josephson junction of weakly-coupled superconductors that are separated by a thin insulating barrier. In our experiment, the required overlap of two macroscopic wavefunctions is provided by loading a BEC into an optical double well potential. It is realized by a superposition of a one-dimensional optical lattice with a focused laser beam optical dipole trap. The tunneling dynamics between the two potential wells exhibits two distinct dynamical regimes. For small initial population imbalances of the two wells we observe nearly sinusoidal Josephson tunneling oscillations, which are characterized by an oscillating population and relative phase. The situation changes drastically, if the initial population imbalance is chosen above a critical value. In this case, resonant tunneling between the two wells is prohibited because the difference between the on-site particle interaction energies in the two wells exceeds the tunneling energy splitting. As a consequence, the atomic distribution becomes self-locked and the relative phase evolves unbound in time. This regime of prohibited tunneling, which has no analogon in superconducting Josephson junctions, is called “macroscopic quantum self-trapping”.

To Karen, Clara and Luca.

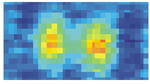

Contents

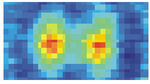

1 Introduction

One of the most prominent and striking features of quantum mechanics is the tunneling of massive particles through classically forbidden regions. Although tunneling is a purely quantum mechanical effect, it can be observed on a macroscopic scale in a system described by two weakly linked macroscopic wavefunctions with global phase coherence. This macroscopic tunneling, which is referred to as the "Josephson effect", was predicted by Brian D. Josephson in 1962 [1], who was rewarded the nobel price in physics in 1973.

The first experimental evidence of the corresponding current-phase relation has already been observed in 1963 [2] in a superconducting Josephson junction, which is a device consisting of two coupled superconductors separated by a thin insulating barrier. The discovery of the Josephson effect opened not only a new important chapter of physics but also new horizons for a wide variety of applications [3]. Nowadays Josephson junctions are used for example in SQUIDS (Superconducting Quantum Interference Devices) which allow to measure extremely small magnetic fields with a resolution on the order of $10^{-14}\,\mathrm{T}$.

The theory of the Josephson effect was developed in the context of superconductors but can nevertheless be applied to all physical systems described by weakly coupled macroscopic wavefunctions. Due to the difficulty of creating a weak link between two neutral superfluids, the Josephson effect in superfluid helium has only been observed in 1997 [4]. In those experiments, the weak link between two macroscopic wavefunctions was realized by means of a membrane with nanoscopic holes.

In this thesis, the first experimental implementation of a single Josephson junction in a new experimental system, which can be described by phase-coherent macroscopic wavefunctions, is presented: macroscopic tunneling in Bose-Einstein condensates.

Nonlinear macroscopic quantum mechanics

Based on the quantum statistical description of indistinguishable bosonic particles by Satyendra Nath Bose [5], Einstein predicted a quantum phase transition to a fascinating new state of matter [6]. This transition occurs, when the de Broglie wavelength of the atoms becomes comparable to the distance between the atoms. The successful achievement of this so-called Bose-Einstein condensation (BEC) in a dilute gas in 1995 [7, 8, 9] was made possible by the development of novel cooling techniques - laser cooling and evaporative cooling of neutral atoms. The transition to the quantum-degenerate regime allows for studying matter at the level of a single macroscopically occupied quantum state. This provides a new source of coherent macroscopic matterwaves, which can be regarded as an ideal state for studies and applications of quantum mechanics. Bose-Einstein condensates of weakly interacting alkali atoms allow the investigation of neutral superfluids in a controlled and experimentally tunable environment. Nowadays, Bose-

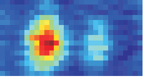

Einstein condensates of alkali atoms are routinely generated in many laboratories all over the world.

A striking feature of Bose-Einstein condensates is their coherent nature on the micrometer scale. This phase coherence has been impressively demonstrated in the first interference experiments at the MIT [10] where two independent Bose-Einstein condensates were created in a double well potential, realized by focussing a blue detuned laser beam into the center of the confining magnetic trap. After turning off all traps the two BECs expand and start to overlap forming clear atomic interference patterns.

Many interesting properties of BECs result from the atom-atom interaction that can be either attractive or repulsive. Combined with the ability to manipulate BECs with magnetic and optical potentials, this opened up the way to many outstanding experiments [11]. The peculiarity of these trapped alkali vapors is that their densities are sufficiently low to be treated in the framework of the well established theory of weakly interacting Bose gases. This description provides a simple language to explain most of the so far performed experiments with BECs in terms of a few physical quantities.

The new field of nonlinear matter wave optics is a highly interdisciplinary branch of physics which is closely connected to statistical mechanics, atomic physics, photon optics and solid state physics. The realization of atom lasers [12] for example has pointed out analogies to photon optics. Nonlinear optics, where the nonlinear Kerr effect strongly affects the propagation of intense light pulses through optical fibers, found its parallel in atom-optics by the creation of dark [13] and bright [14, 15, 16] matter wave solitons. These non-spreading localized wavepackets form, if the linear dispersion of the atoms is canceled by the nonlinear particle interaction. Additionally, parallels to condensed matter physics have been demonstrated by the observation of vortices in a stirred Bose-Einstein condensate [17].

Bose-Einstein condensates in optical lattices

During the last years, the dynamical behavior of Bose-Einstein condensates in optical lattices has been intensely investigated theoretically and experimentally. As known from solid state physics, electrons in periodic potentials exhibit a modified dispersion relation. The concepts developed in solid state theory can be directly transferred to the description of Bose-Einstein condensates in optical lattices. This analogy has been confirmed by the observation of Bloch-oscillations [18], Wannier-Stark ladders [19], Bragg-scattering [20] [21] and Landau-Zener tunneling [22] for Bose-Einstein condensates. At the beginning of my PhD period, we have implemented "dispersion management" [23, 24] for atomic matterwaves, which has allowed for the creation of bright atomic gap solitons of atoms with repulsive interaction [16]. The highlight of the experiments with Bose-Einstein condensates in optical lattices was the observation of the quantum phase transition from a superfluid to a Mott insulating phase of atoms [25], which directly shows the analogies to solid state physics.

Josephson effect in Bose-Einstein condensates

The first observation of a Josephson atomic current in a one-dimensional Josephson junction array formed by a deep optical lattice has been reported in [26]. However, because of the small spacing of approximately 400 nm of the individual Josephson junctions, the

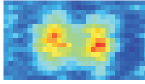

dynamics of a single junction could not be resolved experimentally. This restricted the observation to a measurement of the center of mass oscillations inside the superimposed harmonic trap and to a continuous probing of the phase coherence of the system. Recently, we have observed the nonlinear effect of self-trapping in a Josephson junction array [27] with a similar experimental setup.

In order to investigate the direct analogon of a superconducting Josephson junction, one has to implement a single weak link between two Bose-Einstein condensates. This can be done in two different experimental systems. The most straight forward realization of the weak coupling is loading a BEC into a double well potential which provides a small wavefunction overlap (external Josephson effect). This physical system has been extensively studied theoretically [28, 29, 30, 31, 32, 33, 34].

Additionally, Josephson effects have also been predicted to exist in a system of two BECs in different hyperfine levels trapped in a single harmonic trap in the presence of a weak driving field that couples these hyperfine states [35, 36] (internal Josephson effect).

The effect of macroscopic tunneling in a single bosonic Josephson junction manifests itself in a coherent exchange of atoms between the two wells or correspondingly between the two hyperfine states. If a BEC is loaded into a double well potential with a small initial population imbalance, it can oscillate between the wells by quantum mechanical tunneling. This regime of Josephson oscillation is characterized by an oscillating population and relative phase around a zero mean value. However, due to the nonlinearity arising from particle interactions, new dynamical tunneling regimes are predicted in a weak link of two Bose-Einstein condensates. The most striking effect is the inhibition of tunneling oscillations between the two wells, if the initial population imbalance is chosen above a critical value. In this case, resonant tunneling between the particles on each side of the barrier is prohibited because the difference of the interaction energy between the two components exceeds the tunneling energy splitting. Therefore, the atomic distribution is self-locked inside a single well, and the relative phase of the two wavepackets increases unbound. This new dynamical regime is called "macroscopic quantum self-trapping". It has no direct analogon in superconducting Josephson junctions, where nonlinear self-interaction effects can generally be neglected because of the small fraction of 10^{-10} of tunneling Cooper pairs compared to the total number of electrons.

Double well potentials for Bose-Einstein condensates have been created in time-orbiting magnetic traps [37], by a combination of two focused red detuned laser beams [38] and on atom chips [39]. It has recently been shown that Bose-Einstein condensates in a double well potential can be prepared with a fixed phase-relation [40] (each realization of the experiment reproduces the same relative phase), which is a prerequisite for the experimental observation of macroscopic quantum tunneling. However, up to now nobody has succeeded in observing the Josephson effect between two weakly coupled Bose-Einstein condensates. The main reason is that in order to realize tunneling times on an observable timescale on the order of 100 ms, the distance of the two wells has to be on the scale of a few micrometers [40]. For usual atom numbers of several ten thousand atoms, working with such small traps implies that the dynamics is always meanfield dominated which inhibits the occurrence of Josephson tunneling between the two wells. In principle, Feshbach resonances[41] could be used to tune the strength of interatomic interaction in order to make Josephson tunneling observable. However, they are difficult to implement experimentally for the case of ^{87}Rb [42].

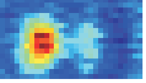

In our experiment, we prepare ^{87}Rb BECs consisting of approximately 1000 atoms in a double well potential with a well-spacing of $4.4\,\mu$m. The stable experimental setup combined with the optical resolution of $2.7(2)\,\mu$m of our imaging system makes it possible for the first time to observe Josephson tunneling in a single bosonic Josephson junction. This experiment is a generalization of the familiar superconducting Josephson contact and reveals new insight into the well known tunneling dynamics. Since the relative phase between two BECs can be directly deduced by observing atomic interference fringes, the full complex macroscopic wavefunction can be determined experimentally. Both dynamical regimes - Josephson tunneling and macroscopic quantum self-trapping - are experimentally accessible. In the presented experiments, the quantum mechanical effect of tunneling is indeed *macroscopic* in a sense that the tunneling of massive particles can be observed directly by means of a simple optical imaging system.

Outline of this thesis

This thesis consists of three sections: an introductory part (chapter 2), a theoretical part (chapter 3) and a technical and experimental part (chapters 4, 5 and 6).

Chapter 2 gives a fundamental description of the physics of two weakly coupled macroscopic wavefunctions and a short introduction to Josephson effects in superconductors and superfluids. Chapter 3 treats the theoretical description of Josephson junctions for Bose-Einstein condensates. After a short introduction to the general theory of Bose-Einstein condensates, the two-mode approximation for a BEC in a double well potential is presented. Subsequently, an extended two-mode model will be discussed and compared to the results of a numerical integration of the Schrödinger equation. The experimental procedure and the setup for cooling ^{87}Rb atoms to quantum degeneracy and preparing the Bose-Einstein condensate in a double well potential is described in chapter 4. At this I have focused on the active stabilization of the optical potentials that is crucial for the realization of a bosonic Josephson junction. In Chapter 5, the experimental results on macroscopic tunneling of Bose-Einstein condensates are presented. Experiments that have been performed during the first two years of my PhD period are presented in chapter 6. The results of four publications are discussed: dispersion management and continuous dispersion management in weak periodic potentials, the observation of bright atomic gap solitons and the transition from the tunneling to the self-trapping regime in a one-dimensional optical lattice. Finally, the conclusion and an outlook to feasible future experiments, which can be performed with the current setup is given in chapter 7.

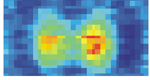

2 Josephson effect in superconductors and superfluids

The phenomenon of superconductivity was first observed by Heike Kamerlingh Onnes in 1911. He succeeded in producing liquid Helium at a temperature of 4.2 K in 1908 and was able to subsequently cool other materials down to 1.7 K. When measuring the electric resistance of mercury, he observed a phenomenon which was incompatible with the state of knowledge of solid state physics. At that time, the behavior of the electrical resistance close to zero temperature was extensively and controversially discussed. Lord Kelvin of Largs (1824-1907) predicted an infinite resistance at $T = 0$ assuming that electronic motion freezes in at low temperatures. In contrast, Heinrich Matthiessen (1830-1906) predicted a finite resistance and Heike Kamerlingh Onnes supposed an asymptotic decrease to zero.

When he cooled mercury with liquid Helium, the resistance decreased at first continuously as predicted by solid-state theory. But at a temperature of 4.2 K it changed abruptly to a non-measurable level as shown in figure 2.1. Kamerlingh Onnes called this phenomenon superconductivity and the corresponding temperature critical temperature.

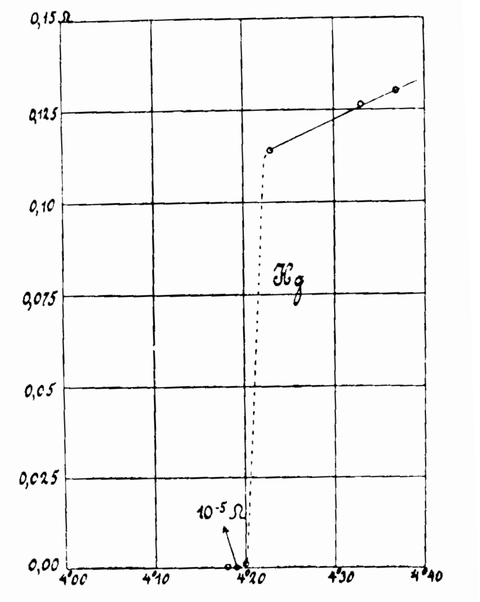

Figure 2.1: First observation of superconductivity in mercury cooled by superfluid helium (Leiden 1911, from [43]).

Only twenty years after the observation of superconductivity, theoreticians came up

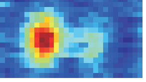

with first theoretical models. The interpretation of superconductivity as a macroscopic quantum phenomenon was proposed by F. London in 1935 [44]. Ginzburg and Landau [45] developed a modification of the London theory by introducing a complex parameter Ψ which is the quantum mechanical wavefunction of superconducting electrons. This single wavefunction describes a macroscopic number of electrons which are assumed to "condense" into the same macroscopic quantum state. They succeeded in expanding the theory of thermodynamic phase transitions which allowed to explain all fundamental features of superconductivity.

The microscopic basis and a quantum mechanical description of superconductivity was first developed in 1957 by Bardeen, Cooper and Schrieffer in the framework of the BCS theory [46]. Within this approach, the effect of superconductivity is attributed to the existence of paired electrons, so-called Cooper pairs. The electron-electron attraction leading to this pairing arises from electron-phonon interaction, which is required to be larger than the inter-electronic Coulomb repulsion. In contrast to single electrons, Cooper pairs have an integer spin and therefore obey Bose-Einstein statistics instead of Fermi-Dirac statistics, which explains the existence of a single macroscopic quantum mechanical wavefunction. Within the framework of the BCS theory, the existence of supercurrents (currents without resistance) is explained by the appearance of a finite energy gap in the excitation spectrum of Cooper pairs. This gap corresponds to the Cooper pair binding energy which is typically on the order of a few meV.

One of the most important features of superconductors is the phase correlation which means that the quantum mechanical phase is constant over the whole superconductor allowing for macroscopic tunneling as we will see in the following section.

2.1 Fundamental description of Josephson tunneling: the Josephson equations

A Josephson junction consists of two superconducting electrodes separated by a thin insulating barrier. For a barrier thickness of more than typically 30 Å, no electronic transport between the two superconductors takes place. When reducing the barrier thickness to 30 Å, single electrons can tunnel and the barrier basically acts as an electrical resistance between the two superconductors. If the thickness of the barrier is further reduced to typically 10 Å or below, the quantum mechanical macroscopic wavefunctions of the two superconductors begin to overlap within the classically forbidden region. This system is often referred to as weak link of two superconductors. In a semi-classical particle model, this overlap corresponds to Cooper pair transport from one superconductor to the other, a phenomenon called Josephson tunneling. This macroscopic tunneling effect was theoretically predicted [1] by the graduate student Brian D. Josephson who investigated weak links of superconductors at the University of Cambridge in 1962.

In these Josephson junctions the phase correlation is transmitted through the dielectric barrier leading to supercurrents without any electrical resistance, i.e. without any voltage drop across the barrier. The phenomenon of tunneling in a Josephson junction is therefore often called "weak superconductivity". For details on geometry and fabrication of the various junction types I refer to [47].

In deriving the basic Josephson equations I follow the approach of Feynman [48], which can also be found in superconductor textbooks [3, 43, 49]. Let us consider two superconductors S_L and S_R separated by an insulating barrier as shown in figure 2.2.

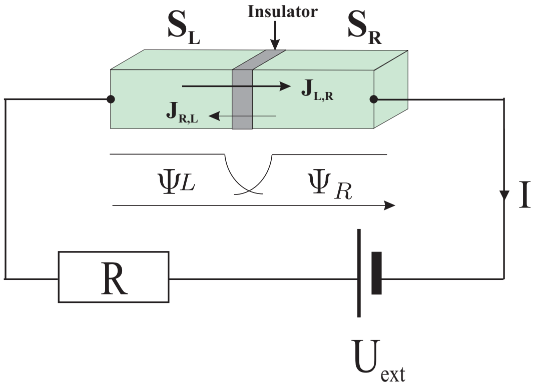

Figure 2.2: Superconducting tunnel junction provided by a thin insulating layer with a typical thickness of 1 nm between two superconductors S_L and S_R. J_{LR} and J_{RL} denote the tunneling current densities in both directions. The weakly overlapping macroscopic wavefunctions are indicated by Ψ_L and Ψ_R. Tunneling Cooper pairs are replaced by the external current source, which therefore suppresses charge-imbalances across the junction.

If the barrier is thick enough so that the two superconductors are insulated, the Schrödinger equation for each macroscopic wavefunction reads

$$\begin{aligned} i\hbar\frac{\partial}{\partial t}\Psi_L &= E_L\Psi_L \\ i\hbar\frac{\partial}{\partial t}\Psi_R &= E_R\Psi_R. \end{aligned} \tag{2.1}$$

In the presence of a weak coupling between the superconductors the two equations couple via an additional tunneling energy term

$$\begin{aligned} i\hbar\frac{\partial}{\partial t}\Psi_L &= E_L\Psi_L + K\Psi_R \\ i\hbar\frac{\partial}{\partial t}\Psi_R &= E_R\Psi_R + K\Psi_L, \end{aligned} \tag{2.2}$$

where K is the coupling constant for the two wavefunctions having a weak overlap in the barrier region. The two macroscopic wavefunctions can be described using the following ansatz

$$\Psi_L = \sqrt{\rho_L}e^{i\phi_L}; \quad \Psi_R = \sqrt{\rho_R}e^{i\phi_R}, \tag{2.3}$$

where ρ_L, ρ_R denote the Cooper pair densities and ϕ_L, ϕ_R the phases of the Cooper pair wavefunctions that are assumed to be constant over the individual superconductors.

Substituting this Ansatz into the coupled wave equations 2.2, separating the results into real and imaginary part and subtracting the equivalent equations yields

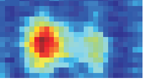

$$
\begin{aligned}
\frac{\partial}{\partial t}(\rho_L) &= \frac{2K}{\hbar}\sqrt{\rho_R\rho_L}\sin(\phi_R-\phi_L) \\
\frac{\partial}{\partial t}(\phi_R-\phi_L) &= \frac{1}{\hbar}(E_R-E_L)+K\cos(\phi_R-\phi_L)\left(\sqrt{\frac{\rho_L}{\rho_R}}-\sqrt{\frac{\rho_R}{\rho_L}}\right),
\end{aligned}
\tag{2.4}
$$

where we employed the continuity equation $\frac{\partial}{\partial t}\rho_L = -\frac{\partial}{\partial t}\rho_R$ for the exchange of Cooper pairs between left and right. If we define the relative phase between the two superconductors $\phi = \phi_R - \phi_L$ and, for the sake of convenience, assume identical superconductors (i.e. $\rho_L = \rho_R = \rho$), we get

$$
\begin{aligned}
\frac{\partial}{\partial t}(\rho_L) &= \frac{2K}{\hbar}\rho\sin(\phi) = -\frac{\partial}{\partial t}(\rho_R) \\
\frac{\partial}{\partial t}(\phi) &= \frac{1}{\hbar}(E_R-E_L).
\end{aligned}
\tag{2.5}
$$

Note that although ρ_L and ρ_R are assumed to be constant, they have a non-vanishing time derivative $\frac{\partial}{\partial t}(\rho)$. There is no contradiction if we take into account the continuous replacement of tunneling Cooper pairs by the external current source. Those feeding currents are not included in our derivation, but they would not change our expression for macroscopic tunneling[1]. We can derive the electrical current density by multiplying the Cooper pair current density with the Cooper pair charge $2e$. For the case of superconductors, the energy difference is given by a voltage $U = \frac{E_R-E_L}{2e}$ applied to the Josephson junction. This leads to the two Josephson equations for the current density and the evolution of the relative phase

$$
\begin{aligned}
J &= J_0\sin(\phi) \\
\frac{\partial}{\partial t}\phi &= \frac{2eU}{\hbar}
\end{aligned}
\tag{2.6}
$$

where $J_0 = \frac{4eK}{\hbar}\rho$ is the maximum allowed Cooper pair tunneling current density.

Note that the derivation of the two Josephson equations is only based on the existence of macroscopic wavefunctions and is therefore also valid for other physical systems like superfluid helium or Bose-Einstein condensates in the non-interacting limit (when replacing the applied voltage across the Josephson junction by a more general energy difference between left and right macroscopic wavefunction).

In the absence of an external voltage $U = 0$ the phase difference is constant, but not necessarily zero. In this case, equation 2.6 predicts, that a finite current with a maximum value $I_0 = J_0 A$ can flow through the barrier without any voltage drop across the junction, where A is the contact area of the Josephson junction. This phenomenon is called DC Josephson effect [1] and has already been demonstrated in 1963 by Anderson and Rowell [2] in their implementation of the first Josephson junction.

---

[1] For a complete self-consistent derivation see for example [50].

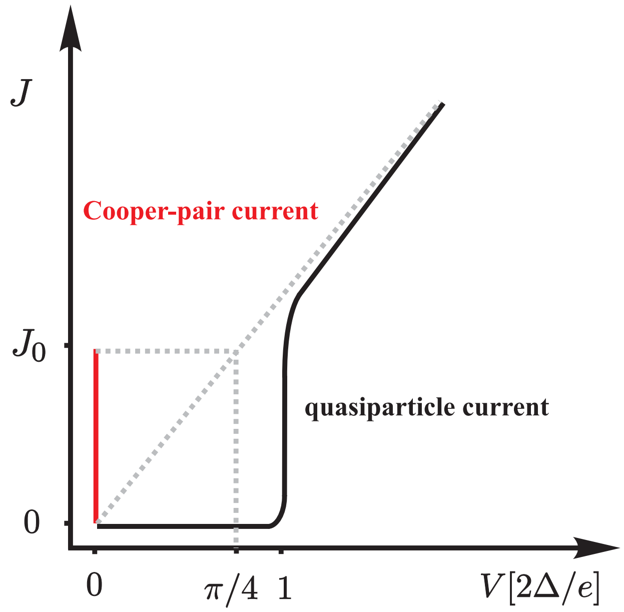

Figure 2.3: Typical DC current-voltage characteristics of a Josephson junction at zero temperature. Currents up to a current density J_0 can flow without applied external voltage (DC-Josephson effect). For junction voltages larger than the quasiparticle-gap $\frac{2\Delta}{e}$ the junction has a finite resistance (single electron tunneling) and the current contains an oscillating part with frequency $\omega = \frac{2eV}{\hbar}$(AC-Josephson effect)

If a constant Voltage $U \neq 0$ is applied to the junction, it follows from equation 2.6 that the phase $\phi = \phi_0 + \frac{2eU}{\hbar}t$ is linearly increasing in time which leads to an alternating current with a frequency $\omega = \frac{2eU}{\hbar} = 2\pi \cdot 483.6\,\frac{\mathrm{MHz}}{\mu\mathrm{V}}U$. This is the essence of the AC Josephson effect which was experimentally demonstrated by Shapiro in 1963 using the so-called Shapiro effect (see section 2.2.1).

How does the DC current-voltage characteristics of a Josephson tunnel junction look like, if we only take Cooper pair tunneling into account? This question is answered by figure 2.3. If the current flowing across the junction is smaller than the critical current J_0 given above, the system will be in a state with zero voltage drop. For $J > J_0$ the current has to originate from single electron (quasiparticle) tunneling with a finite resistance R. Therefore the voltage across the junction has to jump to $V = \frac{2\Delta}{e}$ at the critical current corresponding to a potential difference between the two superconductors sufficiently large to break up Cooper pairs (2Δ is the energy gap of the superconductor). For higher currents, the voltage current characteristics is linear according to Ohms law.

In order to compare the maximum Cooper pair current to the normal single electron current at the voltage-threshold $\frac{2\Delta}{e}$, Ambegaokar and Baraktoff [51] derived the following expression at $T = 0$:

$$I_0 R(T \to 0) = \frac{\pi}{2e}\Delta. \tag{2.7}$$

This result implies that the maximum Cooper pair current I_0 is approximately 80% of the single electron threshold current. The critical current density is typically on the order of $10^2 \frac{A}{\mathrm{cm}^2} - 10^3 \frac{A}{\mathrm{cm}^2}$. For a junction with a contact area of $10\,\mu\mathrm{m}^2$ this yields a typical critical current of $I_0 = 500\,\mu\mathrm{A}$. Using equation 2.7, this implies a resistance $R \approx 10\,\Omega$

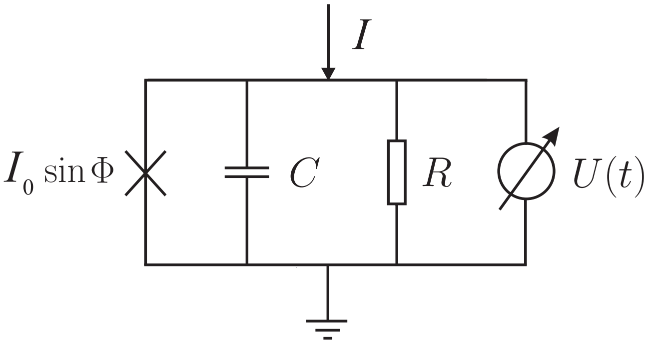

Figure 2.4: Equivalent circuit of a real current biased Josephson junction in the framework of the RCSJ-model. R represents the resistance for single-electron current and C is the finite capacitance of the junction.

for a typical value $\Delta = 3\,\text{meV}$.

2.2 RCSJ-model

Josephson tunneling involves quantum effects that are difficult to grasp intuitively. The current-voltage characteristics of a real Josephson junction including single electron tunneling is well explained by the resistively and capacitively shunted junction (RCSJ) model which was first used by Stewart [52] and McCumber [53] in 1968. Within this approach, the weak link is represented by the simple equivalent circuit in figure 2.4.

According to Kirchhoff‘s law the total current in this circuit is the sum of the superconducting Josephson current $I_s = I_0 \sin\phi$, a quasiparticle tunneling current $I_{qp} = \frac{U}{R}$ and a displacement current $I_C = C\frac{\partial}{\partial t}U$ which takes into account the finite capacitance of the Josephson junction. Therefore, the current balance equation reads

$$I = C\frac{\partial}{\partial t}U + \frac{U}{R} + I_0 \sin\phi. \tag{2.8}$$

Note that the RCSJ model neglects the effect of thermal noise and any spatial dependency of junction parameters within the junction cross section. The most important simplification is the assumption of a constant resistance R, both below and above the gap voltage.

Using the second Josephson relation in equation 2.6 we find the differential equation for the phase difference ϕ across the junction

$$I = \frac{\hbar C}{2e}\frac{\partial^2}{\partial t^2}\phi + \frac{\hbar}{2eR_n}\frac{\partial}{\partial t}\phi + I_0 \sin\phi. \tag{2.9}$$

Solving this differential equation using the relation $U_{dc} = \frac{\hbar}{2e}\langle\frac{\partial}{\partial t}\phi\rangle_t$ yields the dc current-voltage characteristics. For small relative phases $\phi \approx 0$ and for $I \longrightarrow 0$ this equation can be linearized leading to small sinusoidal phase-oscillations with the plasma frequency $\omega_p = \frac{2eI_0}{\hbar C}$.
Equation 2.9 can be solved analytically only in the case of vanishing capacitance C. However, one can gain insight into the possible solutions by bearing in mind a simple mechanical analog, which is described by a comparable differential equation.

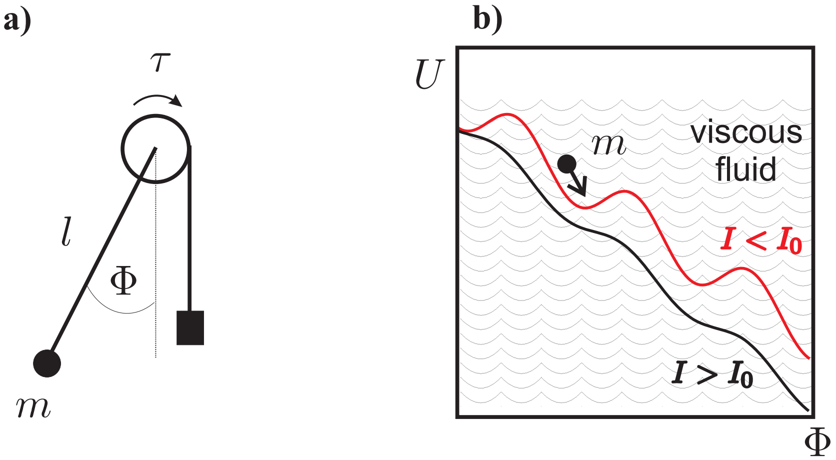

Figure 2.5: Mechanical analogons for a Josephson junction: rigid pendulum (a) and a particle moving on a tilted washboard potential in a viscous fluid (b). This analogons can provide intuitive insight into the tunneling dynamics in the framework of the RCSJ-model.

Let us consider a rigid pendulum of mass m and length l as shown in figure 2.5a. In the presence of a restoring torque due to gravity and a damping torque due to friction this pendulum can be described by the following differential equation for the pendulum angle ϕ:

$$\tau = M\frac{\partial^2}{\partial t^2}\phi + D\frac{\partial}{\partial t}\phi + mgl\sin\phi, \tag{2.10}$$

where τ is an external constant torque, $M = ml^2$ is the moment of inertia, D is the damping coefficient and g is the acceleration of gravity. This equation obviously has the same structure as equation 2.9 with corresponding quantities as given in table 2.1.

RCSJ-model				**rigid pendulum**
applied current	I	$\leftrightarrow$	τ	external torque
average (dc) voltage term	$\langle U\rangle_t\frac{2e}{\hbar}$	$\leftrightarrow$	$\omega = \frac{\partial}{\partial t}\phi$	average angular velocity
phase difference	ϕ	$\leftrightarrow$	ϕ	angular displacement
capacitance term	$\frac{\hbar}{2e}C$	$\leftrightarrow$	M	moment of inertia
critical current	I_0	$\leftrightarrow$	mgl	critical torque

Table 2.1: Equivalence between physical corresponding quantities describing a Josephson junction in the framework of the RCSJ-model and the classical rigid pendulum.

By means of this analogy, we can predict how the Josephson junction will reply with a dc-voltage when increasing the current I starting from zero. For $I < I_0$, corresponding to an applied torque being to small to bring the pendulum to the top position, the mean angular velocity and correspondingly the mean voltage drop across the junction will be zero. At $I = I_0$ the pendulum reaches the top position and every further increase will cause the pendulum to rotate, which implies a non-zero dc voltage drop across the junction. For very large currents, the mean value of the Josephson term $I_0 \sin\phi$ and

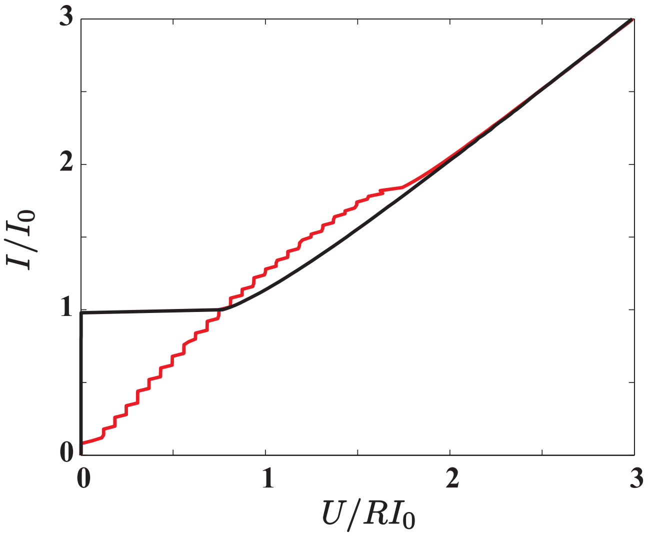

Figure 2.6: Current-voltage characteristics obtained by numerically solving the RCSJ-model (eq. 2.9) without (black line) and with (red line) an applied rf-current $I_{rf} = 490\,\mu$A. The parameters are $I_0 = 500\,\mu A$, $R = 10\,\Omega$, and $C = 10^{-13}\,F$.

the capacitance term in equation 2.9 can be neglected. This leads to a simple linear dependence $I = \frac{\langle U \rangle_t}{R}$ (Ohm‘s law). A typical current-voltage curve obtained in the RCSJ-model is shown in figure 2.6 (black line).

Some textbooks (for example Chesca *et al.* [47]) use another descriptive mechanical analogon in order to illustrate the RCSJ-model: a particle moving in a tilted washboard potential $U = \frac{\hbar}{2e}(I_0(1 - \cos\phi) - I\phi)$ inside a viscous medium (see figure 2.5b). This system is described by a differential equation similar to equation 2.10 and the same arguments as given for the pendulum analogy also hold in this case.

2.2.1 Shapiro effect

In section 2.1, we found that applying a dc voltage across a Josephson junction causes the flow of an ac current. In the inverse Josephson effect dc voltages are induced across an unbiased junction by applying an external microwave field which leads to the appearance of current steps at constant voltages. The easiest way to understand these steps is to represent the Josephson junction by the parallel equivalent RCSJ-circuit of figure 2.4, but now with a total current containing an additional rf-current

$$I_t = I + I_{rf}\cos(\omega_{rf}t). \tag{2.11}$$

A numerical solution of this equation provides a staircase current-voltage characteristics which is often referred to as Shapiro steps. This structure is indicated with the red line in figure 2.6. For a detailed discussion I refer to [54].

It is mathematically easier to analyze this problem in terms of a circuit, where we apply a voltage

$$U(t) = U_0 + U_{rf}\cos(\omega_{rf}t) \tag{2.12}$$

to the Josephson junction.

If we insert this voltage into the second Josephson equation 2.6 we get

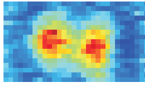

$$\phi(t) = \phi_0 + \frac{2e}{\hbar}U_0 t + \frac{2eU_{rf}}{\hbar\omega_{rf}}\sin(\omega_{rf}t), \tag{2.13}$$

where ϕ_0 is a constant of integration. This yields the following dc Josephson current

$$I(t) = I_0 \sin\left(\phi_0 + \frac{2e}{\hbar}U_0 t + \frac{2eU_{rf}}{\hbar\omega_{rf}}\sin(\omega_{rf}t)\right). \tag{2.14}$$

This equation can be expanded in terms of Bessel-functions J_n

$$I(t) = I_0 \sum_{n=1}^{\infty}(-1)^n J_n\left(\frac{2eU_{rf}}{\hbar\omega_{rf}}\right)\sin\left(\left(\frac{2eU_0}{\hbar} - n\omega_{rf}\right)t + \phi_0\right). \tag{2.15}$$

The time average over the oscillating term is only different from zero if $\frac{2eU_0}{\hbar} = n\omega_{rf}$. This means that if the frequency of the ac-Josephson current corresponds to an integer multiple of the radio frequency, we get steps of constant voltage in the voltage-current characteristics of the Josephson junction. These voltages are given by

$$U_n = \pm n\frac{\hbar}{2e}\omega_{rf}. \tag{2.16}$$

The height of the n-th Shapiro-step is given by[2]

$$I_n = I_0 J_n\left(\frac{2eU_{rf}}{\hbar\omega_{rf}}\right)\sin(\phi_0). \tag{2.17}$$

2.2.2 Ultrasmall Josephson junctions: Coulomb blockade

So far I have depicted a Josephson junction as an object whose characteristics were described by the two Josephson equations 2.6. The description in the framework of the RCSJ-model was exclusively classical and led us to the descriptive mechanical analog of a rigid pendulum.

Now I want to point out a quantum mechanical feature of Josephson junctions which is related to the finite capacitance of the junction and based on the quantization of the electric charge.

We assume a mesoscopic Josephson junction with a capacitance[3] $C \approx 10^{-15}\,F$. As a result of the tunneling of a single Cooper pair a voltage of $U = \frac{2e}{C} \approx 3\,\mathrm{mV}$ is built up across the junction. This voltage is accompanied by a charging energy $E_C = \frac{2e^2}{C}$ which can be larger than the Josephson coupling energy $E_J = \frac{\hbar}{2e}I_0$. This leads to an inhibition of tunneling of further Cooper pairs, provided that thermal fluctuations are small compared to the charging energy, which implies operation temperatures well below 1 K. The next Cooper pair cannot tunnel through the barrier until the voltage dissipates after a typical timescale $\delta_t = RC$. This inhibition of tunneling due to Coulomb interaction has been termed Coulomb blockade. It allows a control of the transfer of a single electron despite of the huge number of typically $> 10^9$ free electrons in the

---

[2] As shown in [54], the current steps are all positive because the voltage source has a fixed polarity, so the sign of ϕ_0 adjusts accordingly.

[3] This implies a junction contact area of $\approx 0.01\,\mu\mathrm{m}^2$, corresponding to an edge length of 100 nm.

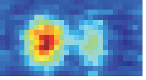

junction, which makes a realization of a single-electron transistors (SET) possible [55]. For a detailed review about this subject see for example [56].

One effect related to the Coulomb blockade occurs in ordered one or two-dimensional arrays of Josephson junctions, which can nowadays be manufactured by means of lithographic methods. Here the Mott insulator transition from a macroscopic superconductive state to an insulating state can be observed when the charging energy of the superconductors becomes larger than the Josephson-tunneling energy. In this case, the number of Cooper pairs per superconductor gets fixed leading to an undefined relative phase[4].

As we will see in chapter 3.3 the repulsive interparticle interaction of the Bose-Einstein condensates can lead to an inhibition of macroscopic tunneling. This corresponds to some extent to the continuous version of the Coulomb blockade described here.

2.3 Josephson effect in superfluid helium

We have seen in section 2.1 that Josephson tunneling of massive particles occurs in systems which can be described by a coherent macroscopic wavefunction. Another example of a macroscopic quantum system with a global phase coherence is superfluid ^{3}He and ^{4}He [57], where the Josephson effects described above have recently been found to have analogues. In this system, massive atoms can tunnel between weakly linked superfluids. Here, the viscosity corresponds to the electrical resistance and the Landau critical velocity to the critical current density in superconductors. For a detailed comparison of the different systems exhibiting Josephson effects see for example [58].

The tunneling experiments I will refer to in this section have been performed in the group of Packard with superfluid ^{3}He [59, 4] and in the group of Pearson with ^{4}He [60].

In the ^{3}He Josephson experiments, the overlap of two macroscopic wavefunctions is provided by an array consisting of 4225 small apertures, each of diameter 100 nm and length 50 nm. In order to realize a weak link between the superfluids, the aperture size has to be smaller than the superfluid coherence length ξ, which is often referred to as healing length at the operation temperature

$$\xi = \xi_0 [1 - T/T_C]^{-1/2}, \tag{2.18}$$

where $\xi_0 = 65\,\mathrm{nm}$ and T_C is the transition temperature. In the reported experiments, the individual apertures in the array act coherently. There is no interference between adjacent apertures so that the whole array behaves like a single weak link with 4225-fold increased current. The setup of the ^{3}He-experiment is shown in figure 2.7.

By applying a pressure gradient ΔP between the two reservoirs, the difference in the chemical potential becomes $\Delta\mu = 2m_3 \Delta P/\rho$ where $2m_3$ is the mass of a ^{3}He Cooper pair and ρ is the liquid density[5]. This results in a linear time evolution of the relative phase ϕ of the two superfluids according to the second Josephson equation

$$\phi(t) = \frac{\Delta\mu}{\hbar} t, \tag{2.19}$$

---

[4] The Mott insulator transition has also been observed for a BEC in a three dimensional optical lattice [25].

[5] This pressure gradient is experimentally implemented by changing the potential of the electrode in figure 2.7 with respect to the metallized soft membrane.

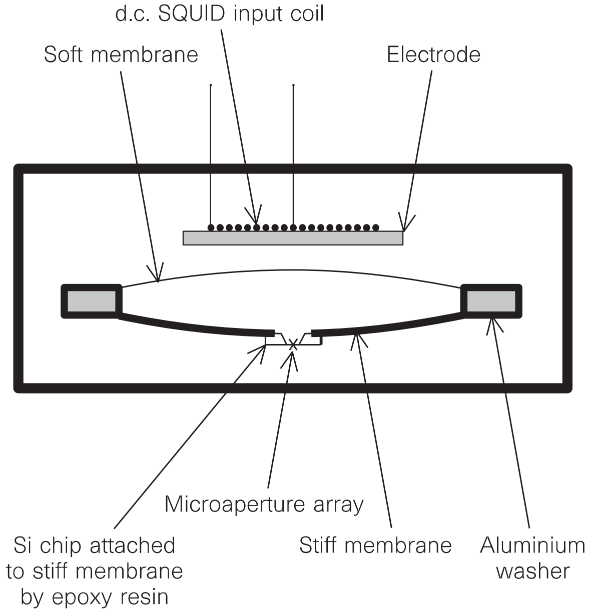

Figure 2.7: Experimental setup for the measurement of Josephson oscillations in superfluid ^{3}He. The relative phase can be changed by applying a pressure gradient between the two reservoirs on either side of the microaperture array. This leads to AC-Josephson currents through the weak link. The particle current can be observed by measuring the displacement of the soft membrane (from [59]).

which leads to ac tunneling-currents with a frequency of $183.7 \cdot 10^3\,\mathrm{Hz/Pa}$. This small frequency, which has to be compared to $4.82 \cdot 10^{14}\,\mathrm{Hz/V}$ in the superconducting analog, allows for an observation of the particle tunneling currents.

The instantaneous mass flow of ^{3}He Cooper pairs through the microaperture array can be obtained by measuring the displacement of the soft membrane in figure 2.7

$$I(t) = \rho A \frac{\partial}{\partial t} x, \tag{2.20}$$

where A is the membrane area. Additionally the membrane's displacement from the equilibrium position x_e is proportional to the pressure gradient: $\Delta P = \alpha(x - x_e)$. The knowledge of α allows for the determination of the instantaneous phase difference $\phi(t)$ by integrating equation 2.19:

$$\phi(t) = \frac{-2m_3}{\rho\hbar} \int_0^t \alpha(x(t) - x_e)dt. \tag{2.21}$$

Equations 2.20 and 2.21 show that it is possible to measure the current-phase relation of the superfluid weak link by measuring the position of the soft membrane as a function of time. For temperatures close to T_C corresponding to a healing length larger than the aperture size, the measured $I(\phi)$ dependency is nearly sinusoidal as predicted by the first Josephson equation. For lower temperatures (small healing length compared to the aperture diameter) the current-phase characteristics $I(\phi)$ evolves from sine-like to almost linear because the weak-link condition is no longer satisfied.

Additionally to the measurement of the current-phase relation, the same group has also shown the existence of a metastable superfluid state with a phase difference between

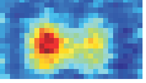

the two weakly coupled reservoirs which oscillates around a mean value of π [61]. This state is the analog to the so-called π-junction observable in superconductors in connection with extrinsic paramagnetic impurities [62] or in connection with the d-wave symmetry in high T_c superconductors [63]. As we will see in section 3.3 similar π-oscillations can also be realized in bosonic Josephson junctions.

It is important to note that weakly coupled systems are often discussed in terms of quantum mechanical tunneling. These tunneling barriers are not necessary for the occurrence of Josephson effects as shown by the described experiments with liquid helium. The physics governing the effect is only based on the existence of a weak link or in other words on a small overlap between two macroscopic wavefunctions. It is not relevant whether this overlap is provided by a tunneling barrier or by small apertures with dimensions smaller than the healing length of the system.

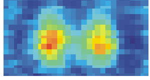

3 Theory of Josephson junctions for Bose-Einstein condensates

In our experiment, we use atomic Bose-Einstein condensates as a source of coherent macroscopic matter waves. The quantum statistics for indistinguishable bosons was introduced by Satyendra Bose [5] in 1924. The phenomenon of Bose-Einstein condensation of massive bosons has subsequently been predicted by Albert Einstein [6] in 1925. BEC is the basic process for the occurrence of superconductivity (BEC of cooper pairs) and superfluidity (BEC of ^{4}He and pairs of ^{3}He).

In the following, I want to give a short summary of the theory and characteristics of Bose-condensed atomic vapors to an extent which is needed for the description of the performed experiments. For a detailed description of the quantum statistics leading to BEC see for example [64] and [65]. For further insight into the special case of BECs of atomic vapors, I recommend the various books and review articles, for example [66, 67, 68].

In the following, a three dimensional trapped gas of bosonic atoms, which for the moment are assumed to be non-interacting, is described within the framework of the grand canonical ensemble. The atoms are trapped in an external potential $V_{\mathrm{ext}}(\mathbf{r})$ and occupy the single-particle states of the trap with eigenenergies ϵ_k. The occupation of these states is given by the Bose-distribution function

$$\langle n_k \rangle = \frac{1}{e^{(\epsilon_k - \mu)/k_B T} - 1} \tag{3.1}$$

where the atom number N is fixed by

$$N = \sum_k \langle n_k \rangle. \tag{3.2}$$

The total number of atoms in the excited states can be written as

$$N - N_0 = \int\limits_{\epsilon \neq \epsilon_0}^{\infty} \frac{\rho(\epsilon)}{e^{\left(\frac{\epsilon - \epsilon_0}{k_B T}\right)} - 1} d\epsilon, \tag{3.3}$$

where $\rho(\epsilon)$ is the density of states of the atomic gas trapped in the external potential $V_{\mathrm{ext}}(\mathbf{r})$. Here we have replaced the chemical potential by the ground state energy. At large temperatures the chemical potential is large and negative. As the atomic gas is cooled down, μ approaches the ground state energy ϵ_0 until at a critical temperature T_C it becomes equal to ϵ_0. In this case, the maximum number of atoms in the excited states becomes limited and the occupation of the ground state N_0 becomes a macroscopic fraction of the total atom number N. In the limit $T \rightarrow 0$ all atoms are in the ground state of the external confinement. This phenomenon is called Bose-Einstein condensation. Note, that in all BEC experiments the energy associated with the temperature is much bigger than the ground state energy[1] $k_B T \gg \epsilon_0$. One finds that, independent of the trap geometry, Bose-Einstein condensation occurs if the so-called phase-space density at the center of the trap reaches the critical value

$$n_0 \lambda_{dB}^3 = \zeta(3/2) \approx 2.61. \tag{3.4}$$

Here n_0 denotes the maximum atomic density,

$$\lambda_{dB} = \frac{h}{\sqrt{2\pi m k_B T}} \tag{3.5}$$

the thermal de Broglie wavelength, m the atomic mass and ζ Rieman's zeta-function.

Equation 3.4 reflects the fact that BEC occurs if the de Broglie wavelength is on the order of the interparticle separation which means that the quantum mechanical wavefunctions of the atoms start to overlap.

In the case of a harmonic trap, which is encountered in most experimental realizations, the density of states is given by

$$\rho_{ho}(\epsilon) = \frac{1}{2}(\hbar\bar{\omega})^{-3}\epsilon^2, \tag{3.6}$$

where we have defined the mean trapping frequency

$$\bar{\omega} = (\omega_x \omega_y \omega_z)^{\frac{1}{3}}. \tag{3.7}$$

The critical temperature for this case can be obtained by substituting 3.7 into equation 3.3 and integrating over ϵ. The phase transition occurs when N_0 becomes larger than zero which leads to

$$k_B T_C = \hbar\bar{\omega}\left(\frac{N}{\zeta(3)}\right)^{\frac{1}{3}} \approx 0.94\,\hbar\bar{\omega}N^{\frac{1}{3}}. \tag{3.8}$$

In our experiments with typical trap frequencies $\bar{\omega} = 2\pi \cdot 80\,\mathrm{Hz}$ and atom numbers $N = 1000$ this equation leads to a critical temperature of $T_C \approx 40\,\mathrm{nK}$. The fraction of atoms in the BEC below the critical temperature is given by

$$\frac{N_0}{N} = 1 - \left(\frac{T}{T_c}\right)^3. \tag{3.9}$$

The presented derivation of the BEC phase-transition has assumed non-interacting bosons in the thermodynamic limes ($N \rightarrow \infty$). This derivation is valid as long as the atomic gas satisfies the condition for a weakly interacting gas $\rho_0 a^3 \ll 1$, where $a = 5.32\,\mathrm{nm}$ is the s-wave scattering length for ^{87}Rb. The influence of finite atom numbers and interatomic interactions slightly decreases the fraction of condensed atoms for a given temperature [67]. However, for typical experimental parameters this effect is on the scale of less than one percent.

---

[1] From a classical point of view this is very counterintuitive since according to Boltzmann statistics, a macroscopic occupation of the ground state is only possible at $k_B T < \epsilon_0$.

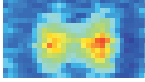

3.1 Meanfield description for BECs: the Gross-Pitaevskii equation

It is a very difficult task to solve the equations that describe N interacting bosons. However, Bose-Einstein condensates of atomic vapors are dilute gases of a typical density $\rho_0 = 10^{14}/\mathrm{cm}^3$. In this regime, the interatomic distance is much larger than the s-wave scattering length a, which describes an effective range of the atom-atom interaction. Therefore elastic two-body low energy collisions are dominant and the scattering potential can be approximated by a delta-shaped potential

$$U(\mathbf{r}-\mathbf{r}') = g_{3d}\,\delta(\mathbf{r}-\mathbf{r}'), \tag{3.10}$$

where $g_{3d} = \frac{4\pi\hbar^2 a}{m}$ denotes the three-dimensional coupling constant. The scattering length a is positive for repulsive interaction and negative for attractive interaction. By assuming this interaction potential and applying the Bogoliubov approximation[2], E.P. Gross [69, 70] and L.L. Pitaevskii [71] have developed a mean field theory for the approximate description of BECs at zero temperature. In this framework the condensate is described by a macroscopic one-body wavefunction $\Psi(\mathbf{r},t)$ and obeys the Gross-Pitaevskii-equation (GPE)

$$i\hbar\frac{\partial}{\partial t}\Psi(\mathbf{r},t) = \left[-\frac{\hbar^2}{2m}\Delta + V_{\mathrm{ext}}(\mathbf{r}) + g_{3d}N\left|\Psi(\mathbf{r},t)\right|^2\right]\Psi(\mathbf{r},t). \tag{3.11}$$

This description provides a simple language to explain most of the so-far performed experiments with BECs in terms of a few physical quantities. In this representation, the condensate wavefunction is normalized to unity and the square of its absolute value determines the atomic density $\rho(\mathbf{r},t) = N\cdot|\Psi(\mathbf{r},t)|^2$. The total energy consists of a kinetic energy, a potential energy inside the external trap and a meanfield-interaction energy which is proportional to the square of the wavefunction and therefore often referred to as nonlinearity. The Gross-Pitaevskii equation can in general not be solved analytically. In the limiting case of dominant kinetic energy, the GPE reduces to the linear Schrödinger equation and one recovers the ground state wavefunction in the external potential. In the opposite case, we can neglect the kinetic energy term, which corresponds to the so-called Thomas Fermi approximation. The density distribution is then given by

$$\rho(\mathbf{r}) = g^{-1}(\mu - V_{\mathrm{ext}}(\mathbf{r}))\,\Theta(\mu - V_{ext}(\mathbf{r})) \tag{3.12}$$

where Θ is the unit step function. In the case of a harmonic external confinement the shape of the cloud is described by an inverted parabola.

3.2 Non-polynomial nonlinear Schrödinger equation

The numerical integration of the three-dimensional Gross-Pitaevskii equation 3.11 with an acceptable spatial resolution is a task that requires a sophisticated implementation

---

[2] In the framework of the Bogoliubov theory, the bosonic fieldoperator which annihilates a particle at position $\mathbf{r}$ is replaced by its mean value $\Psi(\mathbf{r}) = \langle\hat{\Psi}(\mathbf{r})\rangle$. This condensate wavefunction is a classical field which plays the role of the order parameter in the Bose-Einstein phase transition.

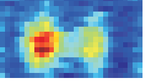

and a huge calculation effort. There have been several attempts to solve the physical problem by using a one-dimensional equation which to some extent includes the transverse motion of a Bose-Einstein condensate in the corresponding potential [72, 73]. The necessary approximations are especially justified for cigar shaped BECs where the dynamical evolution is mainly restricted to the longitudinal axis and the transverse states are close to the harmonic transverse groundstate. We will see in section 3.6 that this condition is fulfilled for our experimentally realized atom numbers and potentials. As already mentioned in the PhD thesis of Bernd Eiermann [74], a comparison of the approach of Salasnich *et al.* [73] and the full numerical solution of the 3d-Gross-Pitaevskii equation has provided the best agreement. This approach assumes that the transverse spatial wavefunction of the Bose-Einstein condensate can be described by a Gaussian distribution

$$\Psi(y,z,t,\sigma_\perp(x,t)) \propto \exp\left(-\frac{y^2+z^2}{2\sigma_\perp(x,t)^2}\right), \tag{3.13}$$

where the transverse Gaussian width $\sigma_\perp(x,t)$ depends on the longitudinal coordinate x and on time. The expression for $\sigma_\perp(x,t)$ is obtained by minimizing the action integral

$$S = \int dt\, d\mathbf{r}\, \Psi^*(\mathbf{r}) \left[i\hbar\frac{\partial}{\partial t} + \frac{\hbar^2}{2m}\nabla^2 - V_{\mathrm{ext}}(\mathbf{r}) - \frac{1}{2} g_{3d} N |\Psi(\mathbf{r})|^2 \right] \Psi(\mathbf{r}) \tag{3.14}$$

with respect to $\sigma_\perp(x,t)$ and yields

$$\sigma_\perp(x,t)^2 = a_\perp^2 \sqrt{1+2aN|\Psi(x,t)|^2}, \tag{3.15}$$

where $a_\perp = \sqrt{\frac{\hbar}{m\omega_\perp}}$ is the $1/\sqrt{e}$ width of the transverse groundstate wavefunction in a harmonic confinement with a trapping frequency $\omega_\perp$. The effective one-dimensional Schrödinger equation is then given by [73]

$$\begin{aligned} i\hbar\frac{\partial}{\partial t}\Psi(x,t) = & \left[-\frac{\hbar^2}{2m}\frac{\partial^2}{\partial x^2} + V_{\mathrm{ext}}(x) + g_{1d}N\frac{|\Psi(x,t)|^2}{\sqrt{1+2aN|\Psi(x,t)|^2}} \right] \Psi(x,t) \\ & + \left[\frac{\hbar\omega_\perp}{2} \left(\frac{1}{\sqrt{1+2aN|\Psi(x,t)|^2}} + \sqrt{1+2aN|\Psi(x,t)|^2} \right) \right] \Psi(x,t), \end{aligned} \tag{3.16}$$

where we have introduced the one-dimensional coupling constant $g_{1d} = 2\hbar a\omega_\perp$. Equation 3.16 is often referred to as non-polynomial nonlinear Schrödinger equation (NPSE) and can be numerically implemented with comparatively small effort. This effective one-dimensional description of the system provides an excellent agreement with our experimental results on Josephson effects between two coupled BECs (see section 3.6.)

3.3 Two-mode approximation

In order to realize a weak link between two ^{87}Rb Bose-Einstein condensates we load a BEC into an external effective double well potential, which can be approximated by

$$V(x,y,z) = \frac{1}{2}m(\omega_x^2x^2 + \omega_y^2y^2 + \omega_z^2z^2) + V_0 \cdot \left(\cos(\pi x/q_0)\right)^2, \tag{3.17}$$

where $m = 1.44 \cdot 10^{-25}$ kg is the mass of a Rubidium atom, $\omega_x = 2\pi \cdot 78$ Hz, $\omega_y = 2\pi \cdot 66$ Hz and $\omega_z = 2\pi \cdot 90$ Hz are the harmonic trapping frequencies, $q_0 = 5.2\,\mu$m is the spacing and $V_0 = h \cdot 413$ Hz the potential depth of the optical lattice. The central part of the density profile in x-direction is sketched in figure 3.1.

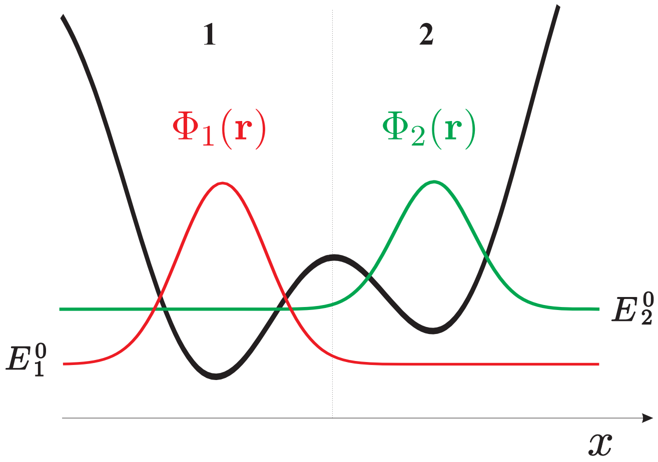

Figure 3.1: Double well potential for Bose-Einstein condensates (black line). The localized modes Φ_1 and Φ_2 in well 1 and well 2 are represented with red and green lines. E_1^0 and E_2^0 denote the respective zero point energies. These energies are equal for a symmetric double well potential.

In principal, one has to integrate the GPE or the NPSE given in the last section by substituting V_{ext} with the effective double well potential in order to describe the dynamics of the system. Such a numerical solution will be presented in section 3.6.

The condensate tunneling between two adjacent traps which results in an oscillatory exchange of the atoms between the traps has already been investigated in 1986 [28]. However, the author did not include the many-body interaction between atoms inside a single well (on-site interaction) which, as we will see in the following chapter is responsible for a rich variety of different dynamical regimes of the system.

In this chapter an approximation is discussed, which can at least qualitatively describe the different regimes of nonlinear dynamics of the system of two weakly linked Bose-Einstein condensates. The total wavefunction is written as a superposition of two time-independent spatial wavefunctions localized in the respective well. In such a way, a formal description of the system in terms of only two dynamical parameters, the fractional population imbalance and the relative phase can be obtained. These two variables are canonically conjugate and satisfy two coupled differential equations, which only contain a few static properties. The mechanical analogon of a nonrigid pendulum will give intuitive insight into the complicated dynamics of this nonlinear generalization of superconducting Josephson junctions.

In the following the dynamics of the two coupled systems is constrained to a subspace spanned by the two-mode wavefunction

$$\Psi(\mathbf{r}, t) = \Psi_1(t)\Phi_1(\mathbf{r}) + \Psi_2(t)\Phi_2(\mathbf{r}) \tag{3.18}$$

with

$$\Psi_{1,2}(t) = \sqrt{N_{1,2}(t)}e^{i\phi_{1,2}(t)} \tag{3.19}$$

where $N_{1,2}$ is the number of atoms and $\phi_{1,2}$ the phase in the corresponding well. The normalization of the total wavefunction $\Psi(\mathbf{r},t)$ is fixed by the total atom number $N_T = N_1 + N_2$ and by $\int |\Phi_{1,2}|^2 \, d\mathbf{r} = 1$. In order to fulfill the condition for a weak link, we claim $\int \Phi_1 \Phi_2 \, d\mathbf{r} \ll 1$, which is often referred to as "tight binding approximation". The spatial wavefunctions $\Phi_1(\mathbf{r}), \Phi_2(\mathbf{r})$ can be obtained by a linear combination of the normalized lowest symmetric $\Phi_s(\mathbf{r})$ and antisymmetric $\Phi_{as}(\mathbf{r})$ stationary eigenstates of the Gross-Pitaevskii equation:

$$\begin{aligned} \Phi_1(\mathbf{r}) &= \frac{\Phi_s(\mathbf{r}) + \Phi_{as}(\mathbf{r})}{\sqrt{2}} \\ \Phi_2(\mathbf{r}) &= \frac{\Phi_s(\mathbf{r}) - \Phi_{as}(\mathbf{r})}{\sqrt{2}}. \end{aligned} \tag{3.20}$$

Due to the existence of the nonlinear interaction term the Gross-Pitaevskii equation does in general not support the superposition principle. Nevertheless, ansatz 3.18 is justified for two very weakly overlapping clouds, for which the interaction in the overlap region can be neglected. Additionally, the use of time-independent spatial wavefunctions $\Phi_1(\mathbf{r}), \Phi_2(\mathbf{r})$ restricts the description to the regime, where atomic interaction produces only small modifications of the ground state properties in the individual wells.

If we substitute ansatz 3.18 into the Gross-Pitaevskii equation 3.11, multiply by $\Phi_1^*(\mathbf{r})$ and integrate over the spatial dimensions, we find the following equation[3]

$$\begin{aligned} & i\hbar\tfrac{\partial}{\partial_t}\Psi_1(t) = \\ & \left(\int \left[-\tfrac{\hbar^2}{2m}\Phi_1\nabla^2\Phi_1 + \Phi_1^2 V_{\text{ext}} + N_1\Phi_1^4 g + \Phi_1^3\Phi_2\Psi_2^*\Psi_1 g + 2N_2\Phi_1^2\Phi_2^2 g\right] d\mathbf{r}\right)\Psi_1 \\ & + \left(\int \left[-\tfrac{\hbar^2}{2m}\Phi_1\nabla^2\Phi_2 + \Phi_1 V_{\text{ext}}\Phi_2 + N_2\Phi_1\Phi_2^3 g + \Phi_1^2\Phi_2^2\Psi_1^*\Psi_2 g + 2N_1\Phi_1^3\Phi_2 \; g\right] d\mathbf{r}\right)\Psi_2 \end{aligned} \tag{3.21}$$

and a corresponding equation for $\Psi_2(t)$ by replacing all "1"s by "2"s and vice versa. In the following we only retain on-site interaction, since the spatial overlap of the two modes is assumed to vanish. Therefore we neglect all mixed terms in Φ_1 and Φ_2 of order larger than two[4]. If we define the constant parameters

$$\begin{aligned} E^0_{1,2} &= \int \left[\frac{\hbar^2}{2m}|\nabla\Phi_{1,2}|^2 + |\Phi_{1,2}|^2 V_{\text{ext}}\right] d\mathbf{r} \\ K &= -\int \left[\frac{\hbar^2}{2m}\nabla\Phi_1\nabla\Phi_2 + \Phi_1 V_{\text{ext}}\Phi_2\right] d\mathbf{r} \\ U_{1,2} &= g\int |\Phi_{1,2}|^4 d\mathbf{r}, \end{aligned} \tag{3.22}$$

---

[3] In the following, the localized modes Φ_1 and Φ_2 are assumed to be real, since they are linear combinations of the stationary states Φ_s and Φ_{as}.

[4] All terms in equation 3.21 can be included in the framework of the extended two mode model, which will be described in section 3.4

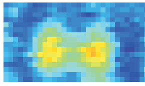

we get the following two coupled Schrödinger equations for the BEC amplitudes in the two wells

$$\begin{aligned} i\hbar\frac{\partial}{\partial t}\Psi_1 &= (E_1^0 + U_1 N_1)\Psi_1 - K\Psi_2 \\ i\hbar\frac{\partial}{\partial t}\Psi_2 &= (E_2^0 + U_2 N_2)\Psi_2 - K\Psi_1. \end{aligned} \tag{3.23}$$

These equations are very similar to equations 2.2 which describe the weak coupling of two superconductors. However, the nonlinearity arising from interatomic interaction gives rise to an additional term which leads to new effects unobservable in superconducting Josephson junctions (SJJ).

In analogy to the description of SJJs in section 2.1, we define the relative phase of the wavefunctions in the two wells

$$\phi(t) = \phi_2(t) - \phi_1(t) \tag{3.24}$$

and the fractional population imbalance

$$z(t) = \frac{N_1(t) - N_2(t)}{N_T}. \tag{3.25}$$

For the definition of the relative phase, we have assumed a constant quantum phase of a localized mode. The numerical calculations in chapter 3.6 will show, that this assumption is justified for our experimental parameters. The fractional population imbalance has no analog in the case of superconducting Josephson junctions, since the external circuits suppresses charge imbalances[5] ($z_{SJJ} = 0$).

In close analogy to the derivation of the Josephson equations in section 2.1, equation 3.23 leads to a system of two coupled differential equations for the two dynamic variables z and ϕ:

$$\begin{aligned} \dot{z}(t) &= -\sqrt{1 - z^2(t)}\sin\phi(t) \\ \dot{\phi}(t) &= \Delta E + \Lambda z(t) + \frac{z(t)}{\sqrt{1 - z^2(t)}}\cos\phi(t), \end{aligned} \tag{3.26}$$

where the time is expressed in units of $\frac{\hbar}{2K}$ and we have defined the dimensionless parameters

$$\begin{aligned} \Delta E &= \frac{E_1^0 - E_2^0}{2K} + \frac{U_1 - U_2}{4K} N_T \\ \Lambda &= \frac{U_1 + U_2}{4K} N_T. \end{aligned} \tag{3.27}$$

Equations 3.26 describe a nonrigid pendulum with a length $l = \sqrt{1 - z^2}$ if we identify the relative phase ϕ with the displacement angle and the fractional population imbalance

---

[5] As discussed in section 2.2.2, small fractional charge imbalances on the order of $z \approx 10^{-9}$ can occur in mesoscopic superconducting Josephson junctions.

z with the angular momentum of the pendulum. The interwell trap tunneling current is given by

$$I = \frac{\dot{z}(t)N_T}{2} = I_0\sqrt{1-z^2}\sin\phi, \tag{3.28}$$

where $I_0 = -\frac{KN_T}{\hbar}$ corresponds to the maximum allowed Cooper pair current in the superconducting analog. This equation is very similar to the first Josephson equation describing the dc Josephson effect in superconductor tunneling junctions. However, it differs from the SJJ-equation in the nonlinearity in z. Equations 3.26 can also be derived employing the concepts of nonlinear guided wave optics [75]. They resemble the dynamic equations for the guided power and phase difference of two interacting orthogonally polarized optical modes in a birefringent fiber.

In contrast to the pendulum analogy in the framework of the RCSJ-model in superconductor Josephson junctions, the atomic counterpart in a symmetric double well potential has no external torque[6]. Nevertheless, we can reach a regime, in which the nonrigid pendulum rotates with non-vanishing mean angular momentum ($z(t) \neq 0$ for all t) by choosing a large initial angular momentum $z(0)$ (see section 3.3.2). This means, that the population gets locked inside one well which, in the RCSJ pendulum analogy corresponds to a dc-voltage drop across the Josephson junction.

Another way to deduce the two-mode equations 3.26 is to express the total conserved energy of the system in terms of the canonically conjugate two-mode dynamical variables z and ϕ:

$$H = \frac{\Lambda z^2}{2} + \Delta E z - \sqrt{1-z^2}\cos\phi. \tag{3.29}$$

and use the Hamilton equations of motion

$$\dot{z} = -\frac{\partial H}{\partial \phi} \qquad \text{and} \qquad \dot{\phi} = \frac{\partial H}{\partial z}. \tag{3.30}$$

In the following, I will restrict the discussion of the Josephson junction dynamics to the case of a symmetric double well potential with $E_1^0 = E_2^0, U_1 = U_2$ and therefore $\Delta E = 0$.

3.3.1 Zero phase modes

In this section, I investigate the first class of Josephson tunneling dynamics, in which the time-average of both dynamical variables z and ϕ is zero.

Non-interacting limit: Rabi-oscillations

For symmetric double well potentials and negligible interatomic interaction ($U = \Lambda = 0$) the differential equations 3.26 reduce to

$$\ddot{z} = -z. \tag{3.31}$$

---

[6] A time-dependent barrier moving adiabatically across the trapping potential has been investigated in [76]. In this case, the phase dynamics are governed by a driven pendulum dynamics, analog to current-driven SJJ.

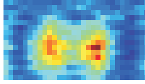

The corresponding solution is a sinusoidal Rabi-like oscillation of the population imbalance z with a frequency (in unscaled units)

$$\omega_R = \frac{2}{\hbar} K. \tag{3.32}$$

The Rabi-oscillations are shown with dashed red lines in figure 3.2a. This limit of vanishing interaction between the Bose-Einstein condensed atoms can in principle nowadays be realized using Feshbach resonances [41] in which a homogenous magnetic field is used to adjust the s-wave scattering length[7].

Small amplitude oscillations: Josephson plasma frequency

For a symmetric double well potential, the equilibrium value of the fractional population imbalance and the relative phase is $z = 0$ and $\phi = 0$. Linearization of the equation of motion 3.26 around these values yields

$$\ddot{z} = -(\Lambda + 1) z. \tag{3.33}$$

This equation describes sinusoidal small amplitude oscillations with an unscaled frequency

$$\omega_{\mathrm{pl}} = \sqrt{\Lambda + 1}\, \frac{2K}{\hbar}. \tag{3.34}$$

In this regime, the oscillation frequency is independent of the initial conditions for z and ϕ as long as the small amplitude approximation holds. These oscillations are often referred to as plasma oscillations in analogy to superconducting Josephson junctions. Figure 3.2a shows the sinusoidal small amplitude oscillations for $\Lambda = 15$ and $z(0) = 0.1$ (black line). For our experimentally realized potential and atom numbers, the plasma frequency is typically on the order of $2\pi \cdot 30\,\mathrm{Hz}$, which has to be compared to typical SJJ plasma frequencies on the order of several gigahertz.

Large amplitude oscillations

In the general case of interacting atoms with large tunneling amplitudes, equations 3.26 can be solved in terms of Jacobian elliptic functions as shown in [30]. The large amplitude oscillations are the anharmonic nonlinear generalization of the sinusoidal tunneling dynamics in superconductor Josephson junctions. In this regime, the oscillation frequency depends on the initial population imbalance $z(0)$ and the relative phase $\phi(0)$. A numerical solution of equations 3.26 in the regime of large amplitude oscillations is shown in figure 3.2 b and 3.2c. An increase of the initial population imbalance $z(0)$ adds higher harmonics to the sinusoidal oscillations, which leads to more and more anharmonic tunneling dynamics. The oscillation period now increases with $z(0)$ until, at a certain population imbalance z_c, the dynamics undergoes a critical slowdown (dashed red line in figure 3.2c). This happens, when the initial angular momentum in the nonrigid pendulum analogon is just enough to reach a maximum phase of π during the dynamical evolution. The pendulum stops at the top position which corresponds to a zero angular momentum, i.e. a population imbalance $z = 0$.

---

[7] For the case of ^{87}Rb, the width of the Feshbach resonances are on the order of 1 mG [42]. Therefore, they are very hard to implement experimentally.

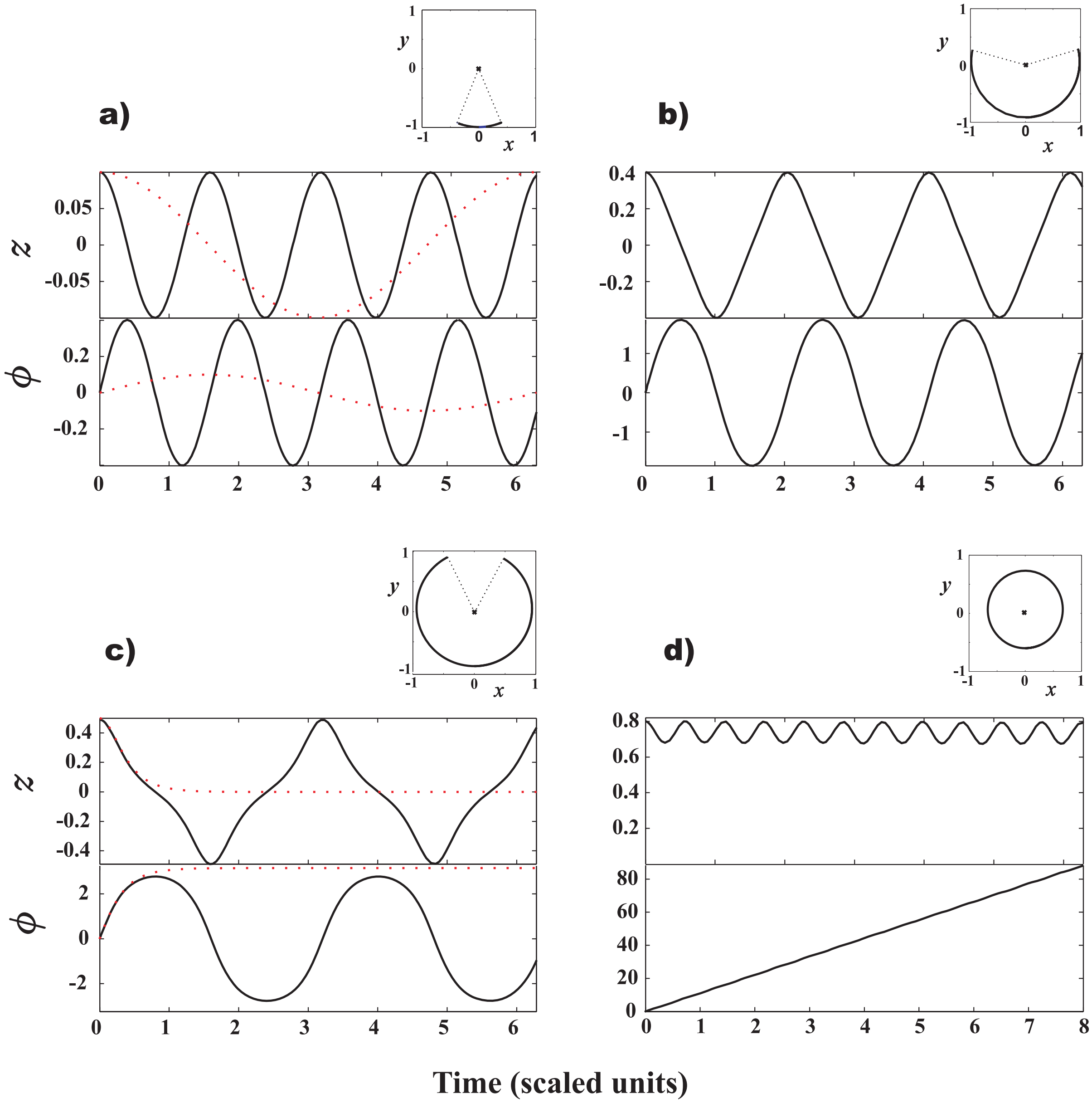

Figure 3.2: Dynamical evolution of the population imbalance z and relative phase ϕ for $\Lambda = 15$. The initial phase $\phi(0)$ is chosen to be zero for all trajectories. The small figures on top show the trajectory of the nonrigid pendulum analog in the corresponding regimes. a) An initial population imbalance $z(0) = 0.1$ results in sinusoidal small amplitude oscillations (black line). The dotted red line shows the evolution expected for non-interacting atoms ($\Lambda = 0$, Rabi oscillations). b) Non-sinusoidal large amplitude oscillations for $z = 0.4$. c) Tunneling dynamics slightly below (black line , $z = 0.49$) and at (dotted red line) the selftrapping threshold $z_c = 0.499$. d) Macroscopic quantum self-trapping for $z = 0.8 > z_c$. The population oscillates around a non-zero mean value and the relative phase increases monotonically (running phase modes).

3.3.2 Macroscopic quantum self-trapping

As shown in the last section, the dynamics of the system changes drastically, when the initial population imbalance approaches a critical value z_c. For larger population imbalances $z(0) > z_c$ the tunneling is strongly suppressed, which leads to self-trapped, nearly stationary modes localized inside a single well ($\langle z \rangle_t \neq 0$).

The critical value is reached, when the atomic tunneling between the two wells is no longer fast enough to counteract the evolution of the relative phase due to the difference of the chemical potentials in the left and the right well. According to equation 3.28, the tunneling current reverses, when the relative phase exceeds the value π. If this happens before the population imbalance has been inverted due to tunneling, the population is locked inside one well and the relative phase will evolve monotonically and unbound (running phase mode).

This leads to a condition for z_c: the initial energy for $z(0) = z_c$ and $\phi(0)$, given by equation 3.29 has to be large enough to reach $\phi_{\text{final}} = \pi$ at $z_{\text{final}} = 0$ which corresponds to an energy $H_{\text{final}} = 1$:

$$H_0 \equiv H(z(0) = z_c, \phi(0)) = \frac{\Lambda}{2} z_c^2 - \sqrt{1 - z_c^2} \cos\phi(0) \equiv 1. \tag{3.35}$$

For a zero initial phase, this equality is only solvable for $\Lambda > 2$ and a positive K. For smaller Λ, there is no transition to self-trapping, even at arbitrary large initial population-imbalances $z(0)$. Using equation 3.35 we find, that the critical population imbalance for macroscopic quantum self-trapping (MQST) for $\phi(0) = 0$ is given by

$$z_c = \frac{2\sqrt{\Lambda - 1}}{\Lambda} \quad \text{for } \Lambda > 2. \tag{3.36}$$

From our experiments, we deduce a critical population imbalance $z_c \approx 0.5$, which means that the left localized mode Ψ_1 contains 75% of the total number of atoms (see chapter 5). If we assume the validity of the two-mode approximation, this value corresponds to $\Lambda \approx 15$, for which the different dynamical regimes are shown in figure 3.2. However, a numerical calculation of the symmetric and antisymmetric states yields $\Lambda \approx 76$. The reason why the two-mode approximation fails to quantitatively explain our experimental results is discussed in section 3.3.5.

In order to reach the self-trapping threshold, we can increase $z(0)$ above the critical value z_c for a fixed value of Λ, or alternatively increase Λ by increasing the total atom number N_T and keeping z_0 fixed. From equation 3.35 we get an expression for the scaled critical on-site interaction energy

$$\Lambda_c = 2\,\frac{1 + \sqrt{1 - z(0)^2}\cos(\phi(0))}{z(0)^2}. \tag{3.37}$$

The dynamical evolution in the regime of MQST is shown in figure 3.2d for z(0)=0.8. The oscillation period of the population imbalance z increases and the amplitude decreases with increasing $z(0)$. The phase difference between the two Bose-Einstein condensates in the left and right well evolves unbound. The effect of MQST can be visualized in the nonrigid pendulum analogy. There the self-locked population imbalance corresponds to a steady self-sustained rotation of the pendulum with non-vanishing mean angular momentum z and phase ϕ. The effect of macroscopic self-trapping is a nonlinear effect arising from the scaled on-site interaction energy of the Bose-Einstein condensates in the individual wells. It is self-maintained in a closed conservative system without an external drive. There is no analogon for MQST in superconductor Josephson junctions since the running phase mode in the RCSJ-model is a driven steady state which is independent of the initial relative phase of the two superconductors. It is also different from the

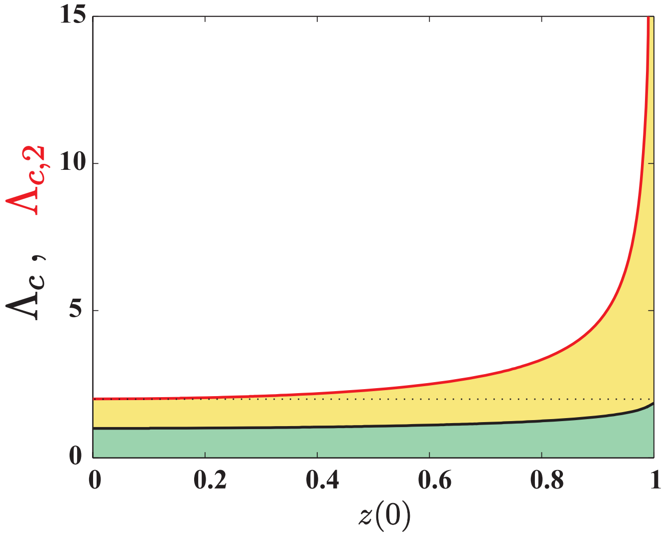

Figure 3.3: Scaled critical on-site interaction energies Λ_c (black line) and $\Lambda_{c,2}$ (red line) as a function of the initial population imbalance $z(0)$ for an initial phase $\phi(0) = \pi$. The green shaded region corresponds to the regime of π-oscillations. The yellow shaded region indicates the regime of π-phase MQST. The running-phase MQST-regime (unshaded region) which is the same as the MQST for $\phi(0) = 0$ can be reached for $\Lambda > \Lambda_{c,2}$.

discrete Coulomb blockade effect discussed in section 2.2.2 which occurs as a result of the tunneling of a single Cooper pair leading to a charging energy E_C larger than the Josephson coupling energy E_J.

The first experimental observation of Josephson tunneling oscillations and macroscopic quantum self-trapping for Bose-Einstein condensates will be presented in chapter 5.

3.3.3 π-phase modes

Additionally to the discussed zero-phase modes and MQST, Bose-Einstein Josephson junctions have another rich class of tunneling dynamics in which the system evolves with a time-averaged value of the relative phase of $\langle\phi\rangle_t = \pi$. Those π-phase modes have not been observed so far in Josephson junctions for Bose-Einstein condensates and I will therefore restrict the discussion to the basic features of this dynamical regime. For a detailed description see for example [30].

The momentum dependent length of the pendulum allows the pendulum to perform small and large amplitude π-oscillations with $\langle z\rangle_t = 0$ around the unstable equilibrium top position. Similar to the zero phase modes discussed above the dynamics changes to macroscopically self-trapped modes with non-zero average of the population imbalance if the scaled on-site interaction energy Λ exceeds the critical value given by equation 3.37.

In contrast to the zero initial phase self-trapping discussed above, there are two distinct self-trapping regimes for $\phi(0) = \pi$ which are separated by another critical on-site interaction energy [30]: $\Lambda_{c,2} = \frac{2}{\sqrt{1-z(0)^2}}$. The two critical parameters as a function of the initial population imbalance are shown in figure 3.3 for $\phi(0) = \pi$.

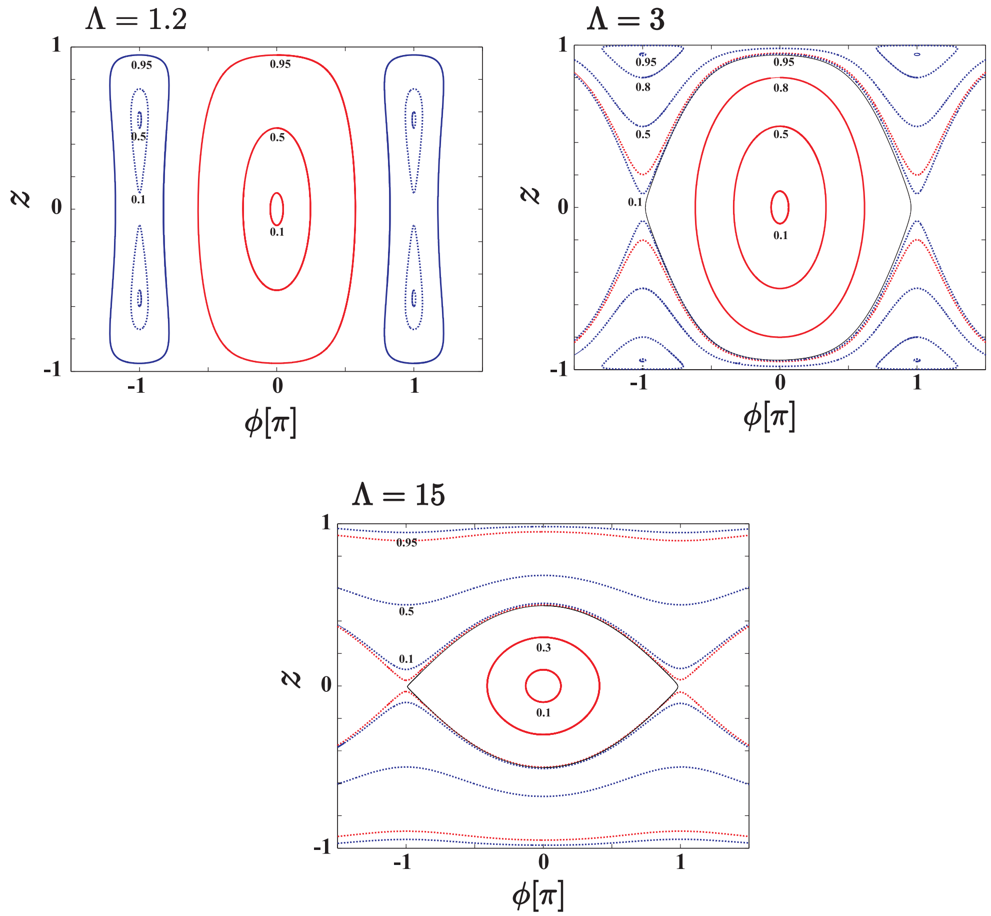

Figure 3.4: Phase-plane portrait of the bosonic Josephson junction in the two mode approximation for different scaled on-site interaction energies Λ. Trajectories with initial phase $\phi(0) = 0$ are depicted in red, those with $\phi(0) = \pi$ in blue. The self-trapped modes are drawn with dashed lines. The indicated numbers represent the different initial population imbalances $z(0)$. The black lines for $\Lambda = 3$ and $\Lambda = 15$ depict the respective separatrix, which is the phase-plane trajectory for $z(0) = z_c$.

For $\Lambda_c < \Lambda < \Lambda_{c,2}$ the system evolves in the regime of π-phase macroscopic self-trapping (yellow shaded region in graph 3.3). In this regime the phase is still localized around π while the population imbalance is locked with $\langle z \rangle \neq 0$. In the mechanical analogon of a nonrigid pendulum, this regime corresponds to a closed-loop trajectory around the vertical instable equilibrium. For $\Lambda > \Lambda_{c,2}$ the phase additionally becomes unbound (unshaded region). This regime is the same as the MQST regime discussed above for zero initial phase.

It is important to note, that the critical Λ_c for $\phi(0) = \pi$ is always between one and two, which means that for all $\Lambda > 2$ the system is always self-trapped. Therefore the small and large amplitude π-oscillation regimes are not accessible with our current setup, where a total number of atoms of $N_T = 1150$ corresponds to $\Lambda \approx 76$. This parameter only allows trajectories in the running phase MQST regime (see figure 3.3). Note that, as already mentioned for the zero-phase modes, the crossovers between different dynamical regimes can also be realized by fixing Λ and changing the initial population imbalance.

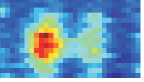

3.3.4 Phase plane portrait

The various regimes of the nonrigid pendulum dynamics discussed above can be summarized very intuitively in terms of a phase plane portrait, where constant energy lines are plotted in a z-ϕ diagram. Figure 3.4 shows phase space plots for different on-site interaction energies Λ, obtained by numerically solving the coupled differential equations 3.26. The first graph shows the accessible regimes for $\Lambda = 1.2$, where all trajectories with initial phase $\phi(0) = 0$ are untrapped, even for arbitrary large initial population imbalances $z(0)$. The situation changes for $\phi(0) = \pi$ where the transition to π-phase MQST occurs at $z_c \approx 0.75$. In the second graph the phase-plot is shown for $\Lambda = 3$. In this regime, a transition from zero-phase oscillations to MQST can be observed for initial zero phase if the initial population imbalance is increased above the critical value $z_c = 0.943$. The separatrix[8] is indicated with a thin black line. For an initial phase $\phi(0) = \pi$ all trajectories are self-trapped. The transition from running phase-MQST to π-phase MQST happens at $z_{c,2} \approx 0.75$. Finally, the third graph shows the various regimes for the scaled on-site interaction energy $\Lambda = 15$. The phase plot shows, that both regimes for zero initial phase, Josephson oscillations and MQST, are accessible. The transition occurs at $z_c \approx 0.5$. As we will see in chapter 5, this value is convenient for our experiments in order to investigate the two regimes. As already shown for $\Lambda = 3$, all trajectories for $\phi(0) = \pi$ are self-trapped. Unfortunately only the running-phase MQST regime would be accessible for our current experimental parameters, even if we were able to prepare a π initial phase.

3.3.5 Limits of the two-mode description

The two-mode approximation describes the system in terms of only two time-independent spatial modes, each of them localized inside a single well. These modes are calculated by linearly combining the symmetric and the antisymmetric groundstate of the Gross-Pitaevskii equation. This assumption implies that the many-body interactions produce only small modifications of the groundstate properties of the individual wells. This situation is surely encountered, if the on-site interaction energy is much smaller than the level spacing of the external trap, which leads to a coarse upper bound for the total atom number. In order to give a rough estimate of the maximum atom number, a harmonic approximation to the confinement inside a single well

$$V(\mathbf{r}) = \frac{1}{2} m(\omega_x^2 x^2 + \omega_y^2 y^2 + \omega_z^2 z^2) \tag{3.38}$$

is applied. Assuming, that the wavefunctions of the interacting atoms can still be described by the Gaussian groundstate for non-interacting atoms in the external harmonic confinement inside a single well[9], we obtain

$$\psi(\mathbf{r}) = \left(\frac{1}{\pi a_0^2}\right)^{3/4} e^{-\frac{1}{2}\left(\frac{x^2}{a_x^2}+\frac{y^2}{a_y^2}+\frac{z^2}{a_z^2}\right)} \tag{3.39}$$

---

[8] The separatrix is the trajectory for $z(0) = z_c$, which separates the different dynamical regimes

[9] This assumption overestimates the interaction energy since the real groundstate of the system is broadened due to the interatomic repulsion.

where $a_{x,y,z} = \sqrt{\hbar/m\omega_{x,y,z}}$ are the respective harmonic oscillator lengths and $\bar{a} = (a_x a_y a_z)^{1/3}$ is their geometric average. This leads to the on-site interaction energy of N particles inside a single well

$$U_{int} = Ng \int |\psi|^4 d\mathbf{r} = \frac{Ng}{(2\pi)^{3/2} r_0^3} \tag{3.40}$$

which has to be small compared to the level-spacing of the harmonic trap leading to the estimate

$$N \ll \sqrt{\frac{\pi}{2}} \frac{r_0}{a}. \tag{3.41}$$

For our experimental setup, the mean trapping frequency is on the order of 100 Hz corresponding to $r_0 \approx 1\,\mu$m which means

$$N \ll 200. \tag{3.42}$$

A numerical simulation (see section 3.6) of the localized mode yields an on-site interaction energy of $h \cdot 105$ Hz for $N = 700$ atoms inside a single well which shows that the expression given above indeed overestimates the interaction. Nevertheless, the requirements for the two-mode approximation to apply are not strictly fulfilled, since the minimum condensate atom number we can generate reproducibly is about $N_T = 1000$. Although the two-state model can not explain our experimental data quantitatively, it still provides an intuitive understanding of the various dynamical regimes.

Another approximation we applied to get the coupled two-mode differential equations 3.26 was the neglect of mixed interaction terms in equation 3.21, which led us to a constant tunneling energy K. An inclusion of the neglected terms still allows a similar description in terms of a set of two coupled differential equations involving only one additional physical quantity. This is shown in the next section, where a time-dependent tunneling energy is included. This small extension of the two-mode model provides surprisingly good quantitative agreement with the numerical solution and experimental results.

The two-mode description is based on the Gross-Pitaevskii equation and therefore does not take into account the effect of quantum fluctuations. These effects have been included for example in [31, 77, 78].

Additionally, the effect of thermal fluctuations due to the residual thermal cloud is neglected in the two-mode description presented here. However, as shown in [34] it can be included by means of a heuristic damping term in equation 3.26. The central result of this work is that damping produces characteristic decay trajectories to the final equilibrium $\phi = z = 0$ for all different dynamical regimes discussed above. Finite temperature effects have also been investigated in [32] where it has been assumed that the thermal cloud results in a non-coherent dissipative atomic current. Ruostekoski and Walls [79] have included the effect of thermal fluctuations by coupling the Bose-Einstein condensate to a thermal reservoir of non-condensed atoms. They also show, that on a time scale of several tunneling times, the self-trapped state decays to an equal population in both wells.

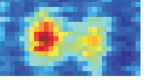

3.4 Extended two-mode approximation: variable tunneling model

As already discussed in section 3.3, the assumption of time-independent spatial wavefunctions and the neglect of mixed interaction terms led to a constant tunneling energy, which is a severe limitation for the description of real bosonic Josephson junctions. Stefano Giovanazzi *et al.* [76] have included the leading mixed interaction term already in 2000. Recently, David Ananikian and Tom Bergeman [80] have included all terms in equation 3.21 and derived differential equations for a more exact two-mode model that accounts for a variable tunneling rate depending on the instantaneous values of the population imbalance z and the relative phase ϕ. This model has been termed variable tunneling model (VTM) in contrast to the normal constant tunneling model (CTM) described above. The VTM assumes the same two-mode approximation (equation 3.18) as the CTM which implies time-independent local modes Φ_1 and Φ_2. These local modes are again calculated in terms of the symmetric ground state Φ_s and the first antisymmetric excited state Φ_{as} (see equation 3.20). However, this is the only assumption for the VTM and no further approximations are applied in this theory. This means in particular, that the tunneling parameter in front of Ψ_2 in equation 3.21 is no longer constant since it contains terms in Ψ_1 and Ψ_2 which are time dependent.

Despite the complexity of the additional terms compared to the CTM, the extended model leads to the following coupled set of differential equations for the symmetric double well case:

$$\begin{aligned} \dot{z}(t) &= -\sqrt{1-z^2(t)}\sin\phi(t) + \frac{C}{B}z\cos(2\phi) \\ \dot{\phi}(t) &= \frac{A}{B}z(t) + \frac{z(t)}{\sqrt{1-z^2(t)}}\cos\phi(t) - \frac{C}{B}z\cos(2\phi), \end{aligned} \tag{3.43}$$

where the time has been re-scaled as $\frac{B}{\hbar}t \to t$ and we have defined the following constants:

$$\begin{aligned} A &= \frac{1}{4}\cdot(10\gamma_{s,as} - \gamma_{s,s} - \gamma_{as,as}) \\ B &= \beta_{as} - \beta_s + \frac{1}{2}\cdot(\gamma_{s,s} - \gamma_{as,as}) \\ C &= \frac{1}{4}\cdot(\gamma_{s,s} - \gamma_{as,as} - 2\gamma_{as,as}) \end{aligned} \tag{3.44}$$

. Here $\beta_{s,as}$ represent the chemical potential of the states $\Phi_{s,as}$ and

$$\gamma_{i,j} = gN_T\int|\Phi_i|^2|\Phi_j|^2 d\mathbf{r}, \quad \text{for } i,j \in \{s, as\}. \tag{3.45}$$

Note, that all constants are expressed in terms of the symmetric and antisymmetric stationary states of the symmetric double well potential, instead of the localized modes used in the CTM.

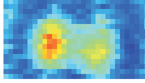

The differential equations 3.43 can be written in Hamiltonian form using the scaled Hamiltonian

$$H = \frac{A}{B}\frac{z^2}{2} - \sqrt{1-z^2}\cos\phi + \frac{1}{2}\frac{C}{B}(1-z^2)\cos(2\phi). \tag{3.46}$$

Equation 3.43 has a similar form as the analogous equations in the CTM. However, the additional term in C in the VTM can be significant for large atom numbers[10]. A direct comparison of the relevant constant parameters of the VTM and CTM yields:

$$\begin{aligned} 2K &= B - \frac{1}{4}(\gamma_{as,as} - \gamma_{s,s}) \\ N_T U &= A + 2C. \end{aligned} \tag{3.47}$$

The different parameters are calculated as a function of the total atom number in [80]. The authors show that the interaction effects are better captured by the VTM than by the CTM especially for large atom numbers. In particular, K can become negative which implies imaginary plasma-oscillation frequencies, whereas B is shown to be positive for all atom numbers.

A very important parameter for the experimental implementation of a bosonic Josephson junction is the critical population imbalance z_c, which constitutes the transition between Josephson tunneling and self-trapping regime. The value for z_c can be obtained by equating $H(0,\pi) \equiv H(z_c, 0)$ using the same arguments as in section 3.3:

$$z_{c,VTM} = \frac{2}{A-C}[B(A-B-C)]^{1/2}. \tag{3.48}$$

In order to compare the two different two-mode approaches and the numerical integration of the non-polynomial nonlinear Schrödinger equation[11], the group of Tom Bergeman has numerically calculated the ground state and the first excited antisymmetric state of the 3d-Gross-Pitaevskii equation for our experimental atom number $N_T = 1150$ and double well potential. The numerical integration has been implemented by diagonalizing the DVR Hamiltonian [81] using sparse matrix techniques [82]. The results for the relevant parameters are $A = 2.377$, $B = 0.073$, $C = 0.0046$, $K = 0.0156$ and $\Lambda = 76$. The critical population imbalance given by equation 3.48 for self-trapping within the VTM is $z_c \approx 0.35$ which is in good agreement with the value $z_c = 0.39$ obtained by integration of the three-dimensional Gross-Pitaevskii equation. The corresponding phase-plane trajectories for the indicated initial population imbalances are shown with blue lines in figure 3.5 and are compared to the results from a numerical integration of the NPSE (red lines). The two predictions are in excellent agreement for small population imbalances $z(0) < 0.4$. However, in the self-trapped regime the VTM slightly deviates from the numerical solution. This can be explained by realizing, that for $z(0) = 0.7$ the chemical potential of the BEC is already on the order of $\mu = h \cdot 300\,\text{Hz}$. This is is approximately half a harmonic oscillator level spacing above the potential barrier, which

---

[10] In this context large means that the scaled interaction gN is bigger than unity, where the scattering length a is given in units of the oscillator length inside the harmonic trap in x-direction and we have set $\hbar = m = 1$. In our experimental realization: $gN \approx 60$.

[11] The details of the numerical methods are discussed in section 3.6.

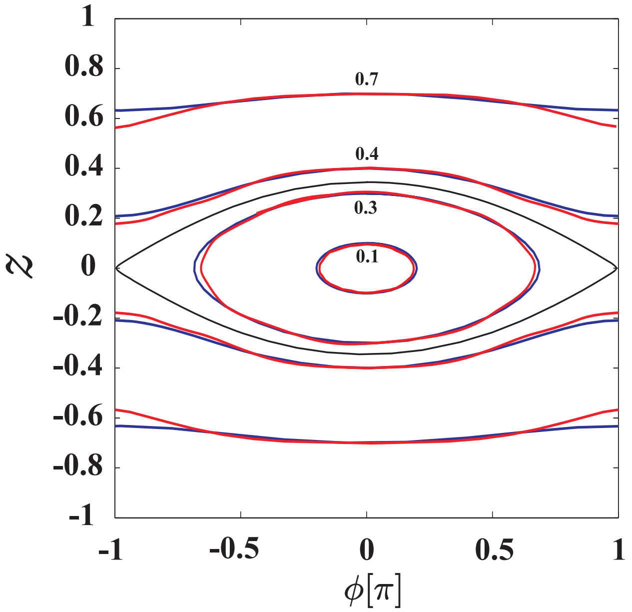

Figure 3.5: Phase plane trajectories for the variable tunneling model (blue lines) and the numerical solution of the non-polynomial nonlinear Schrödinger equation (red lines) for our experimental parameters. The indicated numbers denote the initial population imbalances. The black line shows the separatrix for the VTM at $z_c = 0.35$. The two theoretical predictions show good quantitative agreement.

has a height of $V_b = h \cdot 263\,\mathrm{Hz}$. Therefore the BEC can couple to excited states of the external potential and the assumption of only two modes is no longer strictly valid. Note that the numerically calculated value $\Lambda = 76$ corresponds to a critical population imbalance of $z_{c,CTM} = 0.23$ in the framework of the CTM. This shows, that the usual two-mode approximation fails for the experimentally implemented parameters.

The phase-plane plots do not show the time-scale of the ongoing dynamics. A comparison of the predicted tunneling times as a function of the total atom number in the Josephson tunneling regime ($z(0) = 0.28$) is shown in figure 3.6. The CTM, VTM and a full numerical solution of the 3d-Gross-Pitaevskii equation (TDGPE) with our experimental parameters are taken from [80]. The additional green crosses show our numerical solution of the nonlinear non-polynomial Schrödinger equation for the same parameters. This graph shows again the advantage of the VTM compared to the normal CTM especially for large atom numbers. The main feature of the graph is, that for atom numbers up to 100 all four different theoretical curves predict the same tunneling time. For larger atom numbers, the CTM begins to fail, since the dynamics becomes self-trapped even at $z(0) = 0.28$. The VTM and the numerical integration of the TDGPE and the NPSE predict the same tunneling time up to 1500 atoms with a deviation below 12%. All three theories can explain our experimentally measured tunneling time indicated with the red square and error bars. Note that the deviation of the NPSE compared to the GPE is below 2% in the complete range of considered atom numbers.

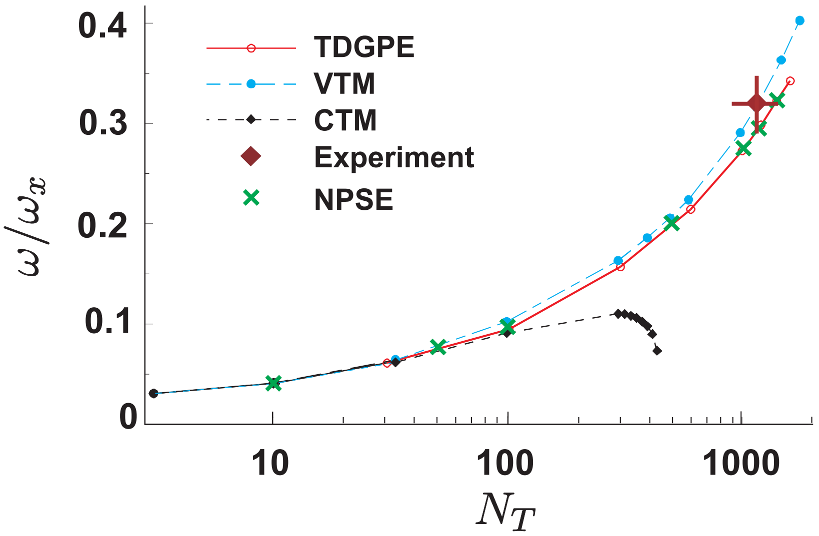

Figure 3.6: Comparison of the calculated Josephson tunneling times using the CTM, VTM and the numerical integration of the TDGPE and NPSE. The tunneling frequencies are given in units of the frequency of the harmonic confinement in x-direction ($\omega_x = 2\pi \cdot 78\,\mathrm{Hz}$, see the definition of the potential 3.17). All theoretical predictions agree for atom numbers below 100. For larger atom numbers, the CTM fails, whereas the VTM still predicts the right tunneling frequency. The red square and error bars indicate the tunneling time deduced from our experiment. This graph is taken from [80] except the points for the NPSE.

3.5 External and internal bosonic Josephson junctions

In the discussion of the Josephson dynamics given above, the weak link between two Bose-Einstein condensates was provided by loading a BEC into an external double well potential (external Josephson effect) with a small spatial wavefunction overlap. The experimental implementation of this system will be presented in chapter 4. However, it is also possible to provide the weak link using a two-component Bose-Einstein condensate consisting of two different hyperfine levels trapped inside a single harmonic trap. The weak coupling between two wavefunctions, i.e. the two hyperfine states, is provided by a weak driving field (internal Josephson effect). This coupling, which results in a transfer from one internal state to the other can be done in a coherent manner, so that the phases of the two condensates couple.

The first Experiment with a two-component BEC was performed in 1997 [83] with ^{87}Rb atoms evaporatively cooled in the $|F = 1, m_F = -1\rangle$ spin state. Those atoms cool an additional cloud in the $|2, 2\rangle$ state by sympathetic cooling[12]. However, this experiment can not produce arbitrary relative atom numbers in the two states. In 1998, the same group has succeeded in using a coherent two-photon transition consisting of a microwave photon, which is a few MHz red detuned from the hyperfine transition with $\nu_0 \approx 6.8\,\mathrm{GHz}$ and a radio frequency photon of 1-4 MHz to convert an arbitrary fraction of a $|1, -1\rangle$ condensate to the $|2, 1\rangle$ state [84, 36]. In this experiment, the coherence between the two states has been shown explicitly by measuring the relative phase of the two condensates using a technique based on Ramsey‘s method of separation [85].

---

[12] Sympathetic cooling means that a cloud of atoms is cooled by thermal contact with a colder sample. This technique has allowed the experimental realization of quantum degenerate Fermi gases.

Note that in the absence of the coupling drive, interconversion between the two species is negligible. Motivated by the experimental implementation of the coupling of different hyperfine states, Williams *et al.* [35] investigated the possibility of creating Josephson-type oscillations in two-component Bose-Einstein condensates. The proposed experiment starts with a short driving pulse that produces condensates in both states with a defined relative population imbalance $z(0)$. Due to the different magnetic moments of the two spin states and the presence of the earth gravitational field, the two clouds see different harmonic traps, separated along the direction of gravity. After a given time which is determined by the transient motion of the two clouds to the new equilibrium position, a weak driving field is turned on, coupling the two condensates in the overlap region, which can be controlled by the magnetic confinement [36]. The time, at which this drive is turned on determines the initial relative phase $\phi(0)$ of the internal Josephson junction.

As shown in [35] the dynamics of the system in the two-mode approximation

$$\Psi = \sqrt{N_1(t)}e^{i\phi_1(t)}\Phi_1(\mathbf{r}) + \sqrt{N_2(t)}e^{i\phi_2(t)}\Phi_2(\mathbf{r}) \tag{3.49}$$

is governed by the following coupled differential equations

$$\begin{aligned} \dot{z}(t) &= -\sqrt{1-z^2(t)}\sin\phi(t) \\ \dot{\phi}(t) &= -\frac{[\mu_1-\mu_2+\delta]}{K} + \frac{z(t)}{\sqrt{1-z^2(t)}}\cos\phi(t), \end{aligned} \tag{3.50}$$

where δ is the detuning of the two-photon drive with respect to the energy separation of the two hyperfine states, K is the tunneling energy in units of $\hbar$ and $\mu_{1,2}$ are the chemical potentials of the two modes Φ_1 and Φ_2, which are assumed to be time-independent[13]. In order to make equation 3.50 look similar to the differential equations 3.26 of the two-mode approximation discussed above, I have re-scaled the time according to $t \rightarrow Kt$. Equation 3.50 is a nonlinear version of the usual Josephson equation and is very similar to the two-mode differential equation 3.26 for the external bosonic Josephson junction. Note, that in contrast to the two-mode approximation for two BECs in a double well trap described above, where we have only included the on-site interaction terms, the interaction between the two condensates has to be included in the internal Josephson junction, since the wavefunctions have significant spatial overlap. To my knowledge, the internal Josephson effect has not been experimentally realized so far.

3.6 Numerical solution

As we have seen in section 3.3 the constant tunneling two-mode approximation qualitatively describes the different dynamical regimes of the bosonic Josephson junction in terms of only two physical parameters Λ and K. In order to check the validity of the CTM and VTM, we have to compare it to a numerical simulation. This chapter deals with the numerical solution of the Gross-Pitaevskii equation and the non-polynomial nonlinear Schrödinger equation.

---

[13] The assumption of time-independent spatial wavefunctions and chemical potentials is often referred to as adiabatic approximation.

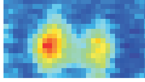

3.6.1 Split-step Fourier method

The numerical integration of the GPE (equation 3.11) and the NLSE (equation 3.16) is performed by applying the infinitesimal time evolution operator $\hat{U}(dt)$ to the wavefunction in each infinitesimal time step dt:

$$\Psi(x, t + dt) = \hat{U}(dt)\Psi(x, t) \tag{3.51}$$

For the case of a time-independent Hamiltonian $\hat{H}$, $\hat{U}(dt)$ is simply given by

$$\hat{U}(dt) = e^{-\frac{i}{\hbar}\hat{H}dt}. \tag{3.52}$$

In order to apply this time evolution operator, we split the Hamiltonian into a kinetic part $K(\hat{p}) = \frac{\hat{p}^2}{2m}$ and a spatially and time-dependent part $S(\hat{\mathbf{r}}, t)$, which is given by

$$S(\hat{\mathbf{r}}, t) = V_{\text{ext}}(\hat{\mathbf{r}}) + gN|\Psi|^2 \tag{3.53}$$

for the three-dimensional Gross-Pitaevskii equation and by

$$\begin{aligned} S(\hat{x}, t) &= V_{\text{ext}}(\hat{x}) + g_{1d}N\frac{|\Psi(x,t)|^2}{\sqrt{1 + 2aN|\Psi(x,t)|^2}} \\ &+ \frac{\hbar\omega_\perp}{2}\left(\frac{1}{\sqrt{1 + 2aN|\Psi(x,t)|^2}} + \sqrt{1 + 2aN|\Psi(x,t)|^2}\right) \end{aligned} \tag{3.54}$$

for the NPSE.

The infinitesimal time evolution is symmetrically separated in order to evaluate $K(\hat{p})$ in momentum space and $S(\hat{x}, t)$ in coordinate space:

$$\hat{U}(dt) \approx e^{-\frac{i}{\hbar}K(\hat{p})\frac{dt}{2}} e^{-\frac{i}{\hbar}S(x,t)dt} e^{-\frac{i}{\hbar}K(\hat{p})\frac{dt}{2}}. \tag{3.55}$$

This separation introduces an error on the order of dt^3 since $\hat{x}$ and $\hat{p}$ do not commute[14] [86]. However, this error can be neglected by choosing dt sufficiently small. The whole operator is now applied to the wavefunction in the following way[15]:

$$\Psi(x, t + dt) = F^{-1}e^{-\frac{i}{\hbar}\frac{p^2}{2m}\frac{dt}{2}}Fe^{-\frac{i}{\hbar}V(x,t)dt}F^{-1}e^{-\frac{i}{\hbar}\frac{p^2}{2m}\frac{dt}{2}}F\ \Psi(x, t), \tag{3.56}$$

where the symbol F represents a Fourier transformation. This way to integrate the Schrödinger equation is called split-step Fourier method and allows a time propagation, which only uses multiplication and Fourier transformation of the wavefunction. We use a typical time resolution of $1\,\mu$s, which is chosen such, that the maximum phase evolution per integration step satisfies $|\frac{i}{\hbar}\hat{H}dt|_{\text{max}} \ll 2\pi$.

---

[14] If we had split the time evolution operator simply into two parts in momentum and coordinate space, the error would be on the order of dt^2.

[15] This is possible since the momentum operator is diagonal in momentum space and the coordinate operator is diagonal in coordinate space.

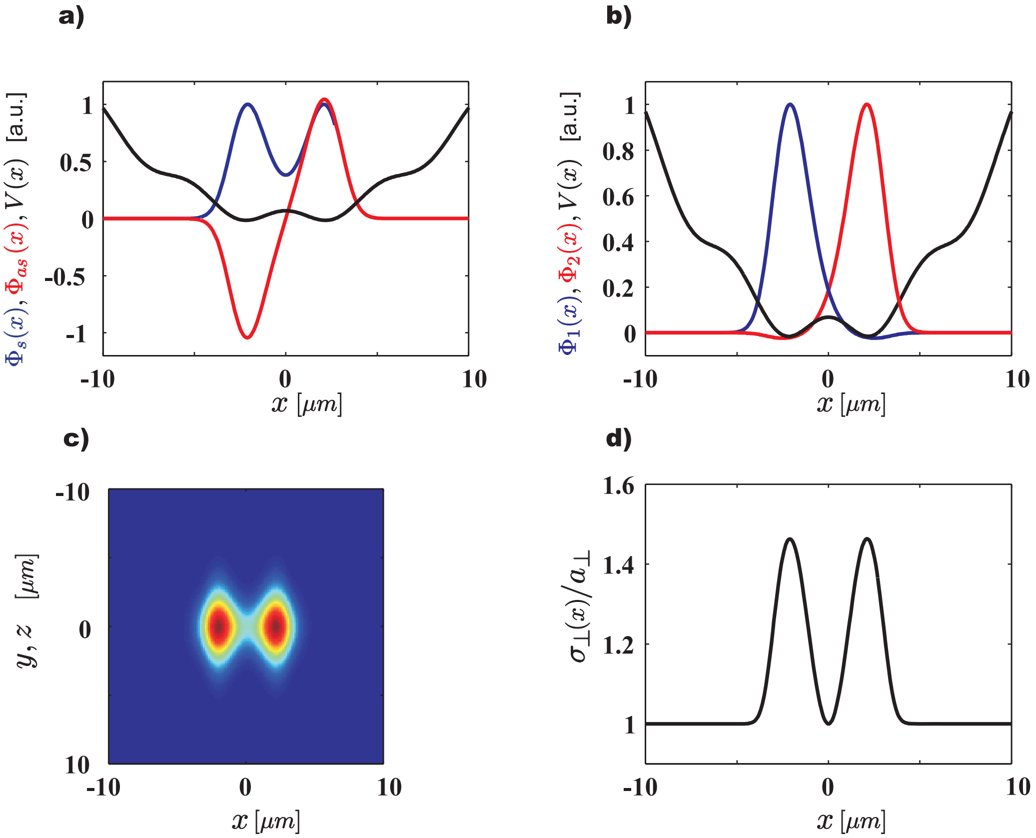

Figure 3.7: Numerical integration of the NPSE in imaginary time for $N_T = 1150$ atoms. a) Symmetric ground state (blue) and first excited antisymmetric state (red) of the symmetric effective double well potential (black). b) Localized modes in the left (blue) and right (red) well. c) Two-dimensional plot of the ground state wavefunction. d) Transverse RMS-width of the BEC scaled in units of the transverse ground state oscillator length.

3.6.2 Ground state: imaginary time propagation

In order to numerically investigate the Josephson dynamics of the Bose-Einstein condensate in the realized potential, we first have to calculate the initial wavefunction, which is given by the groundstate in the three-dimensional double well potential. A very effective way to calculate groundstate wavefunctions is the method of numerical propagation in imaginary time [87]. The Gross-Pitaevskii equation (or alternatively the non-polynomial nonlinear Schrödinger equation) is hereby changed into a diffusion equation by applying a Wick rotation

$$t \rightarrow \tau = -it. \tag{3.57}$$

This transformation results in the necessary energy diffusion but also in a loss of atoms, which can be compensated by a re-normalization of the wavefunction in each integration step. As a starting wavefunction for the imaginary time propagation we take an analytical approximation to the ground state (Thomas Fermi parabola or Gaussian ground state) and use the split-step Fourier method (with $dt \rightarrow -i\,dt$).

If the chosen initial wavefunction is sufficiently close to the real ground state and if we choose a sufficiently small imaginary time step $i\,dt \approx i \cdot 5\,\mu$s the wavefunction converges

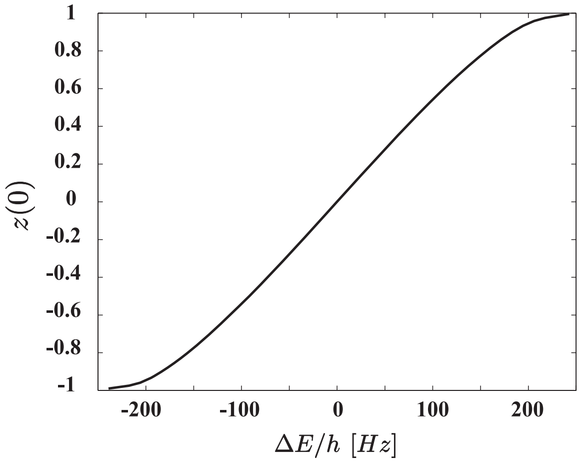

Figure 3.8: Ground state population imbalances as a function of the energy difference ΔE of the two wells. The symmetric double well potential corresponds to $\Delta E = 0$

quickly to the ground state within a few $i\cdot$ ms. A very useful feature of the imaginary time propagation is, that it converges to the first excited antisymmetric state in the double well potential, if we start with an appropriate antisymmetric initial wavefunction. We need both, the symmetric and the first excited antisymmetric state in order to calculate the localized modes Φ_1 and Φ_2 used for the two-mode approximation described in section 3.3.

3.6.3 Numerical results: stationary states

The symmetric and antisymmetric stationary states of the ^{87}Rb BEC in the considered external double well potential are calculated using imaginary time propagation of the NPSE. The considered coordinate space has a total size of $50\,\mu$m and is divided into 2048 spatial steps of 24.4 nm. The chosen potential has the following form

$$V(x,y,z) = \frac{1}{2}m(\omega_x^2 x^2 + \omega_y^2 y^2 + \omega_z^2 z^2) + V_0 \cos^2(\pi(x-\Delta x)/q_0)^2, \tag{3.58}$$

where $\omega_x = 2\pi \cdot 78\,\mathrm{Hz}$, $\omega_y = 2\pi \cdot 66\,\mathrm{Hz}$ and $\omega_z = 2\pi \cdot 90\,\mathrm{Hz}$ are the harmonic trapping frequencies, $q_0 = 5.2\,\mu$m is the periodicity and $V_0 = h \cdot 413\,\mathrm{Hz}$ the potential depth of the optical lattice. For this set of parameters, the distance of the two wells is $d = 4.2\,\mu$m and the potential barrier has a height of $V_b = h \cdot 263\,\mathrm{Hz}$. A nonzero shift Δx of the harmonic confinement in x-direction with respect to the periodic potential results in an asymmetric double well, for which the two wells have an energy difference $\Delta E \neq 0$. Figure 3.7 shows the numerical results for 1150 atoms in a symmetric double well potential ($\Delta_x = 0$). The symmetric ground state and the first excited antisymmetric state are shown in graph 3.7a. The numerical integration yields the chemical potentials $\beta_s = h \cdot 279.7\,\mathrm{Hz}$ and $\beta_{as} = h \cdot 289.5\,\mathrm{Hz}$. The two localized modes Φ_1 and Φ_2, which are the starting point for the two-mode models are shown in graph b). A two-dimensional plot of the ground state wavefunction is shown in graph c)[16]. The reason why the effective one-dimensional NPSE is sufficient to describe the physics in the considered regime is shown in figure

---

[16] Note that the transverse shape of the wavefunctions is restricted to be Gaussian in the NPSE.

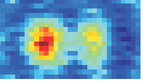

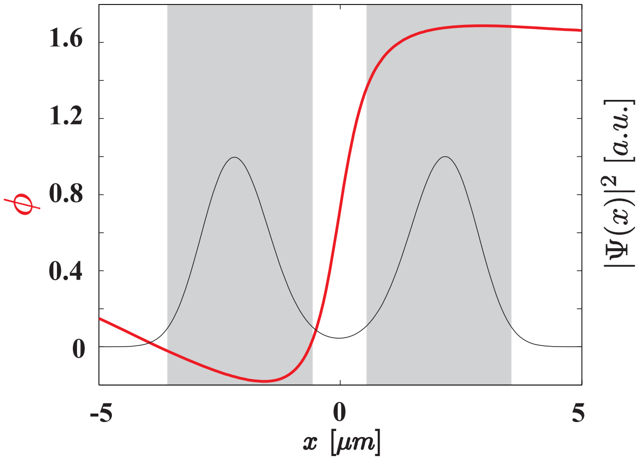

Figure 3.9: Quantum phase of the wavepacket after one quarter of the oscillation period. The phases of the two localized modes and therefore the relative phase are obtained by taking the unweighted mean value over the shaded regions, where the atomic density (black line in arbitrary units) is at least ten percent of the maximum inside the respective well.

3.7d, where the scaled transverse RMS-width of the groundstate is plotted as a function of x. It shows, that the atomic cloud is nearly in the transverse groundstate of the external potential.

The preparation of the initial population imbalance can be implemented by choosing an asymmetric double well with a non-zero energy difference ΔE of the two wells. The resulting atom number inside each well is obtained by integrating the atomic density using $N_1 = \int_{-\infty}^{0} |\Psi|^2 dx$ and $N_2 = \int_{0}^{\infty} |\Psi|^2 dx$. Figure 3.8 shows the corresponding groundstate population imbalances z as a function of the energy shift ΔE.

3.6.4 Numerical results: dynamics

The numerical integration of the NPSE using the split-step Fourier method is carried out for the same potential and atom number and with the same numerical parameters as given above. As a starting wavefunction, we use the ground state wavefunction in an asymmetric double well potential. The potential is subsequently shifted to the symmetric case, which initiates the Josephson tunneling dynamics. This shift is applied non-adiabatically[17] in order to prevent atomic tunneling during the shifting process.

As we have seen in the previous chapters, the dynamics of the system can be characterized by the evolution of the two dynamical parameters, the population imbalance z and the relative phase ϕ.

The phase of the wavepacket is calculated using the relation

$$\phi(x) = \arctan\left(\frac{\mathrm{Im}(\Psi(x))}{\mathrm{Re}(\Psi(x))}\right). \tag{3.59}$$

Figure 3.9 shows a typical spatial distribution of the numerically calculated phase (red line) and the corresponding atomic density (black line) of the BEC after a quarter of

---

[17] In this context, non-adiabatically means that the shifting process is much faster than the tunneling time scale, which is typically on the order of 50 ms.

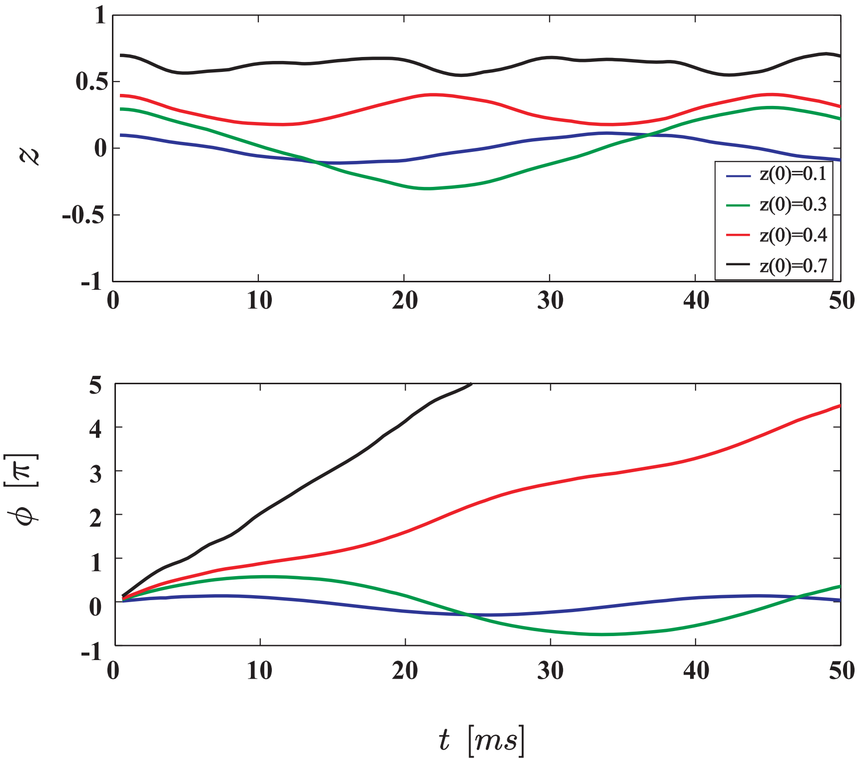

Figure 3.10: Result of the numerical integration of the NPSE for $N_T = 1150$ atoms in the experimentally realized double well potential. The time evolution of the two dynamical variables z and ϕ is shown for different initial population imbalances as indicated in the legend. The dynamics shows Josephson tunneling for $z(0) < z_{c,NPSE} = 0.375$ and self-trapping for $z(0) > z_c$.

the oscillation period. The assumption of a constant phase inside a single well, which is crucial for the two-mode description discussed above, is justified by the numerical calculation. Since the expression for the phase (equation 3.59) diverges for small real parts of the wavefunction, the phases of the BECs in the left and right well are calculated by taking the mean value over a spatial region, where the atomic density is bigger than ten percent of the respective maximum (gray shaded regions). The relative phase of the two localized modes in figure 3.9 is $\phi \approx \pi/2$.

The results of the time evolution of z and ϕ in the different dynamical regimes are shown in figure 3.10. The different lines correspond to different initial asymmetries and therefore to different initial population imbalances as indicated in the graph. Note that the initial relative phase of the two wavepackets is zero for all curves, since the propagation starts with the groundstate of the shifted potential. As predicted by the two-mode models, the system shows two distinct dynamical regimes: Josephson tunneling and macroscopic quantum self-trapping. The numerical integration of the NPSE yields a critical value $z_{c,NPSE} = 0.375$ for the initial population imbalance, which is in good agreement with the value $z_{c,TDGPE} = 0.39$ given in [80] obtained by integrating the full three-dimensional Gross-Pitaevskii equation. For $z(0) < z_c$ the system evolves in the Josephson-tunneling regime which is characterized by an oscillating population imbalance and a relative phase with zero time-average. The self-trapping regime for $z(0) > z_c$ manifests itself in a monotonically increasing phase and a locked population imbalance. In this regime, the tunneling of atoms can no longer counteract the evolution of the

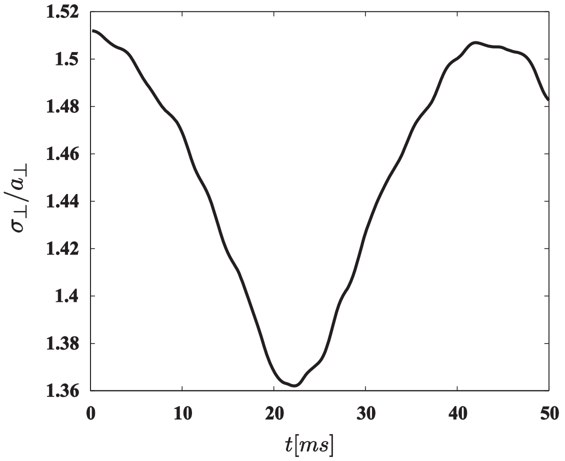

Figure 3.11: Time evolution of the transverse RMS-size of the left localized mode in the Josephson oscillation regime ($z(0) = 0.3$). The fact, that the spatial extent of the wavepacket does not change significantly during the tunneling evolution justifies the two-mode ansatz, which assumes time-independent spatial wavefunctions Φ_1 and Φ_2.

relative phase due to different on-site interaction energies leading to relative phases of $\phi > \pi$. As we will see in chapter 5, this numerical solution is in excellent agreement with our experimental results.

The two-mode model as well as the extended two-mode model assume time-independent localized modes. In order to check this assumption, I have numerically calculated the time evolution of the transverse size of the left mode in the Josephson-tunneling regime for $z(0) = 0.3$. The result is shown in figure 3.11 and reveals that in fact, the transverse wavepacket size only shows an evolution on the order of ten percent although the atom number in this well oscillates between $N_1 = 750$ and $N_1 = 400$. This explains the good agreement between the extended two-mode model described in section 3.4 and our experimental findings, since the assumption of a constant spatial wavefunction and a constant phase inside a single well are the only approximations in this approach.

3.7 Feasibility study for bosonic Josephson junction experiments

The numerical simulations in chapter 3.6 have shown the existence of a set of parameters, in which both dynamical regimes, Josephson tunneling and macroscopic quantum self-trapping are in principle accessible. However, for a successful experimental implementation of a bosonic Josephson junction it is important to choose a set of parameters, which is sufficiently uncritical to small deviations. For this purpose numerical simulations based on the NPSE have been performed for different periodicities q_0 of the periodic potential in equation 3.58 realizing the effective double well structure. The three-dimensional harmonic confinement in 3.58 is fixed to $\omega_x = 2\pi \cdot 78\,\text{Hz}$, $\omega_y = 2\pi \cdot 66\,\text{Hz}$ and $\omega_z = 2\pi \cdot 90\,\text{Hz}$ for all calculations. For each choice of q_0, the remaining two free parameters have been varied: the total atom number N_T and the depth V_0 of the periodic potential, which is directly coupled to the barrier height V_b. A combination of N_T and V_0 is considered to

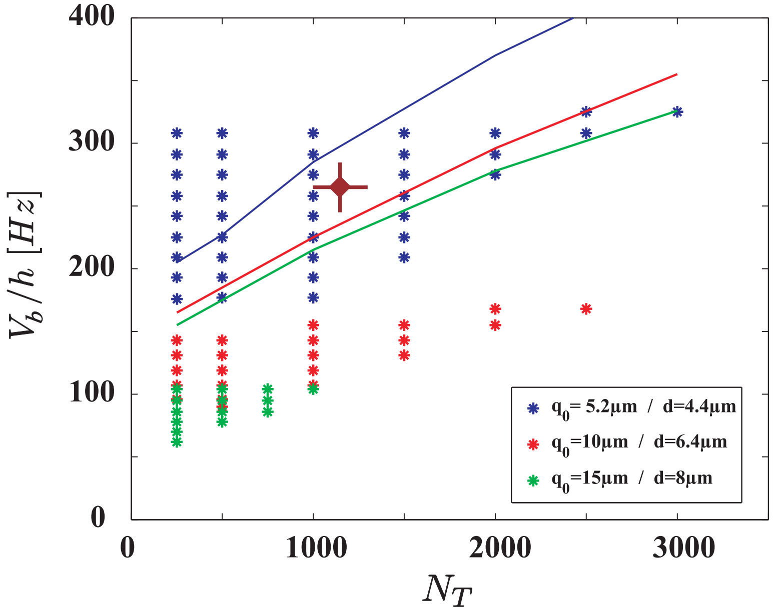

Figure 3.12: Parameter space for a possible experimental implementation of a bosonic Josephson junction. Each point corresponds to a combination of the total atom number N_T and barrier height V_b, where both dynamical regimes are observable. The dark red square and errorbars indicate the parameter regime, in which our experiments have been performed. The solid lines represent combinations of the atom number and potential depth, for which the chemical potential of the BEC coincides with the potential barrier.

be appropriate, if the following conditions are fulfilled:

- First, both regimes - Josephson oscillations and self-trapping - should be experimentally accessible by varying the initial population imbalance z(0). Since the preparation of very small and the quantitative analysis of very large population imbalances are very difficult (see chapter 5), the transition between the two regimes should occur at a critical value $0.3 < z_c < 0.6$.
- A second condition is, that the tunneling time scales have to be much smaller than the lifetime of the BEC, which is on the order of a few seconds. Therefore, only tunneling dynamics with a period of less than 500 ms are taken into account.

The results of this feasibility study for a ^{87}Rb BEC are shown in figure 3.12 for three different lattice spacings $q_0 = 5.2\,\mu$m, $10\,\mu$m and $15\,\mu$m, corresponding to an effective double well spacing of $d = 4.4\,\mu$m, $6.4\,\mu$m and $8\,\mu$m. Each point in the graph represents an appropriate combination of the two parameters N_T and V_b.

The lower bound for the potential barrier heights V_b for given q_0 and N_T is determined by the fact, that the chemical potential is too far above the potential barrier between the two wells, which means that atoms can reach the less occupied well by moving over the barrier. In this case, the distribution is not self-trapped even for huge initial population imbalances. The solid lines represent combinations of the atom number and barrier heights, for which the chemical potential of the BEC coincides with the potential barrier. A comparison of these lines with the lower bound of the calculated points

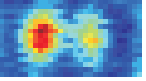

shows, that the regime of self-trapping is still accessible, if the chemical potential is up to typically 100 Hz above the barrier.

The upper bound is determined by the fact, that the potential barrier is too large to allow for tunneling with $z(0) \geqq 0.3$, which makes the Josephson tunneling-regime inaccessible experimentally.

The feasibility study shows, that Josephson junction experiments have to be performed with very small total atom numbers on the order of[18] $N_T \approx 1000$. The appropriate parameter space gets smaller for increasing lattice spacings and is experimentally inaccessible for $d > 8\,\mu$m. On the other hand, our imaging system with a resolution of $2.7(2)\,\mu$m restricts the double well spacing to be at least $4\,\mu$m in order to be able to quantitatively analyze the ongoing tunneling dynamics. The combination of the ability to reproducibly produce BECs consisting of 1150(150) atoms with our imaging resolution have made it possible to observe the bosonic Josephson junction dynamics for $q_0 = 5.2\,\mu$m in the parameter regime indicated with the dark red square and error bars in figure 3.12.

---

[18] The reproducible realization of such small BECs is one of the experimental problems one has to face in order to realize a bosonic Josephson junction. A realization of a smaller s-wave scattering length using a Feshbach resonance would allow for higher total atom numbers.

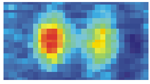

4 Experimental setup and procedure

In this chapter, an overview of the apparatus we use for the realization of Bose-Einstein condensation and for the performed Josephson junction experiments is presented. A detailed description of our experimental setup can be found in previous diploma and PhD theses [74, 88].

In order to cool atoms to quantum degeneracy, a combination of different experimental techniques is required. The atomic sample has to be isolated from the environment. Therefore the experiment has to be performed in ultra-high vacuum (UHV) conditions. The rubidium atoms are trapped and pre-cooled in a magneto-optical trap (MOT). They are subsequently loaded into a magnetic time orbiting potential (TOP) trap, where the first stage of evaporative cooling is performed. The quantum phase transition to Bose-Einstein condensation is finally reached after loading the sample into a crossed optical dipole trap consisting of two focused laser beams and performing a second evaporation stage. The Bose-Einstein condensate is subsequently loaded into an optical effective double well trap. This realizes a weak link of two BECs, which is the analog of the superconductive Josephson junction.

A schematic overview of the experimental setup is given in figure 4.1. It is divided into two parts: the laser setup at the top and the darkened area at the bottom of the graph, where the Bose-Einstein condensation of ^{87}Rb is realized. The different lasers produce light for cooling, trapping and absorption imaging of the atomic sample. The frequency as well as the power of the light, which is coupled into individual optical fibres can be adjusted by acousto-optical modulators (AOMs). Mechanical shutters in front of each optical fibre and a curtain around the vacuum chamber hold off residual near-resonant light, which could heat up the atomic cloud. The Bose-Einstein condensate is produced in the glass cell in the lower right part of figure 4.1, where the MOT, the TOP-trap, the dipole trap and the double well potentials are overlapped. For the sake of clarity, figure 4.1 does not contain details of the optical, electronic and mechanical setup.

The relevant parts of the experimental setup and the sequence which is used for cooling the atoms to quantum degeneracy will be discussed in the following sections.

4.1 Laser system

We use four laser systems for Bose-Einstein condensation and the realization of the optical double well potential:

- The titanium sapphire laser Ti:Sa I (Coherent, Monolithic-Block-Resonator 110)

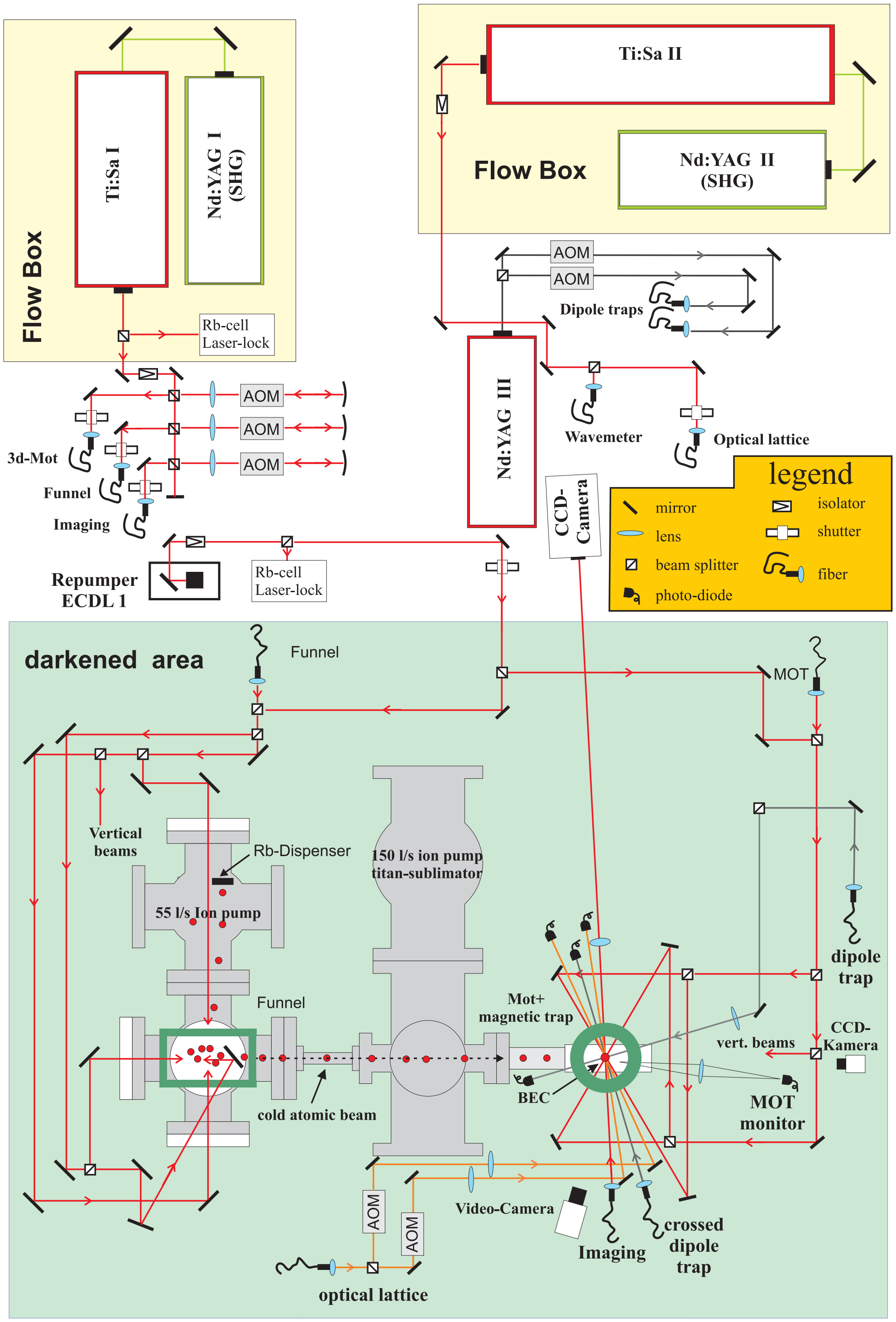

Figure 4.1: Schematic overview of the experimental setup: the upper part contains the laser systems for cooling, trapping and absorption imaging of the atomic sample. The green part is darkened by a curtain in order to prevent scattering of near-resonant photons. Bose-Einstein condensation is reached in an optical crossed dipole trap after a pre-evaporation cooling stage in the magnetic TOP trap.

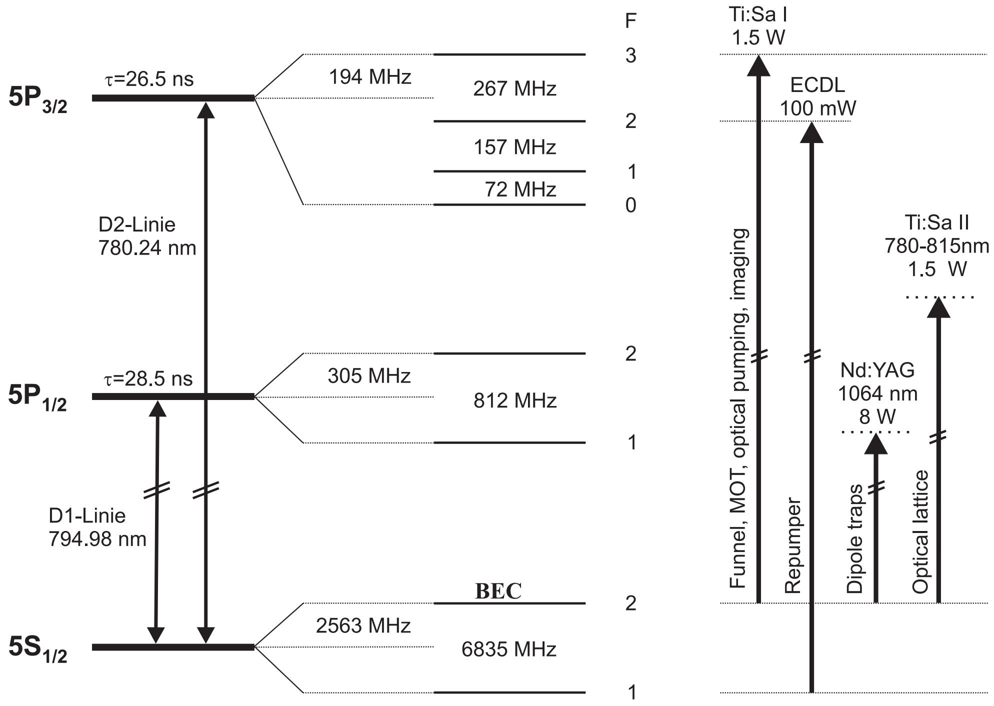

Figure 4.2: Hyperfine-structure of ^{87}Rb and employed laser wavelengths. The Bose-Einstein condensate is produced in the $5S_{1/2}\, F = 2, m_F = 2$ state.

is pumped by a frequency-doubled diode laser pumped Nd:YAG Laser (Coherent, Verdi V10) with 10 W optical output power. The Ti:Sa has a typical output power of 1.5 W. It is locked to the $(F = 2 \longrightarrow F' = (3,1))$ crossover transition of the D_2 line of ^{87}Rb. The light is divided into three parts for the funnel, the magneto-optical trap (MOT) and the absorption imaging beam. The different parts pass individual acousto-optic modulators, since the wavelengths for the MOT, funnel and imaging beam have to be slightly different. The imaging beam is exactly shifted to the $(F = 2 \longrightarrow F' = 3)$ transition, whereas the funnel and the MOT have a detuning of a few MHz.

- An external cavity diode laser (ECDL, 100 mW output power) in Littrow configuration is locked to the $(F = 1 \longrightarrow F' = 2)$ transition of the D_2-line. It is used to repump atoms, which have decayed into the $5S_{1/2}$ state back to the MOT circuit. This laser is often referred to as “repumper”.

- The diode laser pumped Nd:YAG III laser (Spectra-Physics, T40-X30-106QW) with a wavelength of 1064 nm and a maximum output power of 8 W provides the light for the optical dipole traps. The maximum power in the TEM00-mode, which can be coupled into the single mode fibre, is 3 W.

- The light for the optical lattice, which is superimposed on the optical dipole trap and creates the double well potential, is provided by a second titanium sapphire

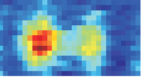

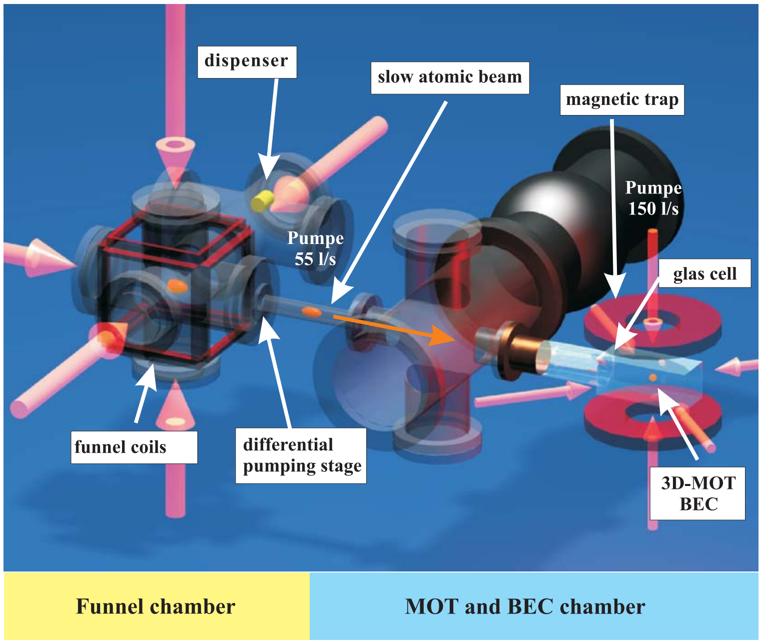

Figure 4.3: Overview of the vacuum setup. It consists of two chambers, which are connected by a differential pumping stage. The atomic funnel which is operated at a pressure of $\approx 10^{-9}$ mbar creates a slow atomic beam which passes the differential pumping stage and is captured by the MOT, where the pressure is below 10^{-11} mbar.

laser Ti:Sa II (Coherent, 899). This laser is also pumped by a Coherent Verdi V10 and is operated at a typical wavelength of approximately 810 nm and an output power of 1.5 W.

The relevant atomic levels of ^{87}Rb and the wavelength of the different lasers used for cooling, trapping and imaging are shown in figure 4.2.

4.2 Vacuum, funnel and MOT

In order to thermally isolate the cooled atomic cloud from the “hot” environment, an ultrahigh vacuum chamber is indispensable. A pressure below 10^{-11} mbar is required in order to be sure, that scattering with background gas atoms does not affect the condensation process and the lifetime of the Bose-Einstein condensate in the optical trap. On the other hand, the loading rate of a magneto-optical trap is proportional to the partial pressure of rubidium, which should therefore not be below 10^{-9} mbar. We therefore use a double MOT setup and a vacuum system consisting of two chambers which are connected by a differential pumping stage. The schematics of the vacuum setup is shown in figure 4.3.

In our experiment, dispensers are used as source of atomic rubidium. The partial pressure of rubidium in the funnel chamber can be adjusted by the electric current through the dispensers. The atomic funnel [89] is loaded from the background gas and produces a cold continuous atomic beam, which passes the differential pumping stage and is captured by the three-dimensional MOT [90] in the glass cell. The typical loading rate of the MOT is $2 \cdot 10^7$ atoms/s at a temperature of $\approx 160\,\mu$K. The atom number in

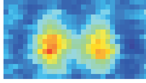

the MOT can be monitored using a photodiode which collects the fluorescence of the trapped atoms. As soon as the MOT contains typically $2 \cdot 10^8$ atoms, the cloud is further cooled to $40 - 50\,\mu$K by means of an optical molasses. At this stage, our atomic sample has a phase space density of $\Omega \approx 3 \cdot 10^{-7}$.

4.3 Magnetic trap

After optically pumping the atoms to the low-field seeking $|F = 2, m_F = 2\rangle$ state, the atoms are loaded into the magnetic trap, which is spatially overlapped with the MOT. The principle of magnetic trapping of atoms is based on the interaction of the permanent magnetic moment μ with an external magnetic field $\mathbf{B}(\mathbf{r})$. The magnetic interaction energy is given by

$$E(\mathbf{r}) = -\mu \cdot \mathbf{B}(\mathbf{r}) = m_F g_F \mu_B \mathbf{B}(\mathbf{r}), \tag{4.1}$$

where g_F is the gyromagnetic factor and m_F is the magnetic sub-level of the atom. Dependent on the sign of $m_F \cdot g_F$, the atoms can be trapped in high ("high field seeker") or low ("low field seeker") magnetic field strength. The Maxwell equations do not allow for a field maximum in regions without current. Therefore only low-field seeking states are magnetically trappable. For the case of the ground state of ^{87}Rb, this restricts the possible states to the magnetic sublevels[1] $|F = 1, m_F = -1\rangle$, $|F = 2, m_F = 1\rangle$, $|F = 2, m_F = 2\rangle$. In our experiment, we choose $|F = 2, m_F = 2\rangle$, since this state has the highest magnetic moment, producing the steepest magnetic potentials for a given magnetic field gradient and thus a spatially small atomic cloud. This allows for an efficient evaporative cooling, since the rate of the necessary collisions for re-thermalization is proportional to the atomic density.

A magnetic field minimum can be experimentally implemented using a pair of coils in anti-Helmholtz configuration, which produces a three dimensional spherical quadrupole magnetic field. Atoms, which are moving in this field adjust their magnetic moment adiabatically to the instantaneous direction of the magnetic field and therefore stay spin polarized and trapped in the corresponding potential, except for the trap center, where the magnetic field vanishes. Here, atoms can undergo Majorana-spinflips [91] to untrapped magnetic sublevels. There are different possible ways to circumvent this problem. The most common types of magnetic traps with a non-zero magnetic field minimum are the Ioffe-Pritchard trap [92], the cloverleaf trap [93] and the time-orbiting potential (TOP) trap [94], which is used in our setup. The TOP trap uses a superimposed homogenous bias field B_0, which is rotating with a frequency of $\omega_{\text{Bias}} = 2\pi \cdot 9.8$kHz in the radial x-y plane. This rotation frequency is chosen much larger than the frequency of the center of mass motion of the atoms in the magnetic potential and much smaller than the larmor frequency. In this case, the superposition of the two magnetic fields yields a time-averaged three-dimensional harmonic potential with typical trapping frequencies $\omega_x = \omega_y = \frac{\omega_z}{\sqrt{8}} = 2\pi \cdot 100\,\text{Hz}$.

The zero magnetic field is no longer in the center of the trap, but moves on a radial circle, the so-called "circle of death" with radius $r_D = B_0/B'$, where B' is the radial field gradient of the quadrupole magnetic field. The circle of death can be used for forced

---

[1] Due to the quadratic Zeeman-shift also $|F = 2, m_F = 0\rangle$ is magnetically trappable.

evaporative cooling. By continuously reducing the bias field B_0 from 32.5 G to 1.5 G and therefore the circle of death from 1.6 mm to 75 μm at a fixed magnetic field gradient $B' \approx 200$ G/cm, we end up with approximately $3 \cdot 10^6$ atoms at a phase-space density of $\Omega \approx 5 \cdot 10^{-3}$. This cloud can now be loaded into the optical crossed dipole beam trap, where the second stage of evaporative cooling to quantum degeneracy is performed.

4.4 Optical dipole potentials

The optical potentials, which are used for the last evaporation stage and the production of the double well potential, are created by focused laser beams with a frequency, which is far detuned from any resonance in the spectrum of ^{87}Rb. This allows for a realization of largely conservative optical traps for neutral atoms.

In the framework of the electric dipole approximation [95], the conservative dipole potential results from interaction of induced atomic dipole moments $\mathbf{d}$ with the oscillating electric field $\mathbf{E}$ of the laser. In the following, I will only consider the case where the detuning $\Delta = \omega_L - \omega_0$ of the laser frequency with respect to the considered line of the rubidium spectrum with frequency ω_0 is much larger than the Rabi frequency $\Omega_R = \mathbf{d} \cdot \mathbf{E}/\hbar$ and the natural line-width Γ of the excited state. In this case, the dipole potential ("ac Stark shift") in a two-level system can be approximated by

$$V(\mathbf{r}) = \frac{\hbar |\Omega(\mathbf{r})|^2}{4\Delta}. \tag{4.2}$$

The square of the Rabi-frequency can be obtained by

$$|\Omega_R(\mathbf{r})|^2 = \frac{\Gamma^2 I(\mathbf{r})}{2 I_{\text{sat}}}, \tag{4.3}$$

where $I(\mathbf{r})$ is the intensity of the laser beam and I_{sat} is the saturation intensity of the considered transition. For atoms with hyperfine structure, we additionally have to take into account the corresponding Clebsch-Gordan coefficients, which are for example listed in [96]. The spontaneous scattering rate, which is determined by the coupling of the atoms to the vacuum modes is given by

$$\Gamma_s(\mathbf{r}) = \frac{\Gamma^3 I(\mathbf{r})}{8 I_{\text{sat}} \Delta^2}. \tag{4.4}$$

It determines the lifetime of the BEC inside the optical trap, since every spontaneous scattering event removes the respective atom from the condensate.

It is important to note, that the potential 4.2 is attractive for red detuned ($\Delta < 0$) and repulsive for blue detuned ($\Delta > 0$) light fields. Therefore, red detuned focused laser beams can be used to realize optical traps for Bose-Einstein condensates.

4.4.1 Crossed optical dipole trap

Our three-dimensional optical trap is realized by two focused far red detuned laser beams, which cross under an angle of nearly 90°. The overlap of the two beams with the magnetic trap is optimized by maximizing the atom number transferred into the optical trap. The laser light for optical trapping is provided by a Nd:YAG laser with a wavelength of

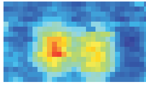

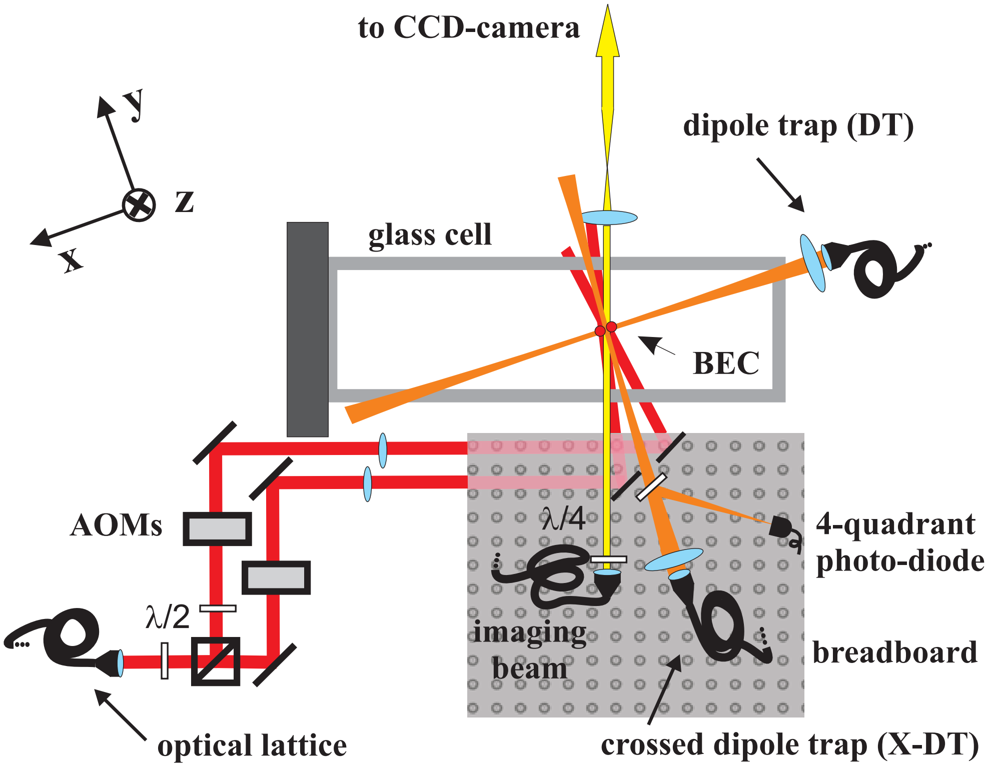

Figure 4.4: Schematic top view of the optical setup around the glass cell. Bose-Einstein condensation is performed in the crossed optical dipole trap consisting of the "dipole trap" (DT) and the "crossed dipole trap"(X-DT). The superposition of the X-DT with an optical lattice of periodicity 5.2 μm creates the effective double well potential. For the sake of clarity, magnetic field coils, MOT-optics and photodiodes for power stabilization of the different beams are not shown.

1064 nm, which is split into two parts (1 W for the dipole trap and 2 W for the crossed dipole trap). The two beams pass individual acousto-optic modulators, which allow to control the optical power and serve as a fast switch. The two AOMs are driven with a frequency difference of 1 MHz in order to prevent interference of the two crossing traps. The first diffraction order of the AOMs is coupled into single mode optical fibers, which guide the light to the experiment. Each of the focused gaussian beams realizes a two-dimensional confinement perpendicular to its propagation axis. For a definition of the x, y and z-direction see figure 4.4. In the following, I will denote the beam propagating in x-direction "dipole trap beam" (DT) and the beam propagating in y-direction "crossed dipole trap beam" (X-DT).

The intensity distribution of a linearly polarized focused gaussian beam of wavelength λ_D propagating in x-direction is

$$I(\mathbf{r}) = \frac{I_{\max}}{1 + (x^2/(x_{Ry}\, x_{Rz}))} \exp\left[-2\left(\frac{y^2}{\sigma_y(x)^2} + \frac{z^2}{\sigma_z(x)^2}\right)\right], \tag{4.5}$$

where $\sigma_{y,z}(x) = \sigma_{0\,y,z}\sqrt{1 + (x/x_{R\,y,z})^2}$. Here, $\sigma_{0y,z}$ is the beam waist in y, z-direction, $x_{R\,y,z} = \frac{\pi\sigma_{0\,y/z}}{\lambda_D}$ is the corresponding Rayleigh length and $I_{\max} = \frac{2P}{\pi\sigma_{0y}\sigma_{0z}}$ is the maximum intensity of the beam with power P.

If the laser has a detuning $\Delta_{1,2}$ with respect to the D1 and D2 line of ^{87}Rb, the optical potential can be approximated by

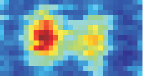

$$V(\mathbf{r}) = \frac{V_{\text{max}}}{1 + (x^2/(x_{R\,y}\,x_{R\,z}))} \exp\left[-2(\frac{y^2}{\sigma_y(x)^2} + \frac{z^2}{\sigma_z(x)^2})\right], \tag{4.6}$$

with the trap depth $V_{\text{max}} = \frac{\hbar\Gamma^2 I_{\text{max}}}{8I_{\text{sat}}}\frac{1}{3}\left(\frac{1}{\Delta_1} + \frac{2}{\Delta_2}\right)$.

For ^{87}Rb the saturation intensity is $I_{\text{sat}} = 1.58\,\text{mW/cm}^2$. The potential in equation 4.6 is the sum of the potentials resulting from the D1 and the D2 line. The factor 1/3 in V_{max} takes into account the Clebsch-Gordan coefficients of the different hyperfine transitions and the factor 2 accounts for the fact, that the D2-line is twice as strong as the D1-line.

If we expand the potential 4.6 quadratically around the focus, we can calculate the trapping frequencies inside a single focused laser beam

$$\omega_y = \sqrt{\frac{4|V_{\text{max}}|}{m\sigma_{0\,y}^2}}, \qquad \omega_z = \sqrt{\frac{4|V_{\text{max}}|}{m\sigma_{0\,z}^2}}, \qquad \omega_x = \sqrt{\frac{2|V_{\text{max}}|}{m x_{R\,y}\,x_{R\,z}}}. \tag{4.7}$$

Note that in the presence of the earth gravitational field, the minimum of the optical potential in z-direction is shifted from the focus about the gravitational sag $\Delta z = g/\omega_z^2$ in the case of a parabolic potential. This effectively reduces all trapping frequencies, since the potential has to be expanded around this new minimum.

The dipole trap beam in our experiment has a radial symmetry and a waist of $60(5)\,\mu$m. It provides the confinement in y and z-direction. Since the Rayleigh length is on the order of 1 cm, the confinement of the DT in x-direction is typically below 1 Hz and therefore negligible. The crossed dipole beam has a waist of $140(5)\,\mu$m in z-direction and $70(5)\,\mu$m in x-direction. It is chosen asymmetrically in order to be able to adjust the harmonic confinement along the x-direction (this will be the direction of the double well potential) more or less independently of the transverse confinement in the y-z plane. The dipole potentials add up in z-direction, which is the direction of gravity. With a maximum power of approximately 500 mW in the dipole trap beam and 800 mW in the crossed dipole trap[2], we can realize a maximum three-dimensional confinement of $\omega_{x,\text{max}} \approx 2\pi \cdot 120\,\text{Hz}$, $\omega_{y,\text{max}} \approx 2\pi \cdot 170\,\text{Hz}$ and $\omega_{z,\text{max}} \approx 2\pi \cdot 180\,\text{Hz}$ and a maximum trap depth of approximately $5\,\mu$K.

All Josephson tunneling experiments have been performed with $\omega_x \approx 2\pi \cdot 78\,\text{Hz}$, $\omega_y \approx 2\pi \cdot 90\,\text{Hz}$ and $\omega_z \approx 2\pi \cdot 66\,\text{Hz}$.

The spontaneous scattering rate per atom

$$\Gamma_s = \frac{\Gamma^3 I_{\text{max}}}{8I_{\text{sat}}}\frac{1}{3}\left(\frac{1}{\Delta_1^2} + \frac{2}{\Delta_2^2}\right). \tag{4.8}$$

at typical optical powers is approximately 0.01 Hz. This means, that we do not expect any influence of spontaneous photon scattering during our Josephson tunneling experiments, which are performed within much less than one second.

The main advantage of the crossed optical dipole trap compared to the magnetic trap is, that we can more or less independently adjust the confinement in the different directions. Another advantage is, that the trap can be switched off within one millisecond

---

[2] The loss of optical power on the way from the laser to the atoms is mainly dominated by the diffraction efficiency of the AOMs, the fiber coupling efficiency (both ≈ 70%) and 10% light reflection of the glass cell.

without introducing kinetic energy to the BEC. In contrast, a sudden turn-off of our magnetic trap always leads to a kick of the BEC which differs from shot to shot. This kick corresponds to a spatial phase gradient on the BEC and would have made the measurement of the relative phase of the two localized modes in the double well trap impossible. Furthermore, the position of our magnetic trap has a shot-to-shot uncertainty on the micrometer scale. As we will see in chapter 5, this uncertainty does not allows for a defined initial preparation of the population imbalance of the two wells. A stable mechanical setup for the optical dipole trap (see section 4.6) allows for a beam stability on the sub-100 nm level, which is required in order to perform the Josephson tunneling experiments.

4.4.2 Realization of an optical double well potential

There are different possibilities to produce a double well potential for Bose-Einstein condensates. The first realized double well potential was obtained by focussing a blue-detuned far off-resonant laser beam into the center of a magnetic trap, generating a repulsive optical dipole potential. This setup with a well-spacing of typically 50 μm was used for the first interference measurements with BECs [10]. Another implementation of a double well potential with a typical spacing of 100 μm in a purely magnetic (time orbiting potential) trap was reported in [37]. Recently, Shin *et al.* [38, 40] have implemented a purely optical double well potential formed by two focused laser beams with a waist of 11.3 μm and a minimum distance of 15 μm.

Without using a Feshbach resonance to suppress the effect of nonlinearity, these implementations are inappropriate for the realization of a Josephson junction for ^{87}Rb Bose-Einstein condensates. In order to be able to observe Josephson tunneling dynamics on a reasonable time scale with at least 1000 condensed atoms, the double well spacing has to be well below 10 μm (see section 3.7).

Atom chips, on which microscopic wires are used to generate magnetic trapping potentials, are predestinated to tailor potentials on a small scale. Double well potentials on atom chips have served as beam splitters for guided atoms already in 2000 [97]. Recently, Estève *et al.* have realized a stable one-dimensional magnetic double well potential with a transverse harmonic confinement on an atom chip [39]. The current status of this experiment is, that a ^{87}Rb Bose-Einstein condensate of approximately $2 \cdot 10^4$ atoms is loaded into a double well trap with a well spacing of 1 μm. The population imbalance can be adjusted by adding an additional bias field on the order of 1 G. However, this setup is very sensitive to fluctuating external magnetic fields on the mG-level and to atom-wire interactions, especially to current distortions inside the wires. This leads to fragmented condensates along the longitudinal potential, which increases the local interaction energy. The authors predict, that despite the noisy electromagnetic field environment, coherent Josephson oscillations should be observable after fixing several technical problems.

To date, coherent Josephson oscillations could not be observed in any of the described experimental setups.

We use a new approach to realize an optical double well potential with a sufficiently small well spacing. This potential is the result of a superposition of the three-dimensional crossed beam dipole trap discussed above with a one-dimensional optical lattice in x-direction. The periodic potential is realized by a pair of laser beams with parallel linear

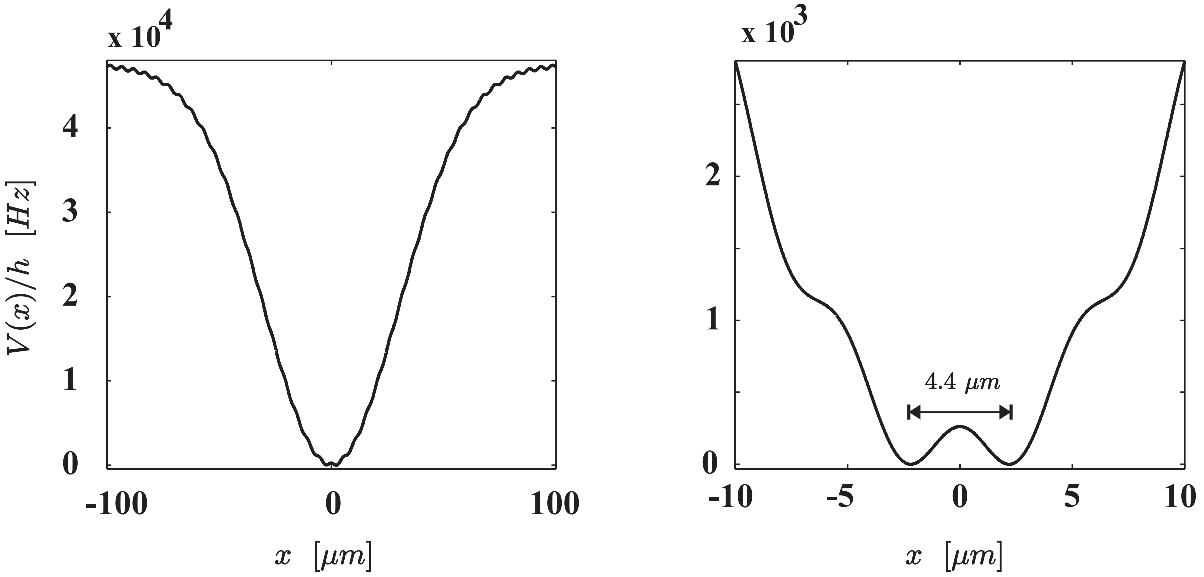

Figure 4.5: Effective double well potential, which is realized as a superposition of the crossed dipole trap with a one dimensional optical lattice (periodicity 5.2 μm). The left hand side shows the complete potential in x-direction. The relevant part of the potential is shown on the right. The Bose-Einstein condensate is loaded into the two central wells, which have a distance of 4.4 μm.

polarization crossing at a relative angle of $\alpha = 9\,°$. The two beams are aligned symmetrically with respect to the crossed dipole trap, such that the resulting potential is modulated in x-direction:

$$V_{SW}(x) = V_0 \cos^2\left(\frac{\pi x}{d}\right) \quad \text{with} \quad d = \frac{\lambda_{\text{sw}}}{2\sin(\frac{\alpha}{2})}. \tag{4.9}$$

The potential depth is given by

$$V_0 = \frac{\hbar\Gamma^2\sqrt{I_1 I_2}}{2I_{\text{sat}}}\frac{1}{3}\left(\frac{1}{\Delta_1} + \frac{2}{\Delta_2}\right) \tag{4.10}$$

where $I_{1,2}$ are the intensities of the two beams and $\Delta_{1,2}$ are their detuning from the D1 and D2 line. Since the laser is red detuned ($\Delta_1, \Delta_2 < 0$), the atoms accumulate in the intensity maxima of the standing light wave.

The laser light for the optical lattice is provided by a Titanium-Sapphire laser, which is operated at a wavelength $\lambda_{sw} = 811\,\text{nm}$. The light is coupled into a single mode optical fiber. The stability of the laser mode can be monitored by means of a Fabry-Perot interferometer. The output of the fibre is split into two parts which pass individual acousto-optic modulators serving to adjust the intensity of the laser beams and the phase of the periodic potential. The AOMs are driven by the two channels of an arbitrary waveform generator (Tektronix AWG 420), whose 10 MHz output signal is mixed with the output of a voltage controlled oscillator operating at 100 MHz. The resulting 110 MHz component is filtered and amplified. The beam waist at the position of the atoms is $\sigma_{sw} = 350(20)\,\mu$m, which is much bigger than the typical extent of the BEC.

Figure 4.5 shows the effective double well potential in x-direction, resulting from the superposition of the X-DT with the optical lattice. Since the spatial extent of the BEC is much smaller than the waist of the crossed dipole beam, it can be approximated by

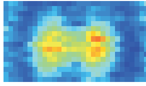

$$V_{\mathrm{dw}} = \frac{1}{2} m \omega_x^2 (x - \Delta x)^2 + V_0 \cos^2\left(\frac{\pi x}{d}\right), \tag{4.11}$$

where Δx is the relative position shift of the two potentials. For $\Delta x = 0$, a symmetric double well potential as shown in figure 4.5 can be created. For the Josephson junction experiments, we use a periodicity $d = 5.2(2)\,\mu\mathrm{m}$ of the optical lattice and a potential depth $V_0 = h \cdot 412(20)\,\mathrm{Hz}$, where the numbers in parenthesis represent the experimental uncertainty in the corresponding parameters.

As we will see in chapter 5, the initial distribution is sensitive to a relative shift on 100 nm-scale. This demands a high passive stability of the crossed dipole beam position and an active stabilization of the phase of the periodic potential.

The combination of the crossed dipole beam trap with a frequency $\omega_x = 2\pi \cdot 78\,\mathrm{Hz}$ and the standing wave results in a well-spacing of $d_{\mathrm{well}} = 4.4\,\mu\mathrm{m}$ and a barrier height $V_b = h \cdot 263(20)\,\mathrm{Hz}$. The main advantage of our double well potential is, that in principle any well spacing can be adjusted by changing the relative angle of the two beams realizing the periodic potential. Additionally this setup allows to adjust the potential barrier independently of the harmonic trapping frequencies, which makes it possible to choose the optimal set of parameters for an experimental observation of nonlinear Josephson junction dynamics at a given total atom number.

4.5 Stabilization of intensity and phase

The intensity of the dipole trap and of the crossed dipole trap are very critical experimental parameters, since intensity fluctuations on the percent level can already parametrically heat the cloud and inhibit Bose-Einstein condensation of small atom numbers. Furthermore, intensity fluctuations of the laser beams realizing the one-dimensional optical lattice result in a fluctuating barrier height during a single experimental sequence and from shot to shot. Therefore, it is important to stabilize all laser beam intensities as good as possible. For this purpose, each beam is locked by an individual control circuit. This consists of a monitor photodiode, which picks up the respective reflection from the glass cell, an AOM and a proportional-integral (PI) loop. The electronic control allows to stabilize the intensity on the photodiode and therefore the intensity inside the glass cell to a nominal value given by the computer by adjusting the input power of the AOM. The resulting relative stability of the beam intensities are better than 10^{-4}. This minimizes shot-to-shot fluctuations of the atom number and allows for a reproducible formation of a BEC consisting of 1000(150) atoms. The condensate lifetime inside the double well potential is typically on the order of 10 s and does not limit the Josephson oscillation measurements, which are performed within approximately 100 ms.

The intensity loop has a time scale of approximately $100\,\mu\mathrm{s}$ and therefore allows for a fast ($< 1\,\mathrm{ms}$) turnoff of the optical potentials. This is especially important for time-of-flight measurements.

Besides the intensity of the laser beams, the relative position of the crossed dipole beam and the standing wave is crucial for the implementation of a bosonic Josephson junction. The relative shift determines whether the resulting effective double well is symmetric or asymmetric. A shift of 350 nm already induces a population imbalance $z = z_c = 0.39$ corresponding to the self-trapping threshold (see chapter 5). This means, that

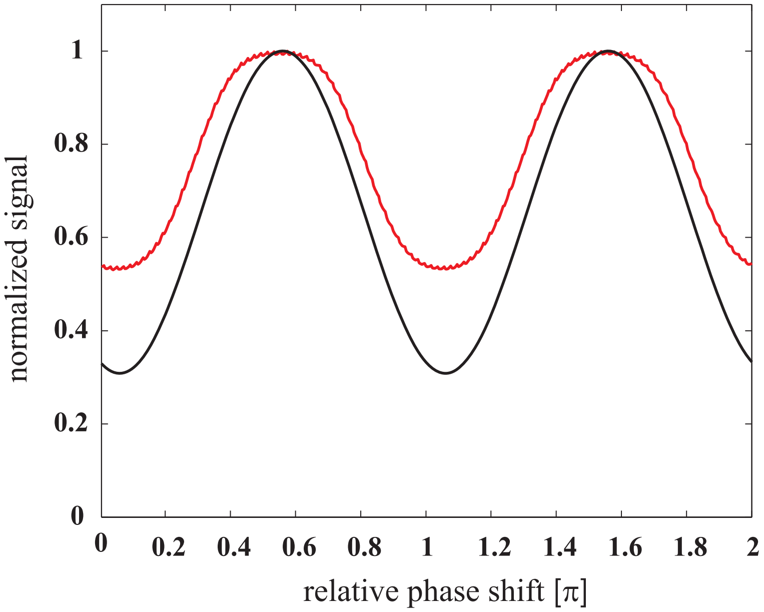

Figure 4.6: Experimentally measured (red line) and theoretically expected (black line) phase lock photodiode signal as a function of the relative phase shift of the two beams. This signal is used to actively lock the relative phase of the one-dimensional optical lattice.

in order to be able to clearly experimentally distinguish the Josephson tunneling regime from the self-trapping regime, a relative position stability below 100 nm is required. In order to stabilize the position of the periodic potential, the relative phase of the two lattice laser beams has to be controlled. For this purpose, two anti-reflection coated glass plates reflect approximately 2% of the intensity of the two beams under a relative angle of 6°. Those two reflected beams interfere outside the vacuum chamber and produce an interference pattern with a periodicity of 8 μm. A precision air slit with a width of 5(1) μm and a length of 3mm (Melles Griot) is placed in the overlap region and is oriented parallel to the interference fringes. The light intensity transmitted through the slit, which is dependent on the relative phase of the two beams, is monitored with a photodiode. The experimental setup for the relevant parts of the phase-lock is shown in figure 4.7. The phase of one beam can be controlled by adjusting the phase of the rf signal driving the corresponding AOM. This is achieved by using four rf phase shifters (Mini-Circuits Jsphs120) connected in series, each with a maximum phase shift of π. The scaled signal of the photodiode as a function of the rf phase is shown in figure 4.6 (red line). The maximum of the signal is on the order of 500 mV for typical experimentally used intensities during the phase lock. The modulation of the signal is nearly 50%. The black line shows the theoretically expected modulation for a lattice of periodicity 8 μm and a slit of 5 μm width. The deviation from the measured signal is most likely due to imperfect alignment of the slit with respect to the direction of the optical lattice. The signal on the photodiode, and therefore the position of the optical lattice can be locked at a given value using a proportional-integral loop which utilizes the phase-shifters to adjust the relative phase of the two beams. We measure the position stability of the periodic potential by fitting the position of the two Bose-Einstein condensates inside the double well potential. From this measurement we obtain a standard deviation of

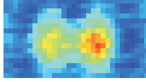

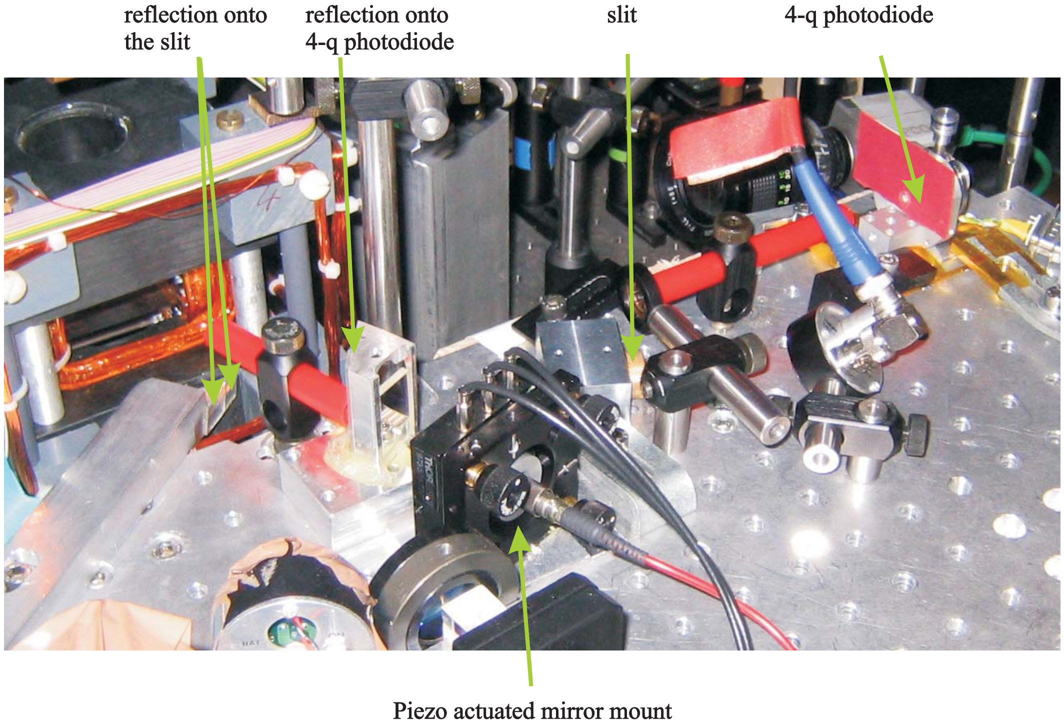

Figure 4.7: Relevant optical parts for the position stabilization of the periodic potential and the crossed dipole trap beam. The position of the optical lattice is controlled by adjusting the relative phase of the two laser beams. The x-position of the X-DT is monitored using a four quadrant photodiode with a spatial resolution of approximately 30 nm

approximately 100 nm, which corresponds to a phase stability of less than $\pi/50$. Since one pixel of our CCD-chip corresponds to approximately 680 nm in real space, the fit error of the position is on the order of the measured position fluctuations. Therefore we believe, that the real position stability of the optical lattice is even better than 100 nm.

One drawback of this implementation of the phase-lock is, that it only works for a constant intensity. However, for loading the Bose-Einstein condensate in the double well potential, the periodic potential has to be adiabatically ramped up to a given value. We therefore lock the phase for two seconds at a very small light intensity, before we ramp to the final potential depth. This intensity is chosen such, that the resulting potential barrier is far below the chemical potential. Therefore the initial adjustment of the phase to the nominal value does not induce collective excitations of the BEC in the crossed dipole trap. A sample and hold integrated circuit is used to fix the input signal of the phase shifters as soon as we start ramping the periodic potential depth to its final value.

The standard deviation of the population imbalance directly after the ramp and after two seconds inside the double well potential is comparably small. Therefore we do not expect that the unlocked phase during the Josephson dynamics affects the tunneling dynamics.

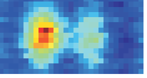

4.6 Mechanical stability and beam position control

The last section described the active position stabilization of the periodic potential. Since the relative position of the standing wave with respect to the crossed dipole trap beam is the relevant experimental parameter, we have to make sure that also the x-position of the X-DT is stable on the same level. This implies a very stable mechanical setup, since the distance of the atoms from the optical table is as large as 22 cm.

In the original setup for the crossed dipole trap individual conventional posts and postholders (from Thorlabs Inc.) for mounting the optical parts have been used. The optical fibre used for the crossed dipole trap beam was assembled by ourselves. In order to control the x-position of the X-DT, a piezo stack was built into the mirror mount carrying the fibre outcoupler. The standard deviation of the x-position of the X-DT using this setup was approximately 800 nm for 30 successive shots. This value is unacceptable for the reproducible adjustment of the initial population imbalance. Therefore we decided to build a breadboard 19 cm above the optical table. This breadboard is fixed on six stable aluminum mounts. A very stable piezo-actuated mirror mount (Thorlabs KC1-PZ), which is directly screwed and glued onto the breadboard is now used to control the position of the X-DT beam. The laser light is focused by a single lens, which is directly glued onto the outcoupler of the new optical fibre (Schäfter + Kirchhoff PMC-1060-P). The optical path has been reduced from 50 cm to 20 cm and now only contains an additional cylindrical lens and an anti-reflection coated glass plate (see figure 4.7). This new setup allows for a standard deviation in the X-DT position below 80 nm. Combined with the position stability of the periodic potential, this is sufficient for the reproducible preparation of a defined initial population imbalance of the two BECs inside the double well potential.

The anti reflection coated glass plate in the optical path of the crossed dipole trap beam reflects a part of the light onto a four-quadrant photodiode (see figure 4.7). This photodiode allows to monitor the position of the beam with a spatial resolution of approximately 30 nm. We have actively stabilized the beam position to the photodiode signal using another PI-loop which acts on the piezo of the piezo actuated mirror mount. However, it turned out that the mechanical setup of the four quadrant photodiode and the glass plate was not more stable than the unlocked position of the X-DT itself. Therefore the active position control did not improve the stability.

In order to initially prepare a given population imbalance, we use a relative shift $\Delta x \neq 0$ of the X-DT with respect to the optical lattice. This shift is experimentally implemented with the piezo actuated mirror mount. After the initial preparation of the BEC, the X-DT beam is shifted back to $\Delta x = 0$, which initiates the Josephson tunneling dynamics. The piezo setup has a response time of 7 ms, which allows to shift the beam non-adiabatically with respect to the Josephson tunneling time scales which are on the order of 50 ms. However, the finite response time has to be taken into account in the numerical integration of the NPSE in order to quantitatively explain our experimental results on Josephson tunneling. The shift could in principle also be done by shifting the phase of the periodic potential. However, this would move the position of the minima of the double well potential, which are basically given by the optical lattice. Therefore, unintentional collective oscillations of the BEC inside the double well potential would be excited.

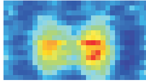

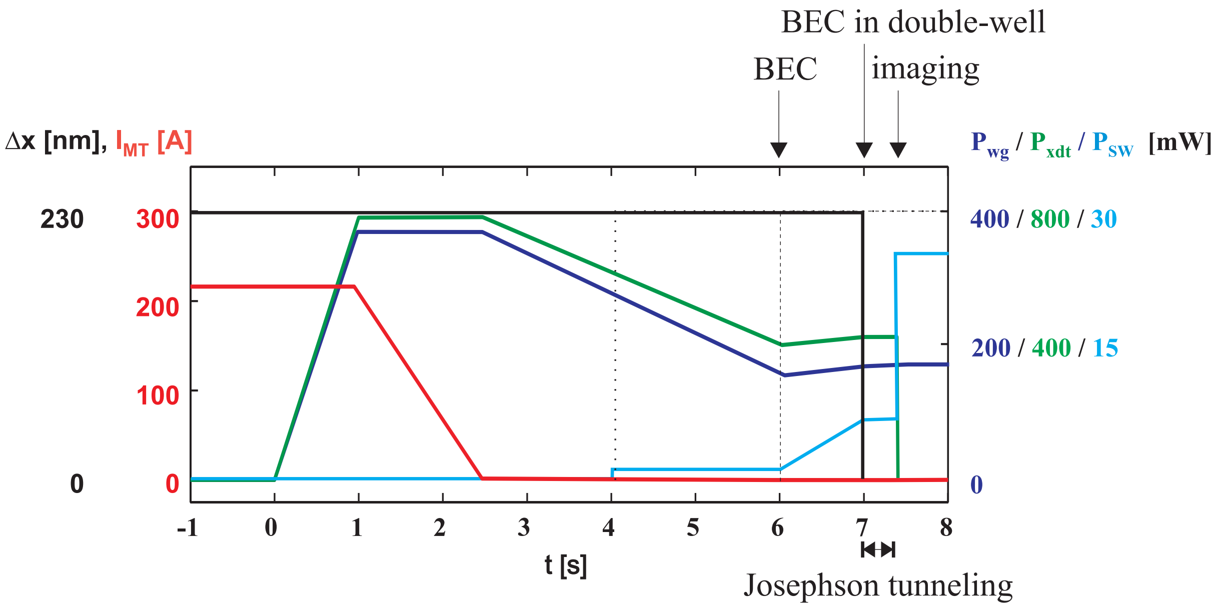

Figure 4.8: Experimental sequence for the observation of Josephson junction dynamics. The BEC is formed inside a crossed optical dipole trap and subsequently loaded into an asymmetric double well potential. After this preparation stage, the potential is shifted to the symmetric double well case, which initiates the Josephson junction dynamics. The sequence ends with the imaging of the wavepacket after a variable propagation time. The black dotted line indicates the activation of the position lock for the periodic potential and the dashed line shows the moment, when the sample-and-hold circuit is activated.

4.7 Experimental sequence

The experimental sequence used for Bose-Einstein condensation of the atomic cloud and preparation in the double well potential is shown in figure 4.8. The figure does not show the MOT-loading process ($\approx 15\,\mathrm{s}$), optical molasses, transfer into the magnetic trap and circle-of-death cooling ($\approx 30\,\mathrm{s}$). At time zero, the transfer from the magnetic trap into the crossed optical dipole trap is initiated by ramping up the intensities of the two laser beams (dark blue and green line). At this stage, the atomic cloud has a phase space density of $\Omega \approx 5 \cdot 10^{-3}$. As soon as the laser beam intensities have reached the maximum value, we ramp down the magnetic quadrupole field indicated by the red line. The whole transfer process takes 2.5 s, which is chosen in order to prevent collective excitations of the atomic cloud. We subsequently perform forced evaporative cooling by lowering the laser beam intensities within 3.5 s. The minimum beam intensities determine the final atom number in the Bose-Einstein condensate. We can reproducibly generate BECs consisting of $5 \cdot 10^4$ down to $1 \cdot 10^3$ atoms in the crossed optical dipole trap. As soon as the desired atom number is reached, the dipole trap beam intensities are again ramped up and at the same time the periodic potential (light blue line) is increased to a given value. This creates two weakly linked BECs inside an asymmetric double well potential with given harmonic trapping frequencies and potential barrier. After the initial preparation, the potential is shifted to the symmetric case by shifting the X-DT position (black line), whereby the Josephson tunneling dynamics are initiated. After a given propagation time, the potential barrier is suddenly ramped up and the X-DT is switched off. This results in dipole oscillations of the atomic clouds around two neighboring minima of the periodic

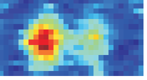

potential. The atomic distribution is imaged at the time of maximum separation using absorption imaging techniques.

The whole sequence from the beginning of the MOT loading to the destructive absorption image of the cloud takes approximately one minute. In order to measure the Josephson dynamics with a sensible statistics and time resolution, a BEC in the double well potential has to be produced several hundred times with reproducible initial population imbalances. This demands for a exceptional long run stability of the system (especially atom numbers, laser beam intensities and positions) and endurance of the experimenters.

Computer control

The experimental sequence is controlled with a time resolution of 1 ms using a programm written in “LabView”. We use 16 analog output channels (-10V to 10V, 1mV RMS noise), 16 digital output channels and 8 analog inputs to control all relevant experimental parameters. A second computer controls the CCD camera taking the absorption images. The first evaluation of the taken images is performed directly after each experimental sequence.

4.8 Imaging setup and optical resolution

The imaging system is crucial for experiments with cold atoms, since all experimental results are extracted from the taken images. We use destructive absorption imaging, which is appropriate for the small atom number $N < 10^4$ used in our experiments. For an overview over non-destructive imaging methods see for example [66].

A collimated gaussian σ^+ polarized laser beam with a waist of 1.9mm, which is resonant with the $F = 2 \rightarrow F' = 3$ transition of the D2-line illuminates the atomic cloud. In order to keep the atoms spin-polarized inside the optical dipole trap, we apply a homogenous magnetic field in the direction of the imaging beam. A part of the laser light is absorbed by the BEC. The shadow of the atoms is approximately 10-fold magnified and imaged onto a CCD camera (Theta-System SiS s285M) by a commercial aspheric lens system (Zeiss Plan-Apochromat S, focal length $f = 10\,\text{cm}$). The CCD-chip consists of 1040×1392 pixels with a pixel size of $6.45\,\mu\text{m} \times 6.45\,\mu\text{m}$ and has a quantum efficiency of approximately 30%. The BEC is heated up and destroyed during the imaging pulse. However, the broadening of the cloud during the exposure time of $4\,\mu\text{s}$ is below one micrometer and therefore negligible. For each realization, we take three images of the transmitted intensity with a time lag of 500 ms: one image I_{pic} of the light in the presence of the atoms, one reference image I_{ref} without atoms and one background image I_{back} without imaging light. The spatial dependent relative intensity is calculated using

$$T(x', z') = \frac{I_{\text{pic}}(x', z') - I_{\text{back}}(x', z')}{I_{\text{ref}}(x', z') - I_{\text{back}}(x', z')}. \tag{4.12}$$

Here, y' denotes the propagation direction of the imaging beam, which encloses an angle of 12.3° with the crossed dipole trap beam (see figure 4.4) and the $x' - z'$-plane is perpendicular to y'. All taken images are projections of the atomic cloud onto the imaging

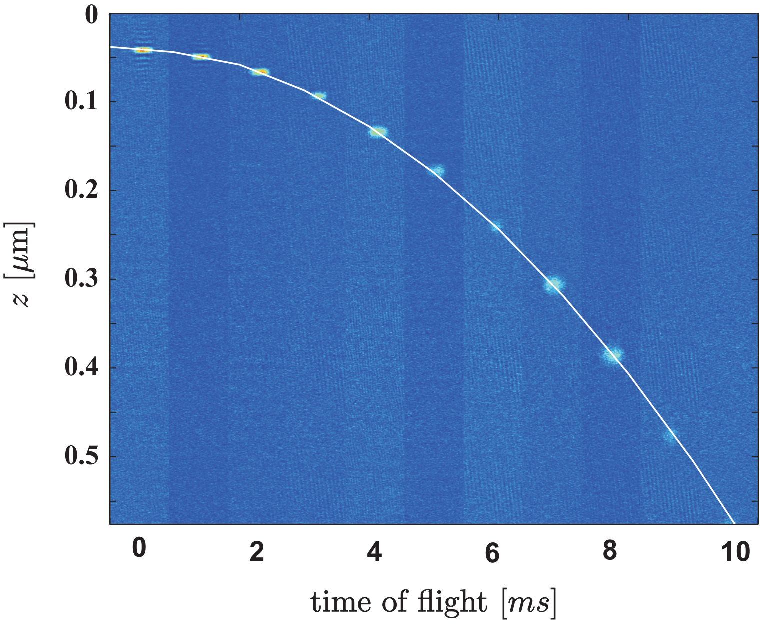

Figure 4.9: Measurement of the magnification of the imaging system. The BEC is released from the optical trap and accelerated in the earth gravitational field. The magnification deduced from a parabolic fit is $M = 9.5(4)$.

plane. Expression 4.12 eliminates the influence of background light and of stationary interference fringes caused by imaging optics. However, time dependent interference fringes, which are caused by oscillations of the glass cell and the imaging lens or time-dependent density fluctuations in the air, limit the quality of the data.

The relative intensity loss inside the atomic cloud is given by

$$\frac{dI(x',y',z')}{I(x',y',z')} = -n(x',y'z')\,\sigma(x',y',z')dy', \tag{4.13}$$

where $n(x',y'z')$ is the atomic density. The scattering cross section $\sigma(x',y',z')$ is dependent on the local light intensity $I(x',y',z')$ [96]. For imaging light which is resonant with the transition of frequency ω_0, one gets

$$\sigma(x',y'z') = \frac{\Gamma\hbar\omega_0}{2I_{\text{sat}}}\,\frac{1}{1+I(x',y',z')/I_{\text{sat}}}. \tag{4.14}$$

Using this expression, the atomic density and the total atom number can be obtained by integrating equation 4.13.

Under the condition $s(x',y',z') \gg 1$, equation 4.13 can be solved analytically. In this case, the atom number which is imaged to a single pixel is given by [74]

$$N_{\text{pixel}}(x',z') = \frac{A}{\sigma M^2}(1-T(x',z')), \tag{4.15}$$

where A is the pixel area, M is the magnification of the imaging system and $\sigma = \sigma(x',y',z')$ is assumed to be constant. In our experiments, the typical saturation is $I/I_{\text{sat}} \approx 10$, such that equation 4.15 underestimates the real atom number by typically less than 10%.

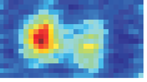

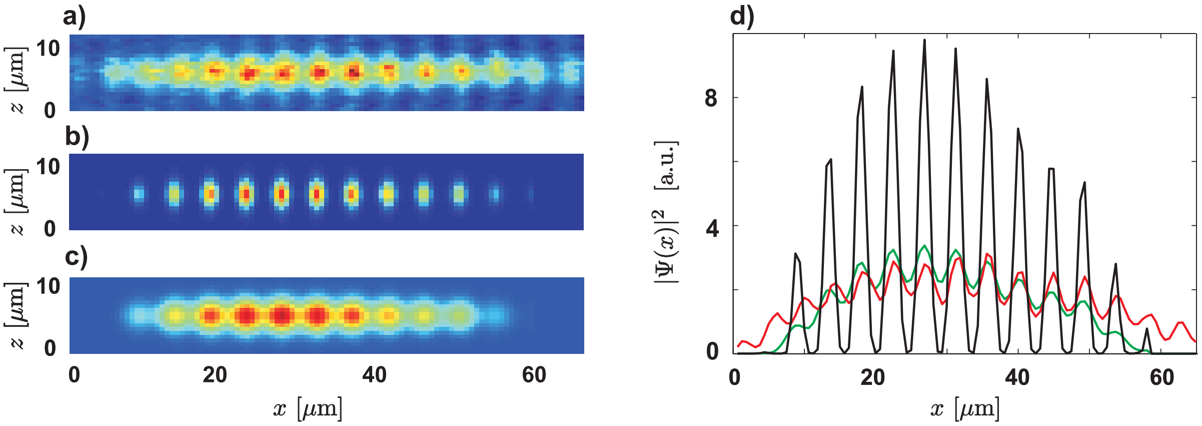

Figure 4.10: Determination of the optical resolution of the imaging system by loading a BEC into a deep optical lattice of period $d = 4.46(5)\,\mu$m. a) Observed density distribution. b) theoretically expected density distribution without including the finite resolution of the imaging system. c) theoretically expected density distribution after convolution with an Airy function of width $\delta_{\text{Rayleigh}} = 4.1(2)\,\mu$m. d) Corresponding density profiles in x-direction (red line: experimental data, black line: theoretically expected density profile, green line: theoretically expected density profile after convolution).

The magnification M of the imaging system is calibrated using a time-of-flight method. For this purpose, a Bose-Einstein condensate is produced inside the crossed optical dipole trap and subsequently the trapping laser beams are switched off. The BEC is accelerated in z-direction due to the earth gravitational field. Figure 4.9 shows absorption images after different time of flights up to 10 ms. By fitting the center of mass trajectory with a parabola, we obtain the magnification $M = 9.5(4)$. Therefore, one pixel on the CCD chip corresponds to 678(30) nm in real space.

Optical resolution of the imaging system

The optical resolution of the imaging system can in principle be calculated using the Abbe formula [98]

$$\delta_{\text{Rayleigh}} = 0.61 \frac{\lambda}{NA} \tag{4.16}$$

which is based on the Rayleigh criterion of resolution[3]. In equation 4.16, NA is the numeric aperture of the imaging lens, which is $NA = 0.218$ in our setup. Therefore, the theoretically expected resolution is $\delta_{\text{Rayleigh}} = 2.18\,\mu$m. Since equation 4.16 does not take into account any abberations, this is a lower bound for the real optical resolution of the imaging setup, which has to be determined experimentally. A detailed investigation of this subject will be presented in the diploma thesis of Jonas Fölling. Therefore, I will only give a summary of the obtained results.

A BEC consisting of $1.8 \cdot 10^4$ atoms is loaded into a deep one-dimensional optical lattice with a potential depth $V_0 = h \cdot 1740(50)$ Hz and a lattice spacing $d = 4.46(5)\,\mu$m superimposed on a harmonic confinement with trapping frequencies $\omega_x = 2\pi\cdot\, 13.5(5)$ Hz

---

[3] The optical resolution according to the Rayleigh criterion corresponds to the position of the first zero of the Airy-function.

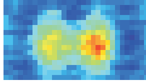

and $\omega_y \approx \omega_z = 2\pi\cdot 116(5)\,\mathrm{Hz}$. Figure 4.10a shows an absorption image of the experimentally observed atomic density distribution. The asymmetry of the density distribution in x-direction is due to a tilt $\alpha = 0.63°$ of the dipole trap with respect to the plane perpendicular to the direction of gravity, which results in a weak distortion of the gaussian potential profile. The density distribution can be compared to the distribution expected from the numerical solution of the NPSE for the corresponding trapping parameters, which has to take into account the enclosed angle of 12.3° between the imaging plane and the plane perpendicular to the optical lattice. The theoretically expected atomic distribution is shown in Figure 4.10b. It is much more modulated than the experimental data, since it does not include the effect of a finite resolution of the imaging system. The optical resolution is obtained by convolving this theoretically obtained distribution with an Airy function of variable size and comparing the result to the measured atomic distribution. The best agreement is obtained using an optical resolution of $\delta_{\mathrm{Rayleigh}} = 4.1(2)\,\mu\mathrm{m}$. The corresponding convolved theoretical atomic distribution is shown in figure 4.10c.

Figure 4.10d shows density profiles in x-direction, which are obtained by averaging over the three central rows of the two-dimensional distributions. The experimental data is represented with the red line and shows good agreement with the numerically calculated profile (green line), which has been convolved with an airy function of width $\delta_{\mathrm{Rayleigh}} = 4.1(2)\,\mu\mathrm{m}$. The black line represents the density profile corresponding to the numerical solution without taking into account the finite resolution.

The Rayleigh criterion of resolution is rather pessimistic, since the sum of the Airy functions of two point sources located at a distance $\delta_{\mathrm{Rayleigh}}$ still shows a clear minimum with a modulation of approximately 26%. If the two point sources are further approached, this minimum vanishes at a certain distance $\delta_{\mathrm{Sparrow}}$. The resolution criterion based on this condition is known as the Sparrow-criterion. It represents the far more appropriate resolution criterion for modern detection devices [99]. The Sparrow resolution is given by

$$\delta_{\mathrm{Sparrow}} = 0.47\frac{\lambda}{NA}. \tag{4.17}$$

From our experimental data, we obtain $\delta_{\mathrm{Sparrow}} = 3.2(2)$. The resolution expected from equation 4.17 is approximately 45% smaller than the experimentally obtained value. This deviation has several reasons:

- The optical resolution of the experimental imaging setup is not only limited by diffraction, but also by abberations of the imaging lens.
- The atomic clouds have a waist of approximately $5\,\mu\mathrm{m}$ in z-direction, which has to be compared to the Rayleigh depth of sharpness $\Delta z_R = \frac{\lambda}{NA^2} \approx 8\,\mu\mathrm{m}$. Therefore, the parts of the cloud, which are not in the central focal plane are effectively broadened by the imaging system.
- The resonant imaging light heats up the atomic clouds and leads to an expansion particularly in imaging direction [74]. This expansion is given by $\Delta z_h = 1/4 v_R \Gamma t^2 \approx 800\,\mathrm{nm}$, where $v_R = 5.7\frac{\mathrm{mm}}{\mathrm{s}}$ is the recoil velocity of a ^{87}Rb atom emitting a photon on the D2 transition and $t = 4\,\mu\mathrm{s}$ is the imaging time. The broadening in the x'-y' plane is given by $\Delta z_\perp = \sqrt{\frac{\Gamma}{3}} v_R t^{3/2} \approx 160\,\mathrm{nm}$. This effect additionally broadens the imaged atomic distribution.

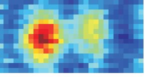

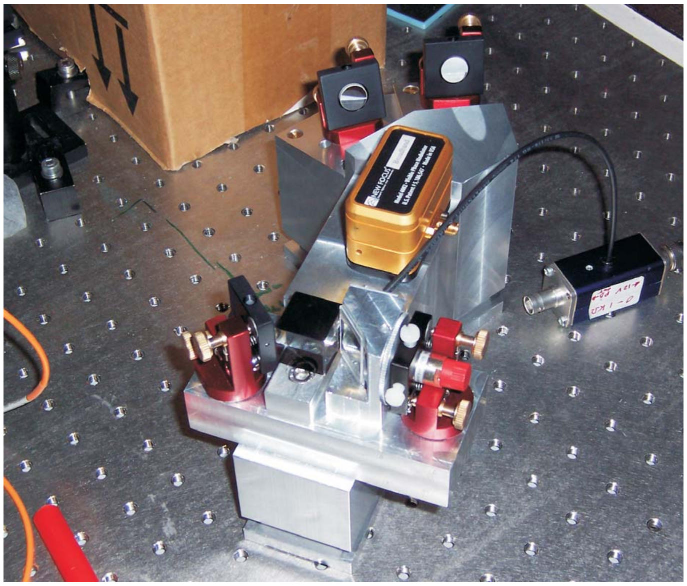

Figure 4.11: Improved experimental setup for the standing light wave. All optical parts are mounted onto a massive aluminum body. The relative phase of the laser beams is adjusted using a single electro-optic modulator.

Therefore the value for the optical resolution above is only an upper bound for the real resolution of the imaging setup.

Another way to determine the resolution is to produce a BEC consisting of ≈ 6000 atoms in the crossed dipole trap with frequencies $\omega_x = 2\pi \cdot 25(2)\,\mathrm{Hz}$ and $\omega_y \approx \omega_z = 116(5)\,\mathrm{Hz}$. The experimentally measured $1/e^2$ width of the wavepacket is $\sigma_z = 2.9(2)\,\mu\mathrm{m}$. From a numerical calculation of the corresponding ground state, one obtains a $1/e^2$ width of $1.7\,\mu\mathrm{m}$. A deconvolution of the measured profile yields an optical resolution $\delta_{\mathrm{Sparrow}} = 2.7(2)$. This will be referred to as optical resolution of the imaging setup in the following sections.

4.9 New experimental setup for the optical lattice

As already discussed above, the depth and the position of the potential barrier are crucial experimental parameters. The lock of the relative phase of the two beams allows for a sufficient short term and long run stability of the lattice position. In the setup described above, we use two independent optical paths of approximately one meter and two AOMs to control the intensity and phase of the individual beams. It turned out, that this setup shows a long term drift of the position of the individual beams and therefore of the barrier height. This made a daily calibration of the potential depth necessary. Therefore we have decided to build a new stable setup for the optical lattice after we have finished the Josephson junction measurements presented in chapter 5. This new setup is shown in figure 4.11. All optical parts are mounted onto a single massive aluminum body. The beam intensities are now controlled using a single AOM in front of the optical fibre. After the fibre outcoupler, the laser beam is split into two parts using a non-polarizing beam splitter, which supersedes the use of additional waveplates. The relative phase of the two beams and therefore the position of the lattice is controlled by a single electro-

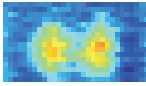

optic modulator which is placed into one of the two beams. The optical paths could be reduced to 30 cm. We use the fibre outcoupler to adjust the beam waist inside the glass cell to approximately 500 μm without using any additional focussing lenses.

This new setup allows us to run the experiment for several days without re-calibration of the optical potentials.

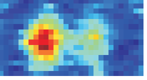

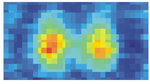

5 Experimental results

In this chapter the experimental results on Josephson junction dynamics of a Bose-Einstein condensate in a double well potential are presented. These results have been published in Physical Review Letters [100].

5.1 Calibration of the double well potential

The characterization of the double well potential is crucial for the investigation of Josephson dynamics of two coupled Bose-Einstein condensates. In order to adjust the atom number such, that we are able to observe both dynamical regimes - Josephson oscillations and macroscopic quantum self-trapping - all optical potentials have to be calibrated with a precision of a few percent. The calibration of the double well potential is done in three steps. We independently measure the trapping frequencies of the three-dimensional harmonic confinement, the lattice spacing and the potential depth of the one-dimensional optical lattice.

5.1.1 Harmonic confinement

The calibration of the harmonic trapping frequencies in x- and z-direction is performed by exciting collective dipolar oscillations and deducing the center of mass position as a function of the evolution time from the taken absorption images. The dipolar oscillation in z-direction (direction of the earth gravitational field) is excited by reducing the power of one of the dipole trap beams for one millisecond. After readjusting the initial power, the BEC starts to oscillate with an amplitude of a few micrometers. The oscillation in x-direction is simultaneously excited by shifting the crossed dipole trap beam using the piezo actuated mirror. Figure 5.1 shows the experimental data (red crosses) and a damped sinusoidal fit (black line) for the parameters we use in the Josephson junction experiments. The measurement yields harmonic trapping frequencies $\omega_x = 2\pi \cdot 79(2)\,\mathrm{Hz}$ and $\omega_z = 2\pi \cdot 66.0(2)\,\mathrm{Hz}$.

Since we can not directly observe oscillations in y-direction with our imaging setup, we have to calibrate the third frequency indirectly. The contribution of the X-DT to this frequency is negligible, since the longitudinal trapping frequency is below 1 Hz for all used beam intensities. We measure the trapping frequency in z-direction and the corresponding equilibrium position for four different intensities of the dipole trap beam. During this measurement, the crossed dipole trap beam is operated at a very small power and does not contribute to the measured frequencies. The potential in z-direction is therefore solely given by the dipole trap beam and the earth gravitational potential

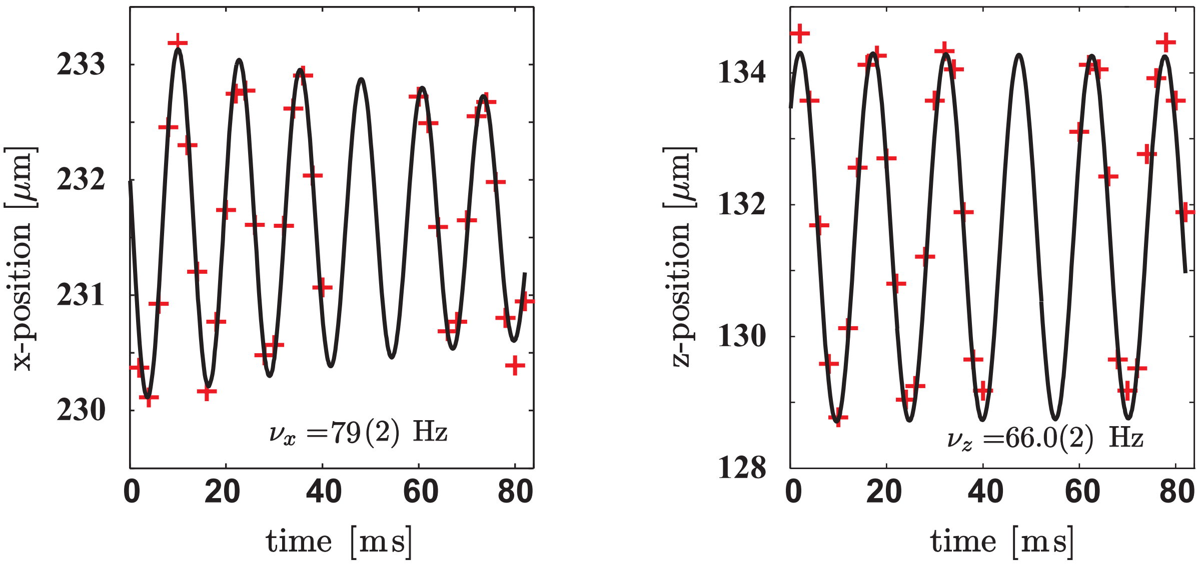

Figure 5.1: Calibration of the harmonic confinement in x- and z-direction. A dipolar oscillation in both directions is simultaneously excited and the center of mass motion of the BEC around the equilibrium position of the optical dipole trap is deduced from absorption images (red crosses). The damped sinusoidal fit to the data (black line) yields the corresponding trapping frequencies $\omega_x = 2\pi \cdot 78.8(2)\,\text{Hz}$ and $\omega_z = 2\pi \cdot 66.0(2)\,\text{Hz}$.

$$V(z) = V_{\text{max,DT}}\, e^{-2(z-z_0)^2/\sigma_{DT}^2} - mgz \tag{5.1}$$

By harmonically expanding equation 5.1 around the respective minimum and comparing the results to the measured frequencies and equilibrium positions, we can deduce the waist σ_{DT} of the DT, the position z_0 of the dipole trap beam and the absolute values of $V_{\text{max,DT}}$ for the four different adjusted relative beam intensities.

The knowledge of these parameters allows for a calculation of the trapping frequency in y-direction as follows. The z-position z_{cloud} of the BEC for the trapping parameters we are interested in can be deduced from the measurement shown in figure 5.1. Using this value, the gravitational sag $\Delta z = z_{\text{cloud}} - z_0$, which is the displacement from the intensity maximum z_0 of the beam can be calculated. The potential in y-direction has a gaussian shape even in the presence of the earth gravitational field acting in z-direction. Under the assumption of a radially symmetric dipole trap beam, the corresponding trapping frequency is given by (see equation 4.7)

$$\omega_y = \sqrt{\frac{4|V_{\text{max,DT}}|e^{-2(z_{\text{cloud}}-z_0)^2/\sigma_{DT}^2}}{m\sigma_{DT}^2}} = 2\pi \cdot 91(2)\,\text{Hz} \tag{5.2}$$

where $V_{\text{max,DT}}$ is the potential at the intensity of the dipole trap beam used for the measurement in figure 5.1.

5.1.2 Lattice spacing

The lattice spacing of the periodic potential can in principle be obtained by measuring the relative angle of the two lattice laser beams. However, due to the restricted access to the

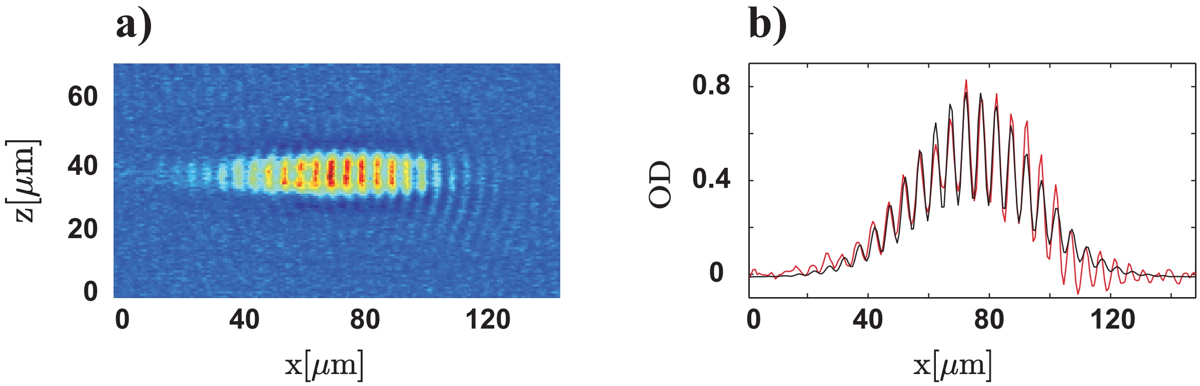

Figure 5.2: Calibration of the lattice spacing of the periodic potential. A Bose-Einstein condensate consisting of $2.8 \cdot 10^4$ atoms is loaded into a deep optical lattice. a) Absorption image of the atomic cloud b) Density profile in x-direction (red line). The distance of the density maxima corresponds to the lattice spacing $d = 5.18(9)\,\mu$m, which is obtained by fitting the density profile with a sinusoidally modulated gaussian (black line).

beams passing below the breadboard, the angle $\alpha = 9(1)^\circ$ can only be determined with an accuracy of approximately 10%. This limits the knowledge of the lattice spacing to $d = 5.17(46)\,\mu$m, which is not accurate enough for the quantitative comparison between numerical simulations and the Josephson junction experiment.

Therefore a direct measurement of the lattice spacing has to be performed. For this purpose, a BEC consisting of $2 \cdot 10^4$ atoms is loaded into a deep optical lattice ($V_0 \approx h \cdot 2000\,$Hz) superimposed on a harmonic trap of trapping frequencies $\omega_{x,y,z} = 2\pi \cdot (5, 120, 140)\,$Hz. For those parameters, the influence of the shallow harmonic potential in x-direction on the spacing of the potential minima is negligible. Therefore, the spacing of the maxima of the atomic density directly corresponds to the lattice spacing d. The resulting atomic distribution is shown in figure 5.2, where several potential wells are occupied. The density profile in x-direction (red line in figure 5.2) is fitted with a sinusoidally modulated gaussian (back line) and the spacing of the atomic density maxima is extracted. By taking the mean value over five realizations, the projection of the spacing onto the imaging plane can be determined to $d_{\text{imag}} = 5.06(9)\,\mu$m. Since the direction of the optical lattice encloses an angle of 12.3° with the imaging plane, the obtained value has to be corrected to $d = d_{\text{imag}}/\cos(12.3^\circ) = 5.18(9)\,\mu$m, which is in agreement with the estimation given above.

5.1.3 Potential depth

The potential depth of the periodic potential is calibrated by measuring the relative motion of the two BECs in the double well potential. A dipolar oscillation inside the respective wells is excited by non-adiabatically increasing the well spacing. This is achieved by loading the BEC into the effective double well potential (black line in figure 5.3a) and subsequently switching off the crossed dipole beam and increasing the potential depth by a factor of 4.9 within 2 ms. At the beginning, the double well spacing $d_{\text{well}} = 4.2\,\mu$m is determined by both, the lattice spacing $d = 5.18\,\mu$m of the optical lattice and the strength of the harmonic confinement in x-direction. By switching off the crossed dipole beam, we change the double well potential to a purely sinusoidal optical lattice with pe-

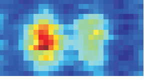

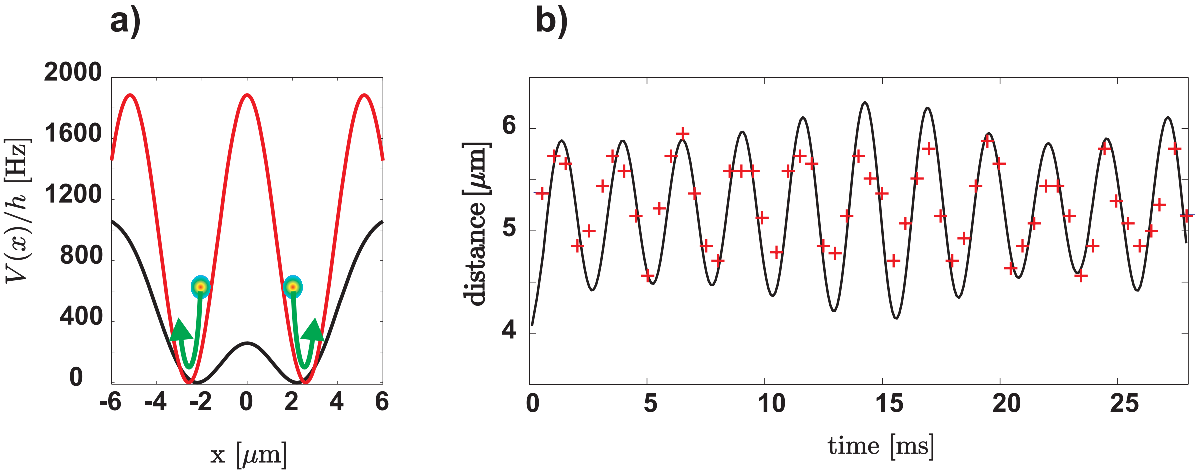

Figure 5.3: Calibration of the periodic potential depth. a) The BEC is first loaded into the effective double well potential (black line). We subsequently switch off the harmonic confinement in x-direction and increase the depth of the optical lattice. This increases the distance between the two wells and causes an oscillation of the two BECs in the individual wells. b) Relative position of the the two BECs in the optical lattice as a function of time after exciting the dipolar oscillation inside the wells. The experimental data (red crosses) is compared to the numerical simulation (black line), which has only the lattice depth as a free parameter.

riodicity $d = 5.18\,\mu$m (red line in figure 5.3a). Therefore the two BECs start oscillating around the new potential minima. The final potential depth of the periodic potential is chosen such, that no tunneling can occur during the oscillation. It turned out that an instantaneous change from the double well to the purely periodic potential also excites collective excitations in the transverse direction, which couples to the x-direction via the nonlinear interaction term in the Gross-Pitaevskii equation. Therefore we have chosen a ramp time of 2 ms, which strongly reduces these excitations, but also reduces the expected oscillation amplitude inside the single wells to approximately 400 nm.

Figure 5.3b shows the distance between the two BECs as a function of time after exciting the dipolar oscillation in the individual wells (red crosses). The black line is the result of a numerical simulation of this measurement using the nonlinear non-polynomial Schrödinger equation. The only free parameter in the simulation is the initial potential depth $V_{0,\mathrm{initial}}$ of the periodic potential, since the trapping frequencies of the harmonic confinement have already been calibrated. By calculating the numerical solution for different $V_{0,\mathrm{initial}}$ and comparing the results to the experimentally obtained oscillation, we get a potential depth $V_{0,\mathrm{initial}} = h \cdot 412(20)\,\mathrm{Hz}$. This potential depth corresponds to a barrier height $V_b = h \cdot 263(20)\,\mathrm{Hz}$ for the experimentally used harmonic confinement $\omega_x = 2\pi \cdot 78\,\mathrm{Hz}$.

5.2 Determination of dynamical variables

The macroscopic tunneling dynamics of a Bose-Einstein condensate in a double well potential is governed by the time evolution of the two dynamical variables, the fractional population imbalance and the relative phase between the left and right component. Their experimental determination is discussed in this section.

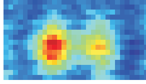

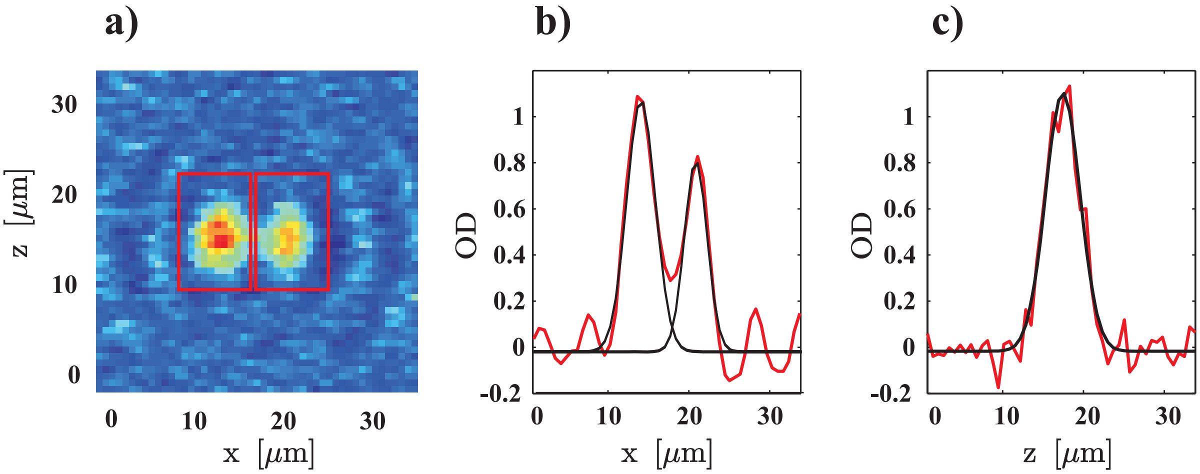

Figure 5.4: Determination of the fractional population imbalance. a) Absorption image of the BEC in the double well potential after increasing the well spacing (see text). The fringes around the atomic cloud result from the fact, that the size of the individual BECs in x-direction is approximately a factor of two smaller than the optical resolution. b) The density profile in x-direction (red line) can be well approximated by a sum of to gaussian functions (black lines). b) The profile in z-direction is fitted using a gaussian function.

5.2.1 Fractional population imbalance

The population imbalance is obtained from the absorption images taken after a given propagation time of the BEC inside the double well potential. In order to be able to clearly resolve the two localized modes, we increase the distance between the two BECs before imaging the atomic distribution. This is done by exciting a dipolar oscillation of the BECs in the individual wells as described in section 5.1.3. Since the lattice depth is increased by a factor of 4.9, no further Josephson tunneling takes place, so that the population imbalance is “frozen” during this process. The absorption image of the atomic cloud is taken at the time of maximum separation $\Delta t = 1.5\,\mathrm{ms}$. At this time, the two wave-packets have a distance of approximately $5.5\,\mu\mathrm{m}$ and can therefore be resolved by our imaging system. A typical absorption image of a BEC consisting of 1200(100) atoms in the double well potential is shown in figure 5.4a. By fitting the profile of the optical density in x-direction (red line in figure 5.4b) with a sum of two gaussian functions and in z-direction (figure 5.4c) with a gaussian function, we obtain the atom numbers in the individual wells and the fractional population imbalance

$$z = \frac{N_1 - N_2}{N_T} = 0.23(3). \tag{5.3}$$

An alternative way to determine the atom number in each well without applying a fit routine is to sum over the pixels in the respective regions (red rectangles in figure 5.4a). From this approach we get $z_{\text{count}} = 0.25(4)$, which is consistent with the value obtained from the fit.

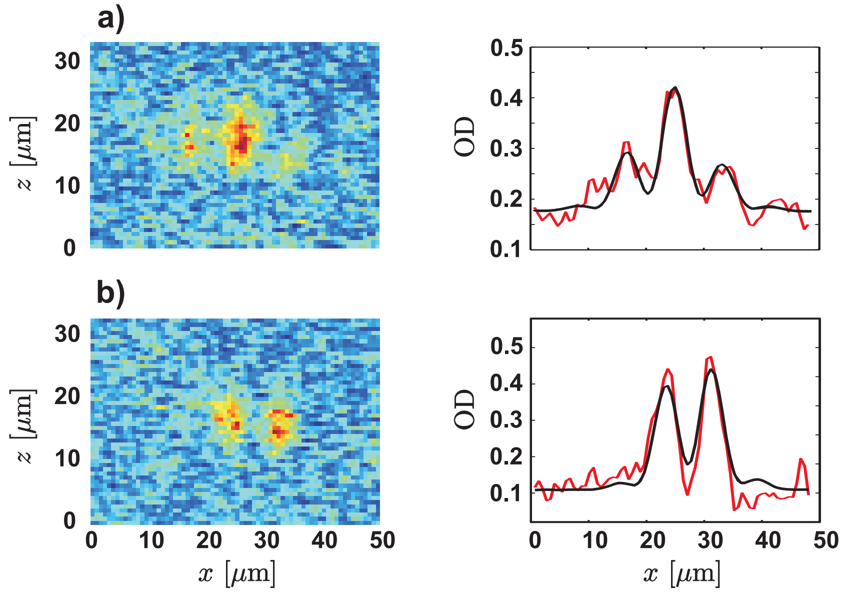

Figure 5.5: Determination of the relative phase of the two localized modes. The figures on the left hand side show absorption images of the atomic interference pattern after a time of flight of 8 ms after switching off the trapping potentials. From the fit (black line) to the density profile in x-direction (red line) we obtain a) $\phi = 0.1(1)\pi$ and b) $\phi = -0.9(1)\pi$.

5.2.2 Relative phase

In order to measure the relative phase of the localized modes, the wavepackets are released from the double well potential by suddenly switching off the confining laser beams. The two BECs are accelerated in the earth gravitational field and expand due to their dispersion. After a certain time-of-flight, the two clouds overlap and form a double slit interference pattern [10]. The phase of the atomic interference pattern is directly connected to the relative phase of the two BECs. In order to extract the relative phase, we assume, that the density distribution in x-direction of the BEC inside the double well potential can be approximated by the sum of two gaussians with independent amplitudes[1]

$$\Psi(x) = A_1 e^{-\frac{(x-x_1)^2}{\sigma^2}} + A_2 e^{-\frac{(x-x_2)^2}{\sigma^2}}. \tag{5.4}$$

The corresponding interference pattern, which is formed in the far field after releasing the cloud from the trapping potentials can be obtained by Fourier transformation of equation 5.4, which is given by

$$|\Psi(k)|^2 = e^{-2((k-k_0)/\sigma_k)^2} \left[A_1^2 + A_2^2 + 2A_1A_2 \cos\left(\frac{2\pi}{d_{TOF}}(k-k_0) - \phi \right) \right], \tag{5.5}$$

where k_0 is the center and σ_k the waist of the gaussian envelope in momentum space, ϕ the relative phase of the two localized modes and d_{TOF} the periodicity of the interference fringes.

---

[1] The width of the two gaussians is assumed to be equal since the difference of the two widths is below 10%, even at a population imbalance $z = 0.6$.

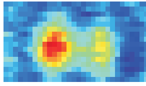

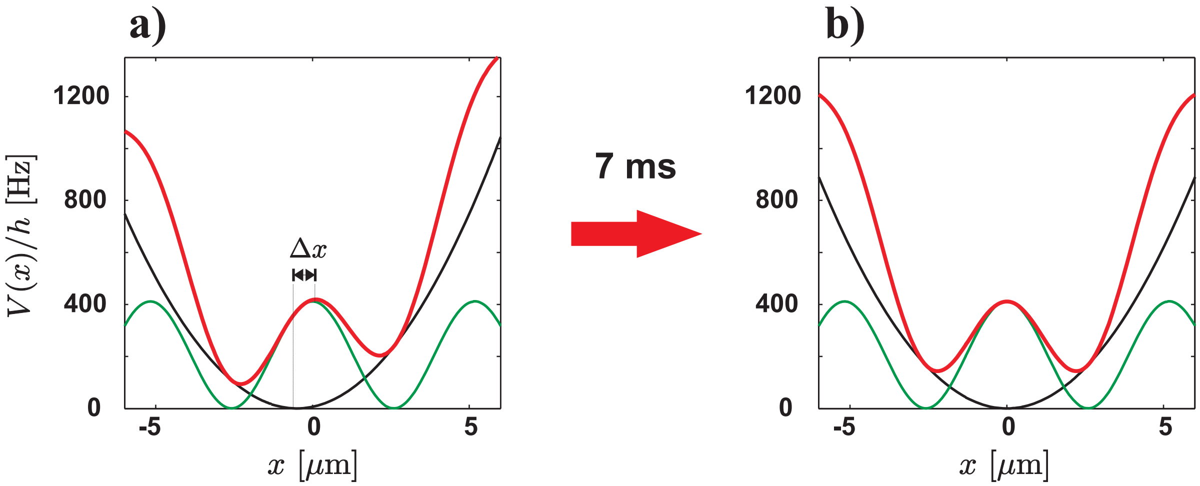

Figure 5.6: The initial population imbalance $z(0) \neq 0$ is prepared by adiabatically loading the BEC into the ground state of an asymmetric double well potential ($\Delta x \neq 0$) shown in the left figure. The potential is subsequently shifted to the symmetric case within 7 ms in order to initiate the macroscopic tunneling dynamics.

Figure 5.5 shows two typical absorption images of atomic interference patterns formed after 8 ms time-of-flight. The density profiles along the x-direction are fitted using equation 5.5. We extract a relative phase of $\phi = 0.1(1)\,\pi$ for the image in figure 5.5a and $\phi = -0.9(1)\,\pi$ for figure 5.5b.

The evaluation of the experimentally observed interference pattern using equation 5.5 requires a long time of flight ensuring that the measurement is performed in the far field. However, the optical density of the atomic cloud drops quickly after releasing a BEC containing approximately 1000 atoms from the trap, which makes an imaging with a reasonable signal to noise ratio impossible for time of flights longer than typically 8 ms. Numerical simulations have shown, that the far field is reached after a time of flight of 5 ms in the Josephson oscillation regime and 8 ms in the self-trapping regime[2].

5.3 Preparation of the initial population imbalance

In order to observe Josephson dynamics of a Bose-Einstein condensate inside a symmetric double well potential, we prepare an initial population imbalance $z(0) \neq 0$. This is experimentally implemented by adiabatically loading the BEC into the ground state[3] of an asymmetric double well potential as shown in figure 5.6a. The asymmetry of the potential and therefore the population imbalance of the corresponding ground state can be controlled by adjusting the relative position shift Δx of the crossed dipole trap beam realizing the harmonic confinement in x-direction with respect to the optical lattice. The potential is subsequently shifted to the symmetric double well configuration (figure 5.6b within 7 ms using the piezo actuated mirror which has been calibrated by measuring

---

[2] For those time of flights, the systematic errors of the phases obtained by applying equation 5.5 are less than 0.1π.

[3] It is important to note, that the preparation in the ground state of the shifted potential implies a zero initial relative phase of the two localized modes independently of the asymmetry of the double well potential.

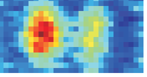

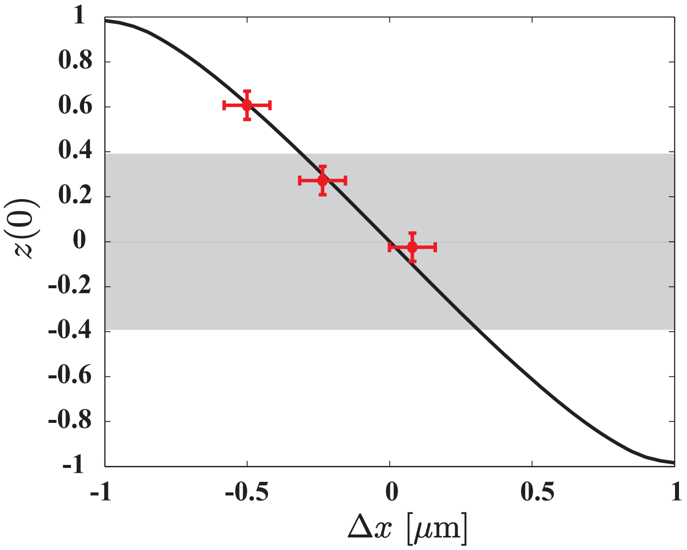

Figure 5.7: Theoretically expected ground state population imbalance (black line) as a function of the relative shift Δx of the harmonic confinement with respect to the optical lattice. The filled red circles show the measured population imbalances. The transition is expected to occur at a relative shift $\Delta x = 350\,\text{nm}$.

the x-position of the BEC in the harmonic trap as a function of the piezo voltage. This initiates the macroscopic tunneling dynamics which will be presented in the next section.

Figure 5.7 shows the calculated ground state population imbalance as a function of the relative shift Δx (black line) obtained by an imaginary time propagation of the nonlinear nonpolynomial Schrödinger equation using the calibrated potential parameters. The red points are the measured population imbalances. The error bars represent statistic and systematic errors[4]. Josephson oscillations are expected in the gray shaded region. The theoretically predicted transition to the self-trapping regime occurs at $z_c = 0.38$ corresponding to a relative position shift of $\Delta x = 350\,\text{nm}$. The mechanical stability of our setup allows for a reproducible adjustment of any initial population imbalance with a standard deviation of $\Delta z(0) = 0.06$. This enables a preparation of the initial population imbalance corresponding to the Josephson oscillation regime as well as to the self-trapping regime.

5.4 Observation of Josephson oscillations and self-trapping

In this chapter, the first experimental observation of a Josephson tunneling between two Bose-Einstein condensates is presented.

After the preparation of a given initial population imbalance and the subsequent shift to the symmetric double well case, the tunneling massive particles are directly imaged using absorption imaging. Figure 5.8 shows the taken images ($17.5\,\mu\text{m} \times 9.8\,\mu\text{m}$) of the Bose-Einstein condensate after a variable evolution time in the symmetric double well potential. Before taking the images, the potential barrier is suddenly ramped up and the harmonic confinement in x-direction is switched off. This results in dipole

---

[4] The errors are dominated by fit errors of the lattice position and the population imbalance.

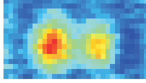

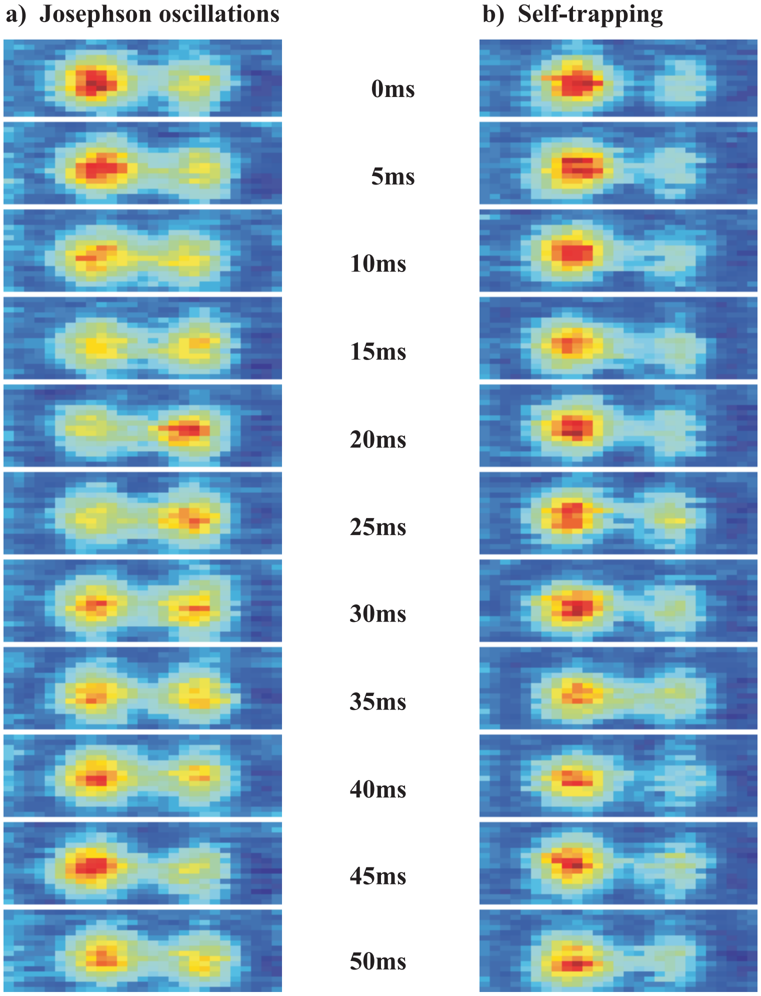

Figure 5.8: Observation of macroscopic tunneling dynamics between two weakly linked BECs in a symmetric double well potential. Shown are absorption images of the atomic cloud after a variable evolution time. a) Josephson oscillations are observed, if the initial population imbalance $z(0) = 0.28(6)$ is below the critical value $z_c = 0.38$. b) In the self-trapping regime with $z(0) = 0.62(6)$, the population inside the individual wells is stationary within the experimental errors.

oscillations of the atomic clouds in the individual wells. The images are taken at the time (1.5 ms) of maximum separation (5.5 μm) of the two BECs. Each image corresponds to a new experimental realization. The experimental data are post-selected retaining only realizations of atom numbers between 1000 and 1300 atoms[5]. This is necessary in order to obtain comparable overlaps of the two localized modes and therefore comparable tunneling times in different realizations.

Figure 5.8a shows macroscopic tunneling dynamics in the Josephson oscillation regime. The initial population imbalance is adjusted to $z(0) = 0.28(6)$, which is implemented using a relative position shift $\Delta x = 240(80)$ nm of the harmonic confinement in x-direction with respect to the optical lattice. The time evolution of the population of the left and right well is directly visible in the absorption images. The atoms tunnel to the right and left over time. The population imbalance is inverted after approximately 20 ms and

---

[5] approximately 70% of all experimental realizations fulfill this condition.

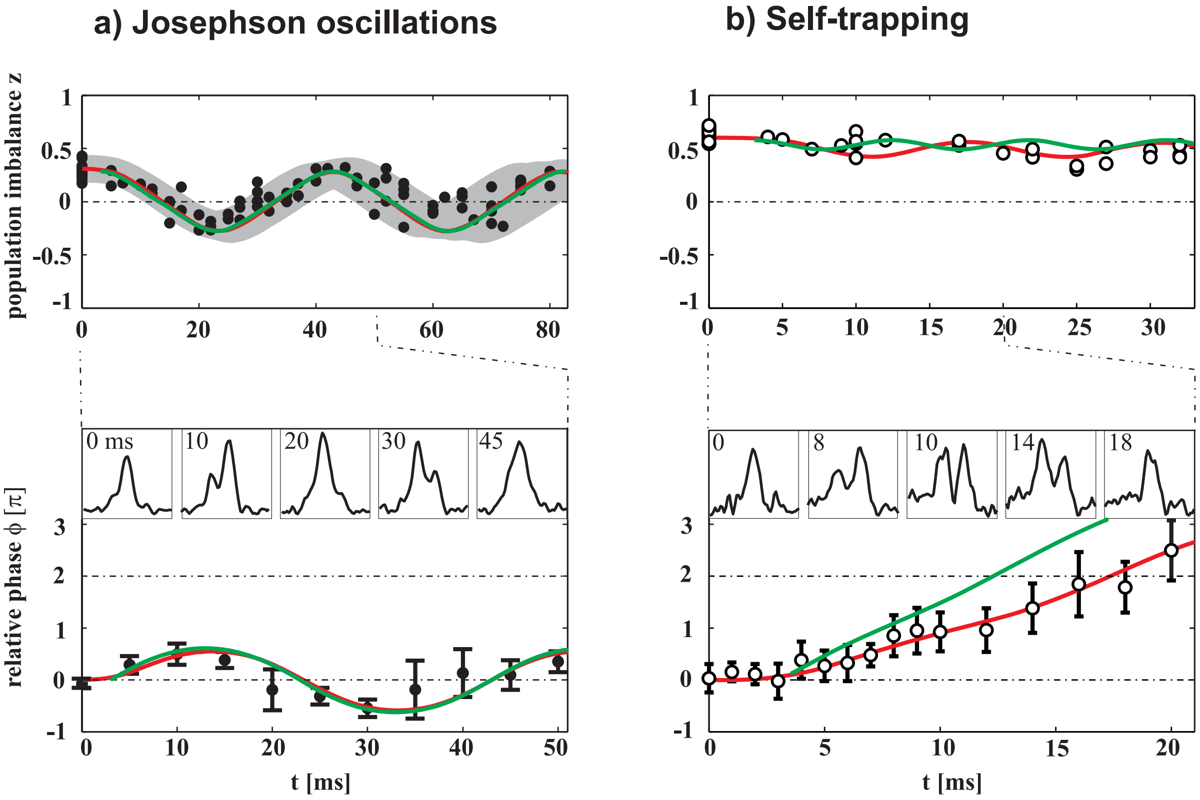

Figure 5.9: Quantitative analysis of the time evolution of the dynamical variables. a) In the Josephson oscillation regime ($z(0) = 0.28(6)$), the population imbalance as well as the relative phase oscillate around a zero mean value with a timescale of 40(2) ms. The numerical solution of the NPSE (red line) and the prediction of the VTM (green line) without free parameter show excellent agreement with the experimental data (filled circles). The gray shaded region in the upper graph indicates the theoretically expected scattering of the data due to the uncertainty in the initial population imbalance. b) In the self-trapping regime ($z(0) = 0.62(6)$) the population imbalance is nearly stationary within the depicted timescale. The relative phase evolves unbound due to the big difference between the chemical potentials in the two wells. The deviation of the VTM is due to an overestimation of the difference between the chemical potentials in the two wells (see text).

reaches the initial value after 45 ms.

The transition from the Josephson tunneling regime to the self-trapping regime is implemented experimentally by increasing the initial population imbalance $z(0)$ above the critical value $z_c = 0.38$. Figure 5.8b shows the time evolution of the BEC after switching to the symmetric double well case for $z(0) = 0.62(6)$ which corresponds to $\Delta x = 500(80)$ nm. The population of the two wells is stationary within the experimental errors. This effect of macroscopic quantum self-trapping is due to the nonlinear interatomic interaction and is absent in any former realization of weak links in superfluids or superconductors.

The quantitative analysis of the Josephson dynamics is shown in figure 5.9 in both dynamical regimes. The upper graph in figure 5.9a shows the experimental results on the time evolution of the population imbalance (filled circles) in the Josephson oscillation regime with z(0)=0.28(6) for two tunneling periods. The experimentally determined tunneling time is 40(2) ms which is significantly shorter than the linear tunneling time

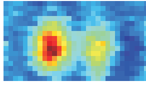

of 500(50) ms expected for non-interacting atoms in the realized potential. This reveals the important role of the nonlinear atom-atom interaction in bosonic Josephson junction experiments. The population imbalance oscillates around the mean value $\langle z(t)\rangle_t = 0$, which shows that we have indeed realized a symmetric double well potential. The results of the numerical integration of the NPSE using the calibrated parameters are represented by the red line. This simulation includes the finite response time $\Delta t = 7\,\mathrm{ms}$ of the piezo actuated mirror mount. The theoretical prediction without free parameters shows excellent agreement with the experimental data. The gray shaded region is the theoretically expected scattering of the data due to uncertainties of the initial parameters. In order to obtain this region, the time evolution of the population imbalance is calculated for different atom numbers $1000 < N_T < 1300$ and initial relative shifts $160\,\mathrm{nm} < \Delta x < 320\,\mathrm{nm}$. The lower and upper bound of the region is subsequently determined by taking the minimum and the maximum of all calculated population imbalances for each evolution time. It broadens for larger evolution times due to different tunneling frequencies for different initial population imbalances and atom numbers. The results of the extended two mode approximation (variable tunneling model) is represented with green lines[6]. Since the piezo response time of 7 ms can not be included in this theory, the results are shifted by 3.5 ms in time. The VTM is in excellent agreement with the experimental data and the solution of the NPSE.

The lower graph shows the relative phase of the two localized modes (filled circles) in the individual wells for one tunneling period. This phase is obtained from the double slit interference patterns formed after releasing the BEC from the double well trap for a time-of-flight of 5 ms before taking an absorption image. The insets show typical interference patterns obtained by integrating the absorption images along the y-and z-direction. The indicated times represent the evolution times before switching off the double well trap. The relative phase oscillates with an amplitude of $0.6(1)\pi$ around its mean value $\langle \phi \rangle_t = 0$ and the same period of 40(5) ms as the population imbalance. The indicated error bars denote statistical errors arising from the uncertainty of the initial population imbalance. Each point in the phase measurement is the result of the average over at least 5 realizations. The solutions of the NPSE (red line) and of the VTM (green line) show quantitative agreement with our experimental findings.

The dynamics of the system changes drastically if the population imbalance is increased above the critical value z_c. Figure 5.9b shows the time evolution of the dynamic variables for $z(0) = 0.62(6)$. The experimentally obtained population imbalance, which is represented with open circles in the upper graph, shows no time evolution within the experimental errors for the depicted time scale. The theoretical predictions show small amplitude oscillations of the population imbalance, which can not be resolved experimentally. The relative phase, which is measured after 8 ms time of-flight is depicted in the lower graph for one oscillation period. It is now unbound and winds up quickly over time reaching the value $\phi = \pi$ already after 9(1) ms. This quick evolution of the relative phase is due to the large difference between the on-site interactions of the left and right well. The resulting phase evolution can no longer be compensated by the atomic tunneling leading to a linearly increasing relative phase. The initial deviation from a linear time dependence is due to the finite response time of the piezo actuated mirror. In the

---

[6] The symmetric ground state and the first excited antisymmetric state are calculated by numerically integrating the three-dimensional GPE for the experimentally implemented atom number and double well potential without free parameters.

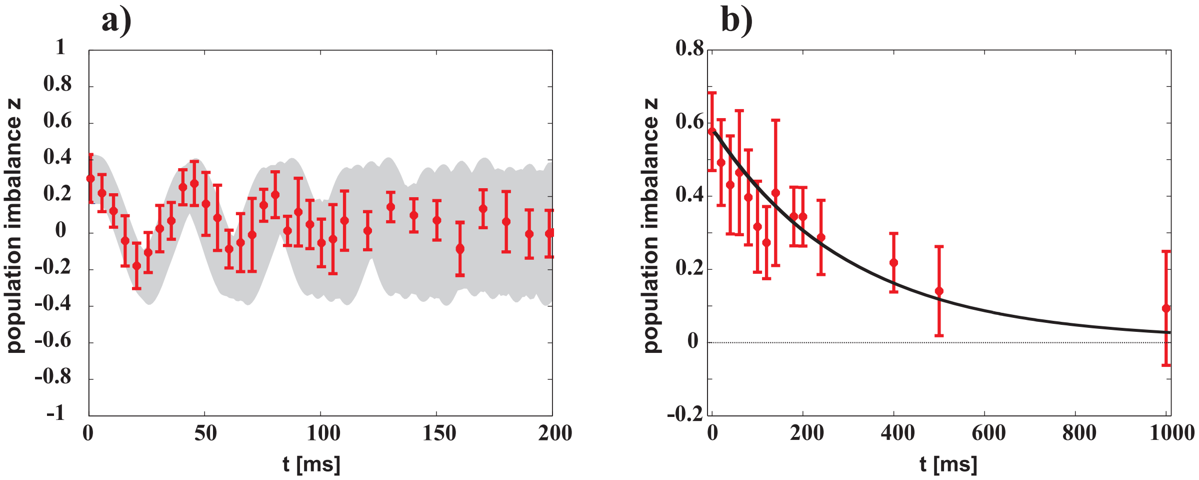

Figure 5.10: Time evolution of the population imbalance for long propagation times. a) The experimentally observed tunneling oscillations (filled red circles with statistic and systematic errors) are damped out after two oscillations periods, which is in agreement with the numerical solution of the NPSE for different initial populations (gray shaded region). b) Decay of the self-trapped state for long evolution times. The black line shows an exponential fit with a 1/e timescale of 280(80) ms. The decay is due to a finite temperature or an instability of the experimental system.

self-trapping regime, the solution of the VTM shows deviations from the experimental data. This can be understood by realizing, that the VTM is based on the assumption of localized spatial wavefunctions, which are independent on the atom number in the respective mode. These wavefunctions are calculated by superpositions of the symmetric and antisymmetric states of the double well potential and are therefore correct for $N_1 = N_2 = N_T/2$. In the self-trapping regime, the large population imbalance $z(0)$ leads to a broadening of the localized mode containing the larger number of atoms. This is not captured by the VTM, which therefore overestimates the difference in the chemical potential leading to a faster increase of the relative phase and a faster evolution of the population imbalance.

It is important to note, that the constant tunneling two-mode approximation fails to explain our experimental findings. A calculation of the normalized on-site interaction for the potential and atom numbers used in the experiments yields $\Lambda = 76$ corresponding to $z_{c,CTM} = 0.23$. Therefore, the CTM predicts a macroscopically self-trapped state for an initial population imbalance $z(0) = 0.28$, which is in contrast to the experimental results revealing Josephson oscillations.

The evolution of the population imbalance for long propagation times is shown in figure 5.10. Graph a) shows the experimental data (filled red circles) in the Josephson oscillation regime for evolution times up to 200 ms and the values, which are theoretically expected from the solution of the NPSE (gray shaded region). The error bars represent systematic errors in the determination of the population imbalance as well as statistic errors. The experimentally observed oscillation of the population imbalance is clearly damped out after two periods. The scattering of the experimental data especially for large oscillation times is due to the uncertainty in the initial population imbalance and can be explained by the numerical solution of the NPSE. However, the experimental errors are smaller than the expected scattering. This additional damping is most likely

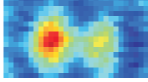

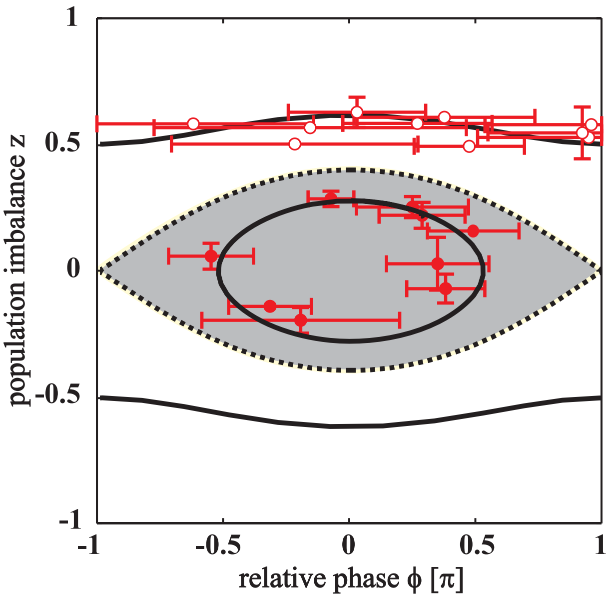

Figure 5.11: Comparison of the experimentally obtained phase plane trajectories to the predictions of the extended two-mode model (black lines). The Josephson oscillation regime (gray shaded region) is characterized by closed trajectories (filled circles). The separatrix, which is represented by the dashed line, constitutes the transition to the self-trapped regime (open circles).

due to the residual thermal cloud, which is not included in the NPSE. Graph b) shows the experimentally measured population imbalance in the self-trapping regime for evolution times up to 1 s. Clearly, the self-trapped state decays to the equally populated state ($z_{\mathrm{final}} = 0$). The black line shows an exponential fit with a 1/e timescale of 280(80) ms. This timescale is significantly smaller than the lifetime of the BEC in the double well potential, which is on the order of 10 s. The decay can either be due to an instability of the experimental setup or to finite temperature effects, which are not included in the Gross-Pitaevskii equation. Those damping effects have already been investigated in the framework of the two-mode approximation [34, 79]. However, as discussed in chapter 3, the two-mode approximation does not apply for the experimentally accessible atom numbers and well spacings. Therefore, a determination of an upper bound for the temperature of the BEC from the timescale of the decay of the self-trapped state is only possible by including finite temperature effects in the numerical integration of the NPSE or at least in the extended two mode model. We are currently investigating the effect of thermal and quantum fluctuations by measuring the fluctuations of the relative phase of the two localized modes as a function of the barrier potential depth. As discussed in [101], this measurement should allow for a determination of the temperature of the Bose-Einstein condensate inside the double well potential.

Phase plane portrait

The distinction between the two dynamical regimes becomes very apparent in the phase plane portrait of the two dynamical variables z and ϕ. This is shown in figure 5.11, where the experimental data set is compared to the predictions of the extended two-mode model. The experimentally obtained closed phase plane trajectory in the Josephson-

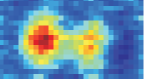

regime z(0)=0.28(6) is depicted with filled red circles. The error bars represent statistical errors and mainly result from the high sensitivity of the relative phase on the initial population imbalance especially for long evolution times. The prediction of the VTM (black line) is in quantitative agreement with the experimental findings. The dotted line shows the separatrix for $z(0) = z_{c,VTM} = 0.35$. It constitutes the crossing between the Josephson oscillation regime (gray shaded region) and the self-trapped regime, which is characterized by open phase plane trajectories (open circles).

The presented experiments cover only the phase plane trajectories with zero initial phase. The dynamical regimes of $\pi-$phase oscillations and self-trapping are so far inaccessible experimentally. There is still plenty of future experiments to be done with Josephson junctions for Bose-Einstein condensates.

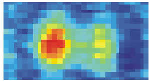

6 Experiments with BECs in optical lattices

In this chapter, experiments are presented which have been carried out during the first two years of my PhD period. The experiments investigated nonlinear wavepacket propagation in a one-dimensional optical lattice oriented along a one-dimensional waveguide. In contrast to the Josephson junction experiment, the optical lattice is realized by two counter-propagating far red detuned laser beams resulting in a lattice spacing of $d \approx 400\,\mathrm{nm}$. By introducing a frequency difference between the two beams, a moving optical lattice can be realized. The one-dimensional waveguide, or rather the two-dimensional harmonic confinement, is realized by a focused far off-resonant laser beam, which is referred to as dipole trap in the previous chapters. After condensation in the crossed optical dipole trap, the BEC is adiabatically loaded into the optical lattice. The size of the atomic cloud in x-direction and therefore the number of occupied lattice sites[1] can be adjusted by controlling the intensity of the crossed dipole trap. After this preparation stage, the BEC is released into the one-dimensional situation by switching off the crossed dipole trap beam.

The dispersion relation of free particles can be modified by exposing them to a periodic potential. As known from solid state physics [102], stationary solutions of the Schrödinger equation in the presence of a periodic potential are given by the Bloch functions

$$\Psi(x) = \phi_{n,k}(x) = u_{n,k}(x) \exp(ikx)\,, \tag{6.1}$$

where $u_{n,k}(x) = u_{n,k}(x+d)$ are periodic functions with the same periodicity as the external potential and k is the quasi-momentum of the atomic cloud, which can be controlled by adjusting the velocity of the moving optical lattice. The energy eigenvalues $E_n(k) = E_n(k + 2\pi/d)$ form a band structure, where the different bands are labeled by the band index n. This modified dispersion relation allows to adjust the dispersion of the atoms by adiabatically preparing the wavepacket in the first band ($n = 0$) at a given quasi-momentum. Combined with the atom-atom interaction, this makes different regimes of nonlinear wavepacket propagation accessible which will be investigated in the following sections.

---

[1] The BEC typically occupies more than 20 lattice sites.

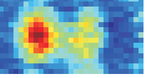

6.1 Dispersion management

The term “dispersion management” originates from nonlinear photon optics where the dispersion of light pulses can be controlled using periodic refractive index structures [86, 103]. It is nowadays also used for the altered dispersion of atoms in periodic potentials. The experiment presented here deals with the wavepacket dynamics in the regime of weak periodic potentials and weak nonlinearity[2]. The experimental results have been published in Physical Review Letters [23]. This publication is attached on the following pages. For a detailed description of the experimental system and the underlying theory see the PhD thesis of Bernd Eiermann [74]. The results can be summarized as follows:

- The first experiment shows in a descriptive way, that the dynamical evolution of the wavepacket in the first band at the Brillouin-zone edge $k_b = \pi/d$ can be characterized by an effective negative mass $m_{\text{eff}} = \hbar^2(\frac{\partial^2 E_0(k)}{\partial k^2})^{-1}$. A BEC is first prepared at zero quasi-momentum and the crossed dipole trap is subsequently switched off. After an expansion time of $t_1 = 17$ms, during which the BEC broadens by approximately 80% due to normal dispersion, the wavepacket is prepared to the Brillouin-zone edge within $dt < 1\,\text{ms}$. The BEC is imaged after a variable evolution time t_2. The negative sign of the effective mass in the phase evolution factor $\exp(-\hbar\frac{k^2}{2m}t)$ which is often referred to as anomalous dispersion, can be interpreted as a time inversion and leads to a re-compression of the atomic cloud until it reaches its initial size after $t_2 \approx 8\,\text{ms}$

- In a second experiment we investigate the applicability of the approximation of a constant effective mass. The evolution of the BEC at the edge of the Brillouin zone is measured for different potential depths of the optical lattice. For small potential depths $V_0 < 2E_G$, the small range of constant effective mass makes the inclusion of dispersion terms of higher order necessary. This leads to non-Gaussian wavepacket shapes. For higher potential depths, the wavepacket stays Gaussian during the expansion, which can now be described using the approximation of constant effective mass.

- The third experiment is finally dedicated to a systematic investigation of the extremal group velocities $v_g = \frac{1}{\hbar}\frac{\partial E_0(k)}{\partial k}$ in the first band. These maximal and minimal group velocities correspond to the quasi-momenta with infinite positive and negative effective masses.

---

[2] For the atomic densities used in this experiment, the nonlinear atom-atom interaction only results in small corrections to the wavepacket dynamics expected for non-interacting atoms.

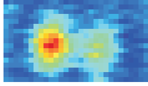

VOLUME 91, NUMBER 6 PHYSICAL REVIEW LETTERS week ending 8 AUGUST 2003

Dispersion Management for Atomic Matter Waves

B. Eiermann,[1] P. Treutlein,[1,2] Th. Anker,[1] M. Albiez,[1] M. Taglieber,[1] K.-P. Marzlin,[1] and M. K. Oberthaler[1]
[1]*Fachbereich Physik, Universität Konstanz, Fach M696, 78457 Konstanz, Germany*
[2]*Sektion Physik, Ludwig-Maximilians-Universität, Schellingstrasse 4, 80799 München, Germany*

(Received 14 March 2003; published 8 August 2003)

We demonstrate the control of the dispersion of matter wave packets utilizing periodic potentials. This is analogous to the technique of dispersion management known in photon optics. Matter wave packets are realized by Bose-Einstein condensates of ^{87}Rb in an optical dipole potential acting as a one-dimensional waveguide. A weak optical lattice is used to control the dispersion relation of the matter waves during the propagation of the wave packets. The dynamics are observed in position space and interpreted using the concept of effective mass. By switching from positive to negative effective mass, the dynamics can be reversed. The breakdown of the approximation of constant, as well as experimental signatures of an infinite effective mass are studied.

DOI: 10.1103/PhysRevLett.91.060402 PACS numbers: 03.75.Be, 03.75.Lm, 32.80.Pj

The broadening of particle wave packets due to the free space dispersion is one of the most prominent quantum phenomena cited in almost every textbook of quantum mechanics. The realization of Bose-Einstein condensates of dilute gases allows for the direct observation of wave packet dynamics in real space on a macroscopic scale [1]. Using periodic potentials it becomes feasible to experimentally study to what extent the matter wave dispersion relation can be engineered. This approach is similar to dispersion management for light pulses in spatially periodic refractive index structures [2].

First experiments in this direction have already been undertaken in the context of Bloch oscillations of thermal atoms [3] and condensates [4]. The modification of the dipole mode oscillation frequency of a condensate due to the changed dispersion relation in the presence of a periodic potential has been studied in detail [5,6]. In contrast to these experiments where the center of mass motion was studied, we are investigating the evolution of the spatial distribution of the atomic cloud in a quasi-one-dimensional situation. Our experiments show that the dispersion and thus the wave packet dynamics can be experimentally controlled. This is a new tool which also allows one to study the interplay between dispersion and atom-atom interaction and to realize predicted non-spreading wave packets such as gap solitons [7] and self-trapped states [8].

For atomic matter waves inside a one-dimensional optical waveguide, we have achieved dispersion management by applying a weak periodic potential with adjustable velocity. Figure 1 shows the results of an experiment in which the propagation of an atomic wave packet is studied in the normal [Fig. 1(b)] and anomalous [Fig. 1(c)] dispersion regime corresponding to positive and negative effective mass, respectively. A broadening of the wave packet is observed in both cases. The faster spreading in the case of anomalous dispersion is a consequence of the smaller absolute value of the negative effective mass. However, if we switch from one regime to the other during the propagation by changing the velocity of the periodic potential, the effects of normal and anomalous dispersion cancel. The wave packet, which has initially broadened under the influence of normal dispersion, reverses its expansion and compresses until it regains its initial shape [Fig. 1(d)]. This is a direct proof of the realization of negative effective mass.

The wave packets have been realized with a ^{87}Rb Bose-Einstein condensate. The atoms are collected in a magneto-optical trap and subsequently loaded into a

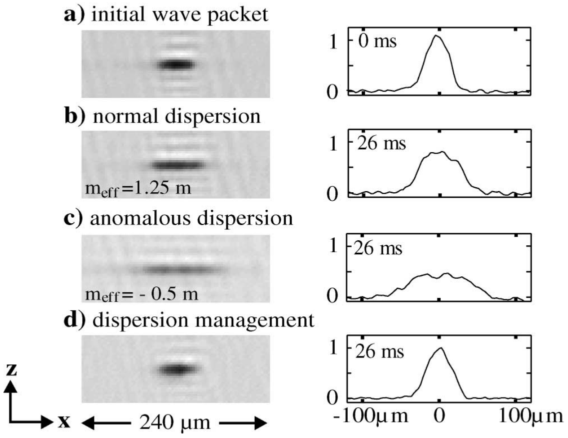

FIG. 1. Controlling the dispersion of an atomic wave packet in a waveguide using a periodic potential. Shown are absorption images of the wave packet averaged over four realizations (left) and the corresponding density distributions $n(x, t)$ along the waveguide (right). (a) Initial wave packet. (b),(c) Images taken after an overall propagation time of $t = 26$ ms for different dispersion regimes with different effective masses as indicated. (d) Wave packet subjected to dispersion management: an initial stage of expansion for $t = 17$ ms with normal dispersion is followed by propagation with anomalous dispersion for $t = 9$ ms. The broadening in the normal dispersion regime has been reversed by anomalous dispersion.

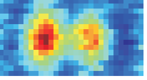

magnetic time-orbiting potential trap. By evaporative cooling we produce a cold atomic cloud which is then transferred into an optical dipole trap realized by two focused Nd:YAG laser beams with 60 μm waist crossing at the center of the magnetic trap. Further evaporative cooling is achieved by lowering the optical potential leading to pure Bose-Einstein condensates with up to 3×10^4 atoms in the $|F = 2, m_F = +2\rangle$ state. By switching off one dipole trap beam the atomic matter wave is released into a trap acting as a one-dimensional waveguide with radial trapping frequency $\omega_\perp = 2\pi \times 80\,\mathrm{Hz}$ and longitudinal trapping frequency $\omega_\| = 2\pi \times 1.5\,\mathrm{Hz}$.

The periodic potential is realized by a far off-resonant standing light wave with a single beam peak intensity of up to $5\,\mathrm{W/cm^2}$. The chosen detuning of 2 nm to the blue off the D2 line leads to a spontaneous emission rate below 1 Hz. The frequency and phase of the individual laser beams are controlled by acousto-optic modulators driven by a two channel arbitrary waveform generator allowing for full control of the velocity and amplitude of the periodic potential. The absolute value of the potential depth was calibrated independently by analyzing results on Bragg scattering [9] and Landau Zener tunneling [4,10].

The wave packet evolution inside the combined potential of the waveguide and the lattice is studied by taking absorption images of the atomic density distribution after a variable time delay. The density profiles along the waveguide, $n(x, t)$, are obtained by integrating the absorption images over the transverse dimension z.

The concept of effective mass m_{eff} [11] allows one to describe the dynamics of matter wave packets inside a periodic potential in a simple way via a modified dispersion relation. The periodic potential in our experiments is well described by

$$V(x) = \frac{V_0}{2}\cos(Gx)$$

with a modulation depth V_0 on the order of the grating recoil energy $E_G = \hbar^2 G^2/8m$, with $G = 2\pi/d$ where $d = 417\,\mathrm{nm}$ represents the spatial period. The energy spectrum of atoms inside the periodic potential exhibits a band structure $E_n(q)$ which is a periodic function of quasimomentum q with periodicity G corresponding to the width of the first Brillouin zone [Fig. 2(a)]. In our experiment, we prepare condensates in the lowest energy band ($n = 0$) with a quasimomentum distribution $w(q)$ centered at $q = q_c$ with an rms width $\Delta q \ll G$ [12].

It has been shown by Steel *et al.* [13] that in this case the condensate wave function in a quasi-one-dimensional situation can be described by $\Psi(x, t) = A(x, t)\ \phi_{q_c}(x) \times \exp[-iE_0(q_c)t/\hbar]$, where ϕ_{q_c} represents the Bloch function in the lowest energy band corresponding to the central quasimomentum. The evolution of the envelope function $A(x, t)$, normalized to the total number of atoms N_0, is described by

$$i\hbar\left(\frac{\partial}{\partial t} + v_g\frac{\partial}{\partial x}\right)A = -\frac{\hbar^2}{2m_{\mathrm{eff}}}\frac{\partial^2}{\partial x^2}A + \tilde{g}|A|^2 A. \qquad (1)$$

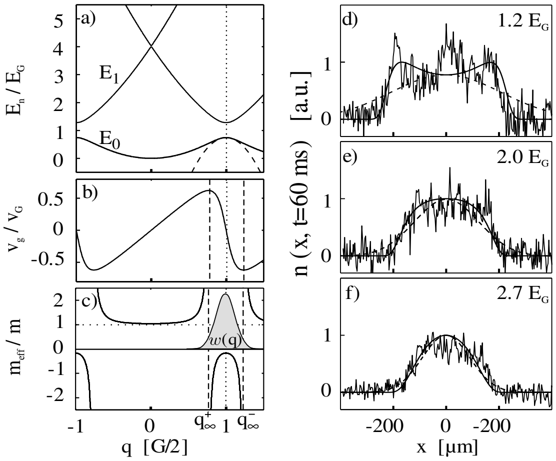

FIG. 2. (a) Band structure in the first Brillouin zone for atoms in an optical lattice with $V_0 = 1.2\,E_G$ (solid), parabolic approximation to the lowest energy band at $q = G/2$ (dashed), corresponding group velocity (b), and effective mass (c) in the lowest energy band. The vertical dashed lines at $q = q_\infty^\pm$ indicate where $|m_{\mathrm{eff}}| = \infty$. (d)–(f) Spatial densities of the wave packet after $t = 60\,\mathrm{ms}$ of propagation with $q_c = G/2$ for different V_0. The position x along the waveguide is measured in the moving frame of the optical lattice. The solid lines represent the theoretical predictions using linear propagation with the exact band structure and the quasimomentum distribution given in graph (c). The dashed lines in graphs (d)–(f) represent the prediction of the constant effective mass approximation.

The strength of the atom-atom interaction is given by $\tilde{g} = \alpha_{nl} 2\hbar\omega_\perp a$, with the s-wave scattering length a, and a renormalization factor $\alpha_{nl} = (1/d)\int_0^d dx|\phi_{q_c}|^4$. Besides the modification of the nonlinear term the periodic potential leads to a group velocity of the envelope $A(x, t)$ determined by the energy band via $v_g(q_c) = \hbar^{-1}[\partial E_0(q)/\partial q]|_{q_c}$ [Fig. 2(b)]. In addition, the kinetic energy term describing the dispersion of the wave packet is modified by the effective mass [Fig. 2(c)]

$$m_{\mathrm{eff}}(q_c) = \hbar^2\left[\frac{\partial^2 E_0(q)}{\partial q^2}\bigg|_{q_c}\right]^{-1}.$$

Since this approximation of constant effective mass corresponds to a parabolic approximation of the energy band, it is valid only for sufficiently small Δq.

The general solution of Eq. (1) is a difficult task, but simple analytic expressions can be found in the special cases of negligible and dominating atom-atom interaction. Omitting the last term in Eq. (1) it is straightforward to see that $|m_{\mathrm{eff}}|$ controls the magnitude of the dispersion term and thus the time scale of the wave packet broadening. A change in sign of m_{eff} corresponds to time reversal of the dynamics in a frame moving with velocity v_g. In the regime where the atom-atom interaction is dominating, e.g., during the initial expansion of a condensate, the evolution of the envelope function can be found in standard nonlinear optics textbooks [2] and in the form of scaling solutions in the context of Bose-Einstein condensates [14]. Note that in this regime the kinetic energy term is still relevant and thus a change of the sign of the effective mass will reverse the dynamics.

In the following we will analyze the obtained experimental results in more detail. The initial wave packet shown in Fig. 1(a) contains 2×10^4 atoms and is characterized by $\Delta x_0 = 14.8(6)\,\mu\text{m}$ (Δx is the rms width of a Gaussian fit). Before releasing the atomic cloud into the one-dimensional waveguide, a weak periodic potential along the waveguide is adiabatically ramped up to $V_0 = 2.8(2)\,E_G$ within 6 ms. This turns the initial Gaussian momentum distribution of the atoms into a Gaussian distribution of quasimomenta $w(q)$ centered at $q_c = 0$ with a corresponding effective mass $m_{\text{eff}} = 1.25\,m$. The density distribution shown in Fig. 1(b) is a result of propagation within the stationary periodic potential for $t = 26$ ms and exhibits a spread of $\delta x := \sqrt{\Delta x(t)^2 - \Delta x_0^2} = 18.4(12)\,\mu\text{m}$ in contrast to $\delta x_f = 20.2(14)\,\mu\text{m}$ for expansion without periodic potential. The resulting ratio $\delta x_f/\delta x = 1.10(15)$ indicates that the evolution is dominated by the nonlinearity, in which case one expects $\delta x_f/\delta x \approx \sqrt{m_{\text{eff}}/m} = 1.11$ in the short-time limit [15]. In the case of linear propagation one expects $\delta x_f/\delta x = m_{\text{eff}}/m = 1.25$.

The dynamics in the anomalous dispersion regime [Fig. 1(c)] are investigated by initially accelerating the periodic potential within 3 ms to a velocity $v = v_G := \hbar G/2m$, thus preparing the atomic wave packet at the edge of the Brillouin zone ($q_c = G/2$), where $m_{\text{eff}} = -0.5\,m$. The velocity is kept constant during the subsequent expansion. In the regime of negative mass a condensate exhibits collapse dynamics. Two-dimensional calculations for our experimental situation reveal that this collapse happens within the initial 3–6 ms of propagation. Subsequently this leads to an excitation of transverse states and thus to a fast reduction of the density and the nonlinearity. An indication of the population of transverse states is the observed increase of the transverse spatial extension of the wave packets by almost a factor of 2. The optical resolution of our setup does not allow for a quantitative analysis of the transverse broadening. Because of the fast reduction of the nonlinearity the subsequent expansion should be well described by linear theory predicting a ratio $\delta x_f/\delta x = 0.5$ which is close to the observed value 0.46(5) [$\delta x = 38.5(15)\,\mu\text{m}$ after 23 ms].

In the case of dispersion management Fig. 1(d) the wave packet was first subjected to normal dispersion for 17 ms at $q_c = 0$. The time of subsequent propagation with anomalous dispersion at $q_c = G/2$ was adjusted to achieve the minimal wave packet size of $\Delta x = 15.4(2)\,\mu\text{m}$. The minimum was achieved for times ranging from 7 to 9 ms which is in rough agreement with the expected time resulting from effective mass considerations $\sqrt{0.5/1.25} \times 17\,\text{ms} = 10.7\,\text{ms}$.

Since the assumption of a constant effective mass used so far is only an approximation, it is important to check its applicability in experiments. Therefore we investigate the dynamics of wave packets prepared at the Brillouin zone edge for different potential depths. The observed density profiles after 60 ms of propagation are shown in Figs. 2(d)–2(f). While both the initial wave packet shape $n(x, 0)$ and the quasimomentum distribution $w(q)$ are measured to be approximately Gaussian, the wave packet changes its shape during evolution. We attribute this distortion to the invalidity of the constant effective mass approximation, which assumes that the populated quasimomenta experience the same negative curvature of $E_0(q)$. Since the range of quasimomenta fulfilling this criterion becomes smaller with decreasing modulation depth, a more pronounced distortion of the wave packet shape for weak potentials is expected [see Fig. 2(d)].

This explanation is confirmed more quantitatively by comparing the observed wave packets with the results of a linear theory. Since the initial collapse of the condensate cannot be described by a linear theory, we take a Gaussian function fitted to the density distribution measured at 20 ms as the initial wave packet for the numerical propagation. Because of the fact that this is not a minimum uncertainty wave packet we add a quadratic phase in real space such that the Fourier transform of the wave packet is consistent with the measured momentum distribution. In first approximation this takes into account the initial expansion including the repulsive atom-atom interaction. For the subsequent propagation of 40 ms in quasimomentum space we use the full expression for $E_0(q)$ which is obtained numerically. In Fig. 2(d)–2(f) we compare the data with the linear theory described above (solid line) and with the constant effective mass approximation (dashed line). Clearly the constant effective mass approximation cannot explain the observed distortion and it strongly overestimates the expansion velocity for weak potentials. Additionally, for small potential modulation depths new features appear in the central part of the wave packet which cannot be explained using the linear theory. We are currently investigating these features in more detail.

The observed distortion is mainly a consequence of another very interesting feature of the band structure: the existence of $|m_{\text{eff}}| = \infty$ for certain quasimomenta $q = q_\infty^\pm$ [see Fig. 2(c)]. A diverging mass implies that the group velocity is extremal and the dispersion vanishes as can be seen from Eq. (1). As a consequence an atomic ensemble whose quasimomentum distribution is overlapping $q = q_\infty^\pm$ will develop steep edges as can be seen in Fig. 2(d) and in Fig. 3. These edges propagate with the maximum group velocity of the lowest band.

The systematic investigation of the velocities of the edges is shown in Fig. 3 for different values of V_0. In order to get a significant overlap of $w(q)$ with $q = q_\infty^\pm$, we

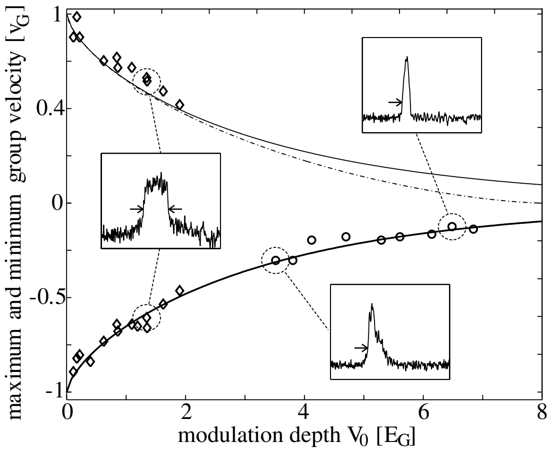

FIG. 3. Group velocities of steep edges emerging from an initial wave packet with significant overlap with $q_{\infty}^{\pm}$ in quasimomentum space. The measured velocities of the indicated positions (arrows in insets) agree very well with the expected maximum and minimum velocity in the lowest band (solid line) corresponding to the infinite masses. The dashed line represents the prediction of the weak potential approximation [11]. For potentials smaller than 2 E_G (diamonds) data are obtained by preparing the initial wave packet at $q = G/2$ leading to two steep edges (see inset). For higher potentials (circles) the wave packet is prepared at $q = G/4$ to ensure population of the quasimomentum corresponding to infinite mass.

prepare atomic ensembles with $\Delta q = 0.17\,G/2$ at $q_c = G/2$ realized by Bose-Einstein condensates of 2×10^4 atoms with a spatial extension of $\Delta x = 15\ \mu$m. The velocities of the edges are derived from two images taken at 20 and 60 ms, respectively. In each image the position of the edge is evaluated at the levels indicated by the arrows in the insets of Fig. 3 (50% and 25% of the maximum density). Since the momentum spread is too small to populate the infinite mass points for potentials deeper than 2 E_G the atomic ensemble was then prepared at $q_c = G/4$. The resulting wave packet shapes are asymmetric exhibiting a steep edge on one side which becomes less pronounced for potentials deeper than 5 E_G. The obtained experimental results in Fig. 3 are in excellent agreement with the numerically calculated band structure predictions. In contrast to the good agreement of the maximum velocity for all potential depths we find that for $V_0 > 5\,E_G$ the group velocity of the center of mass is only 10% of the expected velocity. This could be an indication of entering the tight binding regime where the nonlinear effect of self-trapping, i.e., stopping and nonspreading wave packets, has been predicted [8]. We are currently investigating the transport properties in this regime in more detail.

In conclusion, we have demonstrated experimentally that the dispersion of atomic matter waves in a waveguide can be controlled using a weak periodic potential. Matter wave packets with positive, negative, and infinite effective masses are studied in the regime of weak and intermediate potential heights. The preparation of matter waves with engineered dispersion ($m_{\mathrm{eff}} < 0$) is an important prerequisite for the experimental investigation of atomic gap solitons and other effects arising from the coherent interplay of nonlinearity and dispersion in periodic potentials.

We wish to thank J. Mlynek for his generous support, A. Sizmann and B. Brezger for many stimulating discussions, and J. Bellanca and K. Forberich for their help in building up the experiment. This work was supported by Deutsche Forschungsgemeinschaft, Emmy Noether Program, and by the European Union, Contract No. HPRN-CT-2000-00125.

Note added.—Only recently, we became aware of an experimental work [16] which is closely related to the work presented in this Letter.

[1] *Bose-Einstein Condensation in Atomic Gases*, edited by M. Inguscio, S. Stringari, and C. Wieman (IOS Press, Amsterdam, 1999).
[2] G. P. Agrawal, *Applications of Nonlinear Fiber Optics* (Academic Press, San Diego, 2001); *Nonlinear Fiber Optics* (Academic Press, San Diego, 1995).
[3] M. Ben Dahan, E. Peik, J. Reichel, Y. Castin, and C. Salomon, Phys. Rev. Lett. **76**, 4508 (1996).
[4] B. P. Anderson and M. A. Kasevich, Science **282**, 1686 (1998); O. Morsch, J. Müller, M. Cristiani, D. Ciampini, and E. Arimondo, Phys. Rev. Lett. **87**, 140402 (2001).
[5] S. Burger, F. S. Cataliotti, C. Fort, F. Minardi, M. Inguscio, M. L. Chiofalo, and M. P. Tosi, Phys. Rev. Lett. **86**, 4447 (2001).
[6] M. Krämer, L. Pitaevskii, and S. Stringari, Phys. Rev. Lett. **88**, 180404 (2002).
[7] P. Meystre, *Atom Optics* (Springer-Verlag, New York, 2001), p. 205, and references therein.
[8] A. Trombettoni and A. Smerzi, Phys. Rev. Lett. **86**, 2353 (2001).
[9] M. Kozuma, L. Deng, E.W. Hagley, J. Wen, R. Lutwak, K. Helmerson, S. L. Rolston, and W. D. Phillips, Phys. Rev. Lett. **82**, 871 (1999).
[10] C. F. Bharucha, K.W. Madison, P. R. Morrow, S. R. Wilkinson, Bala Sundaram, and M. G. Raizen, Phys. Rev. A **55**, R857 (1997).
[11] N. Ashcroft and N. Mermin, *Solid State Physics* (Saunders, Philadelphia, 1976).
[12] J. Hecker-Denschlag, J. E. Simsarian, H. Häffner, C. McKenzie, A. Browaeys, D. Cho, K. Helmerson, S. L. Rolston, and W. D. Phillips, J. Phys. B **35**, 3095 (2002), and references therein.
[13] M. Steel and W. Zhang, cond-mat/9810284.
[14] Y. Castin, and R. Dum, Phys. Rev. Lett. **77**, 5315 (1996); Yu. Kagan, E. L. Surkov, and G.V. Shlyapnikov, Phys. Rev. A **54**, R1753 (1996).
[15] M. J. Potasek, G. P. Agrawal, and S. C. Pinault, J. Opt. Soc. Am. B **3**, 205 (1986).
[16] L. Fallani, F. S. Cataliotti, J. Catani, C. Fort, M. Modugno, M. Zawada, and M. Inguscio, cond-mat/0303626.

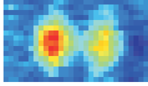

6.2 Continuous dispersion management

In the experiment described above, the wavepacket has been prepared to a fixed quasi-momentum. The concept of dispersion management can be expanded to a continuously varying quasi-momentum ("continuous dispersion management"). The corresponding experiments have been carried out with a slightly modified setup, in which the one-dimensional waveguide and the optical lattice are not collinear, but enclose an angle of $\alpha = 21°$. If the acceleration time of the periodic confinement to a certain velocity corresponding to a given quasi-momentum is not adiabatic with respect to the transverse harmonic confinement, transverse collective excitations inside the waveguide are excited. The resulting oscillation of the wavepacket has a component along the optical lattice. This leads to a continuous oscillation of the quasi-momentum. Combined with the nonlinear nature of atom-atom interaction, a rich variety of different regimes of wavepacket dynamics in real and momentum space can be realized. The experimental results as well as a simple theoretical model explaining the data have been published in Optics Express [24] (attached in the following pages). Two different acceleration schemes to the edge of the Brillouin zone have been investigated:

- In the first experiment, the BEC is prepared to $k = 1.5\, k_b$ within 3 ms at a potential depth $V_0 = 6E_{\text{rec}}$. The lattice is subsequently reduced to $V_0 = 0.52E_{\text{rec}}$ and decelerated within 3 ms in order to finally prepare the wavepacket at the band edge. The dynamical evolution of the wavepacket is observed for expansion times up to 50ms. After an initial stage of nonlinear pulse compression [86], the dynamics is dominated by the continuous change of the quasi-momentum due to the transverse oscillation in the waveguide. This leads to a periodic change from positive to negative group velocities, which appears as an oscillation in real space. During the evolution, the quasi-momentum crosses the points of infinite effective mass. Since the dispersion vanishes at these points and additionally the dynamics at positive and negative masses partially compensate, the central wavepacket is only slowly spreading.

- In the second implemented preparation scheme, the periodic potential is ramped up to $V_0 = 0.37\, E_{rec}$ and the wavepacket is subsequently directly prepared to $k = 1.05\, k_b$ within 3ms. After an initial stage of compression, the dynamics reveals a very complex time evolution. The wave packet repeatedly splits up into two parts in real space and shows a reduced dispersion. This behavior can only be explained by including the nonlinear atom-atom interaction.

A detailed description of the experiments and the numerical simulations will be presented in the PhD thesis by Thomas Anker.

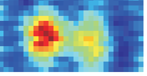

Linear and nonlinear dynamics of matter wave packets in periodic potentials

Th. Anker, M. Albiez, B. Eiermann, M. Taglieber and M. K. Oberthaler

Kirchhoff Institut für Physik, Universität Heidelberg, Im Neuenheimer Feld 227, 69120 Heidelberg

thomas.anker@kip.uni-heidelberg.de

http://www.kip.uni-heidelberg.de/matterwaveoptics

Abstract: We investigate experimentally and theoretically the nonlinear propagation of ^{87}Rb Bose Einstein condensates in a trap with cylindrical symmetry. An additional weak periodic potential which encloses an angle with the symmetry axis of the waveguide is applied. The observed complex wave packet dynamics results from the coupling of transverse and longitudinal motion. We show that the experimental observations can be understood applying the concept of effective mass, which also allows to model numerically the three dimensional problem with a one dimensional equation. Within this framework the observed slowly spreading wave packets are a consequence of the continuous change of dispersion. The observed splitting of wave packets is very well described by the developed model and results from the nonlinear effect of transient solitonic propagation.

OCIS codes: (270.5530) Pulse propagation and solitons; (020.0020) Atomic and molecular physics; (350.4990) Particles

---

References and links

1. “Bose-Einstein condensation in atomic gases,” ed. by M. Inguscio, S. Stringari, and C. Wieman, (IOS Press, Amsterdam 1999)
2. F.S. Cataliotti, S. Burger, S. C. Fort, P. Maddaloni, F. Minardi, A. Trombettoni, A. Smerzi, and M. Ingusio, “Josephson Junction Arrays with Bose-Einstein Condensates”, Science **293** 843 (2001).
3. A. Trombettoni and A. Smerzi, “Discrete Solitons and Breathers with Dilute Bose-Einstein Condensates,” Phys. Rev. Lett. **86** 2353 (2001).
4. M. Steel and W. Zhang, “Bloch function description of a Bose-Einstein condensate in a finite optical lattice,” cond-mat/9810284 (1998).
5. P. Meystre, *Atom Optics* (Springer Verlag, New York, 2001) p 205, and references therein.
6. The experimental realization in our group will be published elsewhere.
7. V.V. Konotop, M. Salerno, “Modulational instability in Bose-Einstein condensates in optical lattices,” Phys. Rev. A **65** 021602 (2002).
8. N. Ashcroft and N. Mermin, *Solid State Physics* (Saunders, Philadelphia, 1976).
9. A.A. Sukhorukov, D. Neshev, W. Krolikowski, and Y.S. Kivshar, “Nonlinear Bloch-wave interaction and Bragg scattering in optically-induced lattices,” nlin.PS/0309075.
10. B. Eiermann, P. Treutlein, Th. Anker, M. Albiez, M. Taglieber, K.-P. Marzlin, and M.K. Oberthaler, “Dispersion Management for Atomic Matter Waves,” Phys. Rev. Lett. **91** 060402 (2003).
11. M. Kozuma, L. Deng, E.W. Hagley, J. Wen, R. Lutwak, K. Helmerson, S.L. Rolston, and W.D. Phillips, “Coherent Splitting of Bose-Einstein Condensed Atoms with Optically Induced Bragg Diffraction,” Phys. Rev. Lett. **82** 871 (1999).

#3346 - $15.00 US Received 11 November 2003; revised 21 December 2003; accepted 21 December 2003

12. B.P. Anderson, and M.A. Kasevich, “Macroscopic Quantum Interference from Atomic Tunnel Arrays,” Science **282** 1686 (1998);
13. O. Morsch, J. Müller, M. Cristiani, D. Ciampini, and E. Arimondo, “Bloch Oscillations and Mean-Field Effects of Bose-Einstein Condensates in 1D Optical Lattices,” Phys. Rev. Lett. **87** 140402 (2001).
14. C.F. Bharucha, K.W. Madison, P.R. Morrow, S.R. Wilkinson, Bala Sundaram, and M.G. Raizen, “Observation of atomic tunneling from an accelerating optical potential,” Phys. Rev. A **55** R857 (1997)
15. L. Salasnich, A. Parola, and L. Reatto, “Effective wave equations for the dynamics of cigar-shaped and disk-shaped Bose condensates,” Phys. Rev. A **65** 043614 (2002).
16. G.P. Agrawal, *Applications of Nonlinear Fiber Optics* (Academic Press, San Diego, 2001).
17. G.P. Agrawal, *Nonlinear Fiber Optics* (Academic Press, San Diego, 1995).
18. R.G. Scott, A.M. Martin, T.M. Fromholz,S. Bujkiewicz, F.W. Sheard, and M. Leadbeater, “Creation of Solitons and Vortices by Bragg Reflection of Bose-Einstein Condensates in an Optical Lattice,” Phys. Rev. Lett. **90** 110404 (2003).

---

1. Introduction

The experimental investigation of nonlinear matter wave dynamics is feasible since the realization of Bose-Einstein-condensation of dilute gases [1]. The combination of this new matter wave source with periodic potentials allows for the realization of many nonlinear propagation phenomena. The dynamics depends critically on the modulation depth of the potential. For deep periodic potentials the physics is described locally taking into account mean field effects and tunneling between adjacent potential wells. In this context wave packet dynamics in Josephson junction arrays have been demonstrated experimentally [2] and nonlinear self trapping has been predicted theoretically [3]. In the limit of weak periodic potentials and moderate nonlinearity rich wave packet dynamics result due to the modification of dispersion which can be described applying band structure theory [4]. Especially matter wave packets subjected to anomalous dispersion (negative effective mass) or vanishing dispersion (diverging mass) are of great interest. In the negative mass regime gap solitons have been predicted theoretically [5] and have been observed recently [6]. Also modulation instabilities can occur [7].

The experiments described in this work reveal wave dynamics in the linear and nonlinear regime for weak periodic potentials. The observed behavior is a consequence of the special preparation of the wave packet leading to a continuous change of the effective mass and thus the dispersion during the propagation. The initial propagation is dominated by the atom-atom interaction leading to complex wave dynamics. After a certain time of propagation slowly spreading atomic wave packets are formed which are well described by linear theory. In this work we focus on the mechanisms governing the initial stage of propagation.

The paper is organized as follows: in section 2 we describe the effective mass and dispersion concept. In section 3 we present our experimental setup and in section 4 the employed wave packet preparation schemes are discussed in detail. In section 5 the experimental results are compared with numerical simulations. We show that some features of the complex dynamics can be identified with well known nonlinear mechanisms. We conclude in section 6.

2. Effective mass and dispersion concept

In our experiments we employ a weak periodic potential which leads to a dispersion relation $E_n(q)$ shown in Fig. 1(a). This relation is well known in the context of electrons in crystals [8] and exhibits a band structure. It shows the eigenenergies of the Bloch states as a function of the quasi-momentum q. The modified dispersion relation leads to a change of wavepacket dynamics due to the change in group velocity $v_g(q) = 1/\hbar\, \partial E/\partial q$ (see Fig. 1(b)), and the group velocity dispersion described by the effective mass $m_{eff} = \hbar^2(\partial^2 E/\partial q^2)^{-1}$ (see Fig. 1(c)), which is equivalent to the effective diffraction introduced in the context of light beam propagation in optically-induced photonic lattices [9]. In our experiment only the lowest band is populated, which is characterized by two dispersion regimes, normal and anomalous dispersion,

#3346 - $15.00 US Received 11 November 2003; revised 21 December 2003; accepted 21 December 2003

corresponding to positive and negative effective mass. A pathological situation arises at the quasimomentum $q^{\pm}_{\infty}$, where the group velocity $v_g(q)$ is extremal, $|m_{eff}|$ diverges and thus the dispersion vanishes.

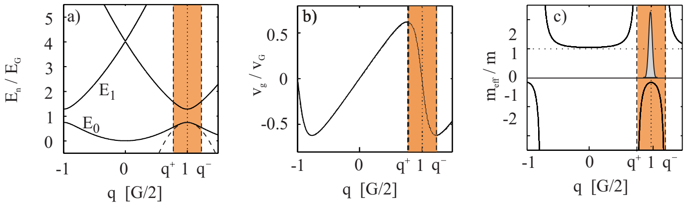

Fig. 1. (a) Band structure for atoms in an optical lattice with $V_0 = 1.2E_{rec}$ (solid), parabolic approximation to the lowest energy band at $q = \pi/d = G/2$ (dashed), corresponding group velocity (b) and effective mass (c) in the lowest energy band. The vertical dashed lines at $q = q^{\pm}_{\infty}$ indicate where $|m_{\text{eff}}| = \infty$. The shaded region shows the range of quasimomenta where the effective mass is negative.

In the following we will show that the two preparation schemes employed in the experiment lead to a continuous change of the quasimomentum distribution, and thus to a continuous change of dispersion. One of the preparation schemes allows to switch periodically from positive to negative mass values and thus a slowly spreading wave packet is formed. This is an extension of the experiment reporting on dispersion management [10]. The second preparation gives further insight into the ongoing nonlinear dynamics for the initial propagation.

3. Experimental setup

The wave packets in our experiments have been realized with a ^{87}Rb Bose-Einstein condensate (BEC). The atoms are collected in a magneto-optical trap and subsequently loaded into a magnetic time-orbiting potential trap. By evaporative cooling we produce a cold atomic cloud which is then transferred into an optical dipole trap realized by two focused Nd:YAG laser beams with $60\,\mu m$ waist crossing at the center of the magnetic trap (see Fig.2(a)). Further evaporative cooling is achieved by lowering the optical potential leading to pure Bose-Einstein condensates with $1 \cdot 10^4$ atoms in the $|F = 2, m_F = +2\rangle$ state. By switching off one dipole trap beam the atomic matter wave is released into a trap acting as a one-dimensional waveguide with radial trapping frequency $\omega_\perp = 2\pi \cdot 100\,Hz$ and longitudinal trapping frequency $\omega_\parallel = 2\pi \cdot 1.5\,Hz$. It is important to note that the dipole trap allows to release the BEC in a very controlled way leading to an initial mean velocity uncertainty smaller than 1/10 of the photon recoil velocity.

The periodic potential is realized by a far off-resonant standing light wave with a single beam peak intensity of up to $1\,W/cm^2$. The chosen detuning of 2 nm to the blue off the D2 line leads to a spontaneous emission rate below $1\,Hz$. The standing light wave and the waveguide enclose an angle of $\theta = 21^\circ$ (see Fig. 2(b)). The frequency and phase of the individual laser beams are controlled by acousto-optic modulators driven by a two channel arbitrary waveform generator allowing for full control of the velocity and amplitude of the periodic potential. The light intensity and thus the absolute value of the potential depth was calibrated independently by analyzing results on Bragg scattering [11] and Landau Zener tunneling [12, 13, 14].

The wave packet evolution inside the combined potential of the waveguide and the lattice is studied by taking absorption images of the atomic density distribution after a variable time delay. The density profiles along the waveguide, $n(x,t)$, are obtained by integrating the absorption images over the transverse dimension.

#3346 - $15.00 US Received 11 November 2003; revised 21 December 2003; accepted 21 December 2003

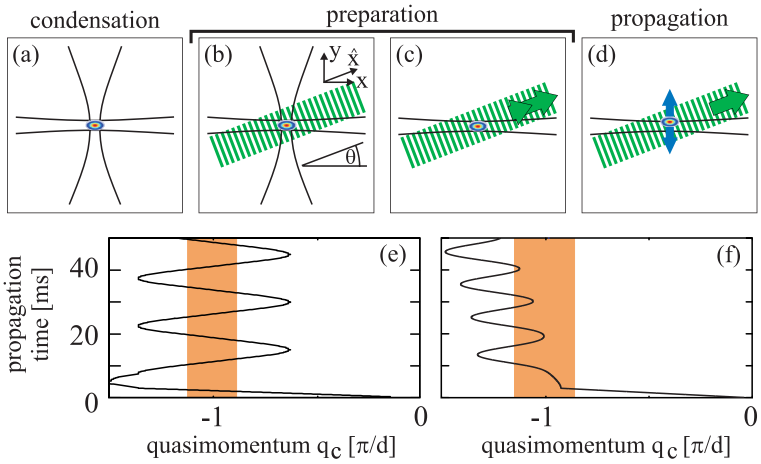

Fig. 2. Scheme for wave packet preparation (a-d). (a) initial wave packet is obtained by condensation in a crossed dipole trap. (b) A stationary periodic potential is ramped up adiabatically preparing the atoms at quasimomentum $q_c = 0$ in the lowest band. (c),(d) The periodic potential is accelerated to a constant velocity. (e) shows the numerically deduced quasimomentum shift for the preparation method I described in the text. (f) The motion of the center quasimomentum for the preparation method II described in the text. The additional shift to higher quasimomenta for long times results from the residual trap in the direction of the waveguide. The shaded area represents the quasimomenta corresponding to negative effective mass.

4. Dynamics in reciprocal space

In our experimental situation an acceleration of the periodic potential to a constant velocity leads to a collective transverse excitation as indicated in Fig. 2(d). Since the transverse motion in the waveguide has a non vanishing component in the direction of the periodic potential due to the angle θ, a change of the transverse velocity leads to a shift of the central quasimomentum of the wave packet. The coupling between the transverse motion in the waveguide and the motion along the standing light wave gives rise to a nontrivial motion in reciprocal (see Fig. 2(e,f)) and real space.

The appropriate theoretical description of the presented experimental situation requires the solution of the three dimensional nonlinear Schrödinger equation (NLSE) and thus requires long computation times. In order to understand the basic physics we follow a simple approach which solves the problem approximately and explains all the features observed in the experiment. For that purpose we first solve the semiclassical equations of motion of a particle which obeys the equation $\vec{F} = M^* \ddot{\vec{x}}$ where M^* is a mass tensor describing the directionality of the effective mass. We deduce the time dependent quasimomentum $q_c(t)$ in the direction of the periodic potential by identifying $\hbar \dot{q}_c = F_{\hat{x}}$ and $\dot{\hat{x}} = v_g(q_c)$ (definition of $\hat{x}$ see Fig. 2(b)). Subsequently we can solve the one dimensional NPSE (non-polynomial nonlinear Schrödinger equation)[15] where the momentum distribution is shifted in each integration step according to the calculated $q_c(t)$. Thus the transverse motion is taken into account properly for *narrow* momentum distributions. We use a split step Fourier method to integrate the NPSE where the kinetic energy contribution is described by the numerically obtained energy dispersion relation of the lowest band $E_0(q)$. It is important to note, that this description includes all higher derivatives of $E_0(q)$, and thus goes beyond the effective mass approximation.

In the following we discuss in detail the employed preparation schemes:

#3346 - $15.00 US Received 11 November 2003; revised 21 December 2003; accepted 21 December 2003

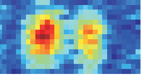

Acceleration scheme I: After the periodic potential is adiabatically ramped up to $V_0 = 6E_{rec}$ it is accelerated within 3 ms to a velocity $v_{pot} = \cos^2(\theta)1.5v_{rec}$. Then the potential depth is lowered to $V_0 = 0.52E_{rec}$ within 1.5 ms and the periodic potential is decelerated within 3 ms to $v_{pot} = \cos^2(\theta)v_{rec}$ subsequently. V_0 and v_{pot} are kept constant during the following propagation. The calculated motion in reciprocal space $q_c(t)$ is shown in Fig. 2(e).

Acceleration scheme II: The periodic potential is ramped up adiabatically to $V_0 = 0.37\,E_{rec}$ and is subsequently accelerated within 3 ms to a final velocity $v_{pot} = \cos^2(\theta) \times 1.05\,v_{rec}$. The potential depth is kept constant throughout the whole experiment. Fig. 2(f) reveals that in contrast to the former acceleration scheme the quasimomentum for the initial propagation is mainly in the negative effective mass regime.

5. Experimental and numerical results

In this section we compare the experimental results with the predictions of our simple theoretical model discussed above. The numerical simulation reveal all the experimentally observed features of the dynamics such as linear slowly spreading oscillating wave packets, nonlinear wave packet compression and splitting of wave packets. The observed nonlinear phenomena can be understood by realizing that in the negative effective mass regime the repulsive atom-atom interaction leads to compression of the wave packet in real space and to a broadening of the momentum distribution. An equivalent picture borrowed from nonlinear photon optics [16, 17] is the transient formation of higher order solitons, which show periodic compression in real space with an increase in momentum width and vice versa.

5.1. Preparation I

The experimental results for the first acceleration scheme discussed in section 4 are shown in Fig. 3. Clearly we observe that a wave packet with reduced density is formed which spreads out slowly and reveals oscillations in real space. This wave packet results from the initial dynamics characterized by two stages of compression which lead to radiation of atoms [18]. The observed behavior is well described by our numerical simulation which allows further insight into the ongoing physics.

In Fig. 3(c,d) we show the calculated momentum and real space distribution for the first 14ms of propagation. As can be seen the acceleration of the standing light wave leads to a oscillatory behavior in momentum space. For the chosen parameters the wave packet is initially dragged with a tight binding potential ($V_0 = 6E_{rec}$) over the critical negative mass regime. While the real space distribution does not change during this process, the momentum distribution broadens due to self phase modulation [16, 17]. The subsequent propagation in the positive mass regime leads to a further broadening in momentum space and real space (t=4-9ms).

The dynamics changes drastically as soon as a significant part of the momentum distribution populates quasimomenta in the negative mass regime (t=10ms). There the real space distribution reveals nonlinear compression as known from the initial dynamics of higher order solitons. This compression leads to a significant further broadening in momentum space and thus to population of quasimomenta corresponding to positive mass. This results in a spreading in real space due to the different group velocities involved and leads to the observed background. The change of the quasimomentum due to the transverse motion prohibits a further significant increase in momentum width, since the whole momentum distribution is shifted out of the critical negative mass regime at t=14ms.

The long time dynamics of the slowly spreading wave packet is mainly given by the momentum distribution marked with the shaded area for t=14ms in Fig. 3(c). The subsequent motion is dominated by the change of the quasimomentum due to the transverse motion. This leads to a periodic change from normal to anomalous dispersion and thus the linear spreading is sup-

#3346 - $15.00 US Received 11 November 2003; revised 21 December 2003; accepted 21 December 2003

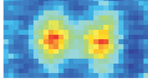

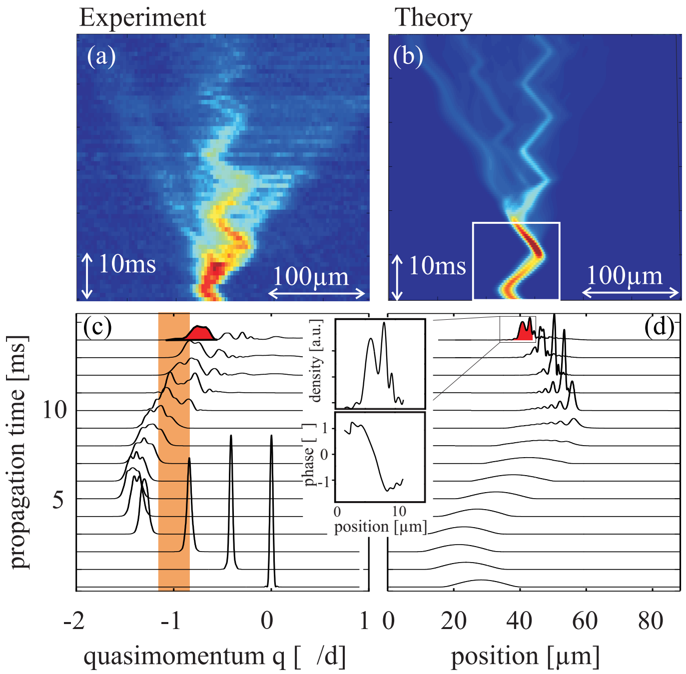

Fig. 3. Wave packet dynamics for preparation I. (a) Experimental observation of wave packet propagation. (b) Result of the numerical simulation as discussed in the text. The data is convoluted with the optical resolution of the experiment. The obtained results are in good agreement with the experimental observations. The theoretically obtained (c) quasi-momentum distribution and (d) real space distribution are given for the initial 14ms of propagation. The inset reveals the phase of the observed slowly spreading wave packet.

pressed. This is an extension of our previous work on dispersion management for matter waves - continuous dispersion management.

5.2. *Preparation II*

This preparation scheme reveals in more detail the transient solitonic propagation leading to the significant spreading in momentum space. This results in a splitting of the wave packet which cannot be understood within a linear theory. The results are shown in Fig. 4 and the observed splitting is confirmed by our numerical simulations.

In contrast to the former preparation scheme the momentum distribution is prepared as a whole in the critical negative mass regime. Our numerical simulations reveal that the wave packet compresses quickly in real space after t=4ms which is accompanied by an expansion in momentum space. The momentum distribution which stays localized in the negative mass regime reveals further solitonic propagation characterized by an expansion in real space and narrowing of the momentum distribution (t=5-10ms). The transverse motion shifts this momentum distribution into the normal dispersion regime after 11ms of propagation resulting in a wave packet moving with positive group velocity (i.e. moving to the right in fig. 4(b)). The initial compression at t=4ms even produces a significant population of atoms in the normal mass regime which subsequently move with negative group velocity showing up as a wave packet moving to the left in Fig. 4(b). Thus the splitting in real space is a consequence of the significant nonlinear broadening in momentum space.

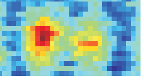

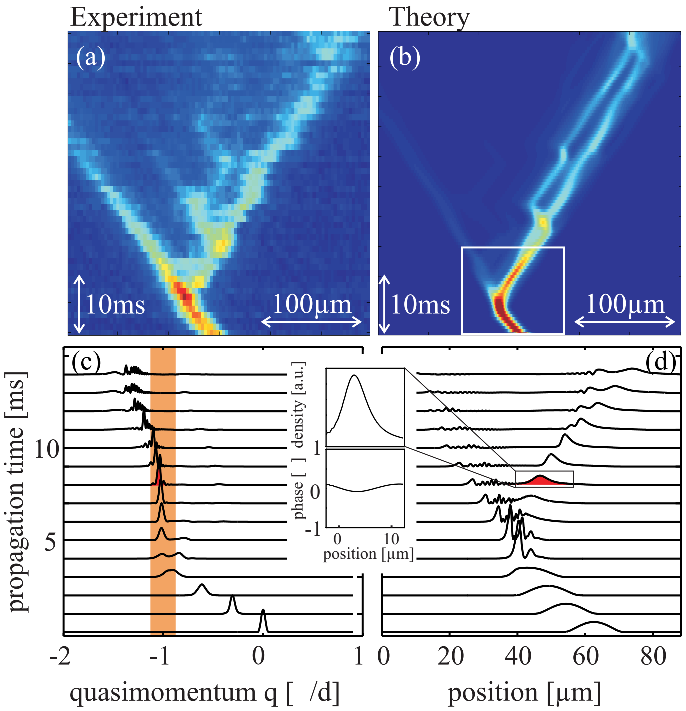

Fig. 4. Wave packet dynamics for preparation II. (a) Experimental results on wave packet propagation. (b) Result of the numerical simulation as discussed in the text. The simulation reproduces the observed wave packet splitting. The theoretically obtained (c) quasimomentum distribution and (d) real space distribution are given for the initial 14ms of propagation. The inset reveals that the transient formed wave packet has a flat phase indicating solitonic propagation.

6. Conclusion

In this paper we report on experimental observations of nonlinear wave packet dynamics in the regime of positive and negative effective mass. Our experimental setup realizing a BEC in a quasi-one dimensional situation allows the observation of wave dynamics for short times, where the nonlinearity due to the atom-atom interaction dominates and also for long times, where linear wave propagation is revealed.

We have shown that a slowly spreading wave packet can be realized by changing the quasimomentum periodically from the normal to anomalous dispersion regime. This can be viewed as an implementation of continuous dispersion management. We further investigate in detail the formation process of these packets, which are a result of the initial spreading in momentum space due to nonlinear compression. A second experiment investigates in more detail the nonlinear dynamics in the negative mass regime where the solitonic propagation leads to a significant broadening in momentum space. This shows up in the experiment as splitting of the condensate into two wave packets which propagate in opposite directions.

The developed theoretical description utilizing the effective mass tensor models the experimental system in one dimension and can explain all main features observed in the experiment.

#3346 - $15.00 US Received 11 November 2003; revised 21 December 2003; accepted 21 December 2003

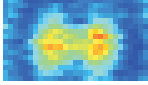

6.3 Bright atomic gap solitons for atoms with repulsive interaction

Bright solitons, which are non-spreading localized wave packets, are encountered whenever the spreading due to linear dispersion is compensated by nonlinear dynamics. For atomic matter waves, bright solitons can form if the mass m and the coupling constant g characterizing the atom-atom interaction have opposite sign $mg < 0$. They have already been demonstrated for atoms with attractive interaction [15, 14].

In the experiment presented here, the anomalous dispersion (negative effective mass) in the first band at the edge of the Brillouin zone is used to implement a bright atomic gap soliton for atoms with repulsive interaction. The experimental results have been published in Physical Review Letters [16]. The necessary pre-requisites for the observation of a gap soliton can be summarized as follows:

- The spatial size of the wavepacket has to be much larger than the periodicity d of the periodic potential. In this case, the BEC can be described by an envelope $f(x,t)$, which is modulated with the corresponding periodic Bloch functions.
- The momentum spread of the wavepacket has to be much smaller than the size of the Brillouin zone in order to prepare a constant negative effective mass. This condition implies a lower bound for the spatial size of the wavepacket.
- The experiments have to be performed in a quasi one-dimensional situation [104], in which the chemical potential of the BEC is smaller than the level spacing of the transverse harmonic confinement. This limits the maximum allowed linear atomic density to approximately $100\,\frac{\text{atoms}}{\mu\text{m}}$. It is important to note, that the existence of non-spreading wavepackets has been also predicted in two- and three-dimensional periodic potentials in the tight-binding regime [105].
- The atom number of the initially prepared wavepacket has to be on the order of the expected final atom number in the soliton, which is $N \approx 350$ for our experimentally implemented transverse confinement and periodic potential depth.
- The shift in momentum space due to the residual longitudinal confinement of the waveguide has to be much smaller than the range of negative effective mass. In our experiment, the longitudinal frequency $\omega_x \approx 2\pi \cdot 0.5\,\text{Hz}$ limits the observation time of the soliton to $t_{\max} = 100\,\text{ms}$.

A detailed investigation of the experimental setup and the theoretical description of bright atomic gap solitons can be found in [74].

VOLUME 92, NUMBER 23 PHYSICAL REVIEW LETTERS week ending 11 JUNE 2004

Bright Bose-Einstein Gap Solitons of Atoms with Repulsive Interaction

B. Eiermann,[1] Th. Anker,[1] M. Albiez,[1] M. Taglieber,[2] P. Treutlein,[2] K.-P. Marzlin,[3] and M. K. Oberthaler[1]
[1]*Kirchhoff Institut für Physik, Universität Heidelberg, Im Neuenheimer Feld 227, 69120 Heidelberg, Germany*
[2]*Max-Planck-Institut für Quantenoptik und Sektion Physik der Ludwig-Maximilians-Universität,*
Schellingstrasse 4, 80799 München, Germany
[3]*Department of Physics and Astronomy, Quantum Information Science Group, University of Calgary,*
2500 University Drive NW, Calgary, Alberta, Canada T2N 1N4

(Received 16 December 2003; published 8 June 2004)

We report on the first experimental observation of bright matter wave solitons for ^{87}Rb atoms with repulsive atom-atom interaction. This counterintuitive situation arises inside a weak periodic potential, where anomalous dispersion can be realized at the Brillouin zone boundary. If the coherent atomic wave packet is prepared at the corresponding band edge, a bright soliton is formed inside the gap. The strength of our system is the precise control of preparation and real time manipulation, allowing the systematic investigation of gap solitons.

DOI: 10.1103/PhysRevLett.92.230401 PACS numbers: 03.75.Be, 03.75.Lm, 05.45.Yv, 05.45.–a

Nonspreading localized wave packets [1]—bright solitons—are a paradigm of nonlinear wave dynamics and are encountered in many different fields, such as physics, biology, oceanography, and telecommunication. Solitons form if the nonlinear dynamics compensates the spreading due to linear dispersion. For atomic matter waves, bright solitons have been demonstrated for which the linear spreading due to vacuum dispersion is compensated by the attractive interaction between atoms [2]. For repulsive atom-atom interaction, dark solitons have also been observed experimentally [3].

In this Letter, we report on the experimental observation of a different type of solitons, which exist only in periodic potentials—bright gap solitons. For weak periodic potentials, the formation of gap solitons has been predicted [4], while discrete solitons [5] should be observable in the case of deep periodic potentials. These phenomena are well known in the field of nonlinear photon optics where the nonlinear propagation properties in periodic refractive index structures have been studied [6]. In our experiments with interacting atoms, a new level of experimental control can be achieved, allowing for the realization of gap solitons for repulsive atom-atom interaction corresponding to a self-defocusing medium. It also opens up the way to study solitons in two- and three-dimensional atomic systems [7].

In our experiment, we investigate the evolution of a Bose-Einstein condensate in a quasi-one-dimensional waveguide with a weak periodic potential superimposed in the direction of the waveguide. In the limit of weak atom-atom interaction, the presence of the periodic potential leads to a modification of the linear propagation; i.e., dispersion [8]. It has been demonstrated that with this system anomalous dispersion can be realized [9], which is the prerequisite for the realization of gap solitons for repulsive atom-atom interaction.

Our experimental observations are shown in Fig. 1 and clearly reveal that after a propagation time of 25 ms a nonspreading wave packet is formed. The observed behavior exhibits the qualitative features of gap soliton formation such as (i) during soliton formation excessive atoms are radiated and spread out over time, (ii) solitons do not change their shape and atom number during propagation, and (iii) gap solitons do not move.

The coherent matter wave packets are generated with ^{87}Rb Bose-Einstein condensates [Fig. 2(a)]. The atoms are initially precooled in a magnetic time-orbiting

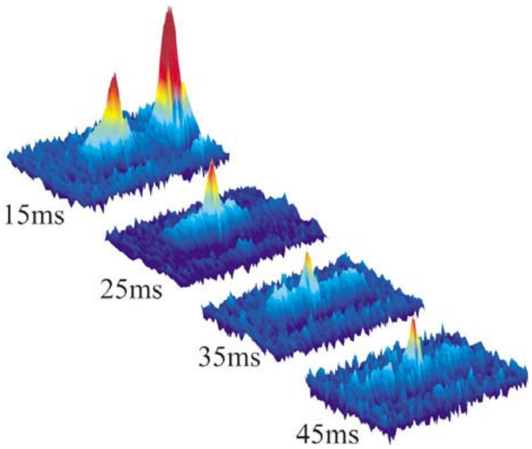

FIG. 1 (color). Observation of bright gap solitons. The atomic density in the negative mass regime deduced from absorption images (430 μm × 125 μm) averaged over four realizations is shown for different propagation times. After approximately 25 ms, a small peak is formed which does neither change in shape nor in amplitude. Excessive atoms are radiated and disperse over time. After 45 ms only the soliton with ~250 atoms has sufficient density to be clearly observable. The second peak at 15 ms shows the atoms which have been removed by Bragg scattering to generate an initial coherent wave packet consisting of ~900 atoms. For longer observation times, those atoms move out of the imaged region.

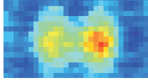

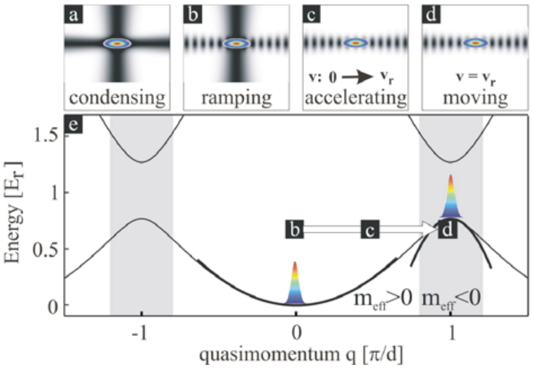

FIG. 2 (color online). Realization of coherent atomic wave packets with negative effective mass utilizing periodic potentials. (a) Top view of the crossed dipole trap geometry used for Bose-Einstein condensation. (b) A periodic potential is ramped up while the atoms are still trapped in the crossed dipole trap realizing the atomic ensemble at $q_c = 0$. (c),(d) The atoms are released into the one-dimensional waveguide and, subsequently, the periodic potential is accelerated to the recoil velocity $v_r = h/\lambda m$. This prepares the atomic wave packet at the band edge of the lowest band. (e) Normal and anomalous (shaded area) dispersion regime in a periodic potential. The single preparation steps are indicated. The shown band structure is calculated for a modulation depth of $V_0 = 1E_r$.

potential trap using the standard technique of forced evaporation leading to a phase space density of ~0.03. The atomic ensemble is subsequently adiabatically transferred into a crossed light beam dipole trap ($\lambda = 1064$ nm, $1/e^2$ waist 60 μm, 500 mW per beam), where further forced evaporation is achieved by lowering the light intensity in the trapping light beams. With this approach, we can generate pure condensates with typically 3×10^4 atoms. By further lowering the light intensity, we can reliably produce coherent wave packets of 3000 atoms. For this atom number no gap solitons have been observed. Therefore, we remove atoms by Bragg scattering [10]. This method splits the condensate coherently leaving an initial wave packet with 900(300) atoms at rest. The periodic potential $V = V_0 \sin^2(\frac{2\pi}{\lambda} x)$ of periodicity $d = \lambda/2$ is realized by a far off-resonant standing light wave of wavelength $\lambda = 783$ nm. The absolute value of the potential depth was calibrated independently by analyzing results on Bragg scattering and Landau-Zener tunneling [11].

After the creation of the coherent wave packet, we ramp-up the periodic potential adiabatically, which prepares the atomic ensemble in the normal dispersion regime at quasimomentum $q = 0$ as indicated in Fig. 2. The dispersion relation for an atom moving in a weak periodic potential exhibits a band structure as a function of quasimomentum q known from the dispersion relation of electrons in crystals [12] [see Fig. 2(e)]. Anomalous dispersion, characterized by a negative effective mass $m_{\rm eff} < 0$, can be achieved if the mean quasimomentum of the atomic ensemble is shifted to the Brillouin zone boundary corresponding to $q = \pi/d$. This is accomplished by switching off one dipole trap beam, releasing the atomic cloud into the one-dimensional horizontal waveguide [Fig. 2(c)] with transverse and longitudinal trapping frequencies $\omega_\perp = 2\pi \times 85$ Hz, and $w_{||} = 2\pi \times 0.5$ Hz. Subsequently, the atomic ensemble is prepared at quasimomentum $q = \pi/d$ by accelerating the periodic potential to the recoil velocity $v_r = h/m\lambda$. This is done by introducing an increasing frequency difference between the two laser beams, creating the optical lattice. The acceleration within 1.3 ms is adiabatic; hence, excitations to the upper bands by Landau-Zener transitions are negligible [11]. It is important to note that the strength of the dispersion is under full experimental control. The absolute value of $m_{\rm eff}(q = \pi/d) = V_0/(V_0 - 8E_r)m$ (weak potential approximation [12]) scales with the modulation depth of the periodic potential, where $E_r = (\hbar^2/2m)(\pi^2/d^2)$ is the recoil energy.

For weak periodic potentials, the full wave function of the condensate is well described by $\Psi(x,t) = A(x,t)u_0^{q_c}(x)\exp(iq_c x)$, where $u_0^{q_c}(x)\exp(iq_c x)$ represents the Bloch state in the lowest band $n = 0$ at the corresponding central quasimomentum q_c. Within the approximation of constant effective mass, the dynamics of the envelope $A(x,t)$ is governed by a one-dimensional nonlinear Schrödinger equation [13]:

$$i\hbar \frac{\partial}{\partial t} A(x,t) = \left(-\frac{\hbar^2}{2m_{\rm eff}} \frac{\partial^2}{\partial x^2} + g_{1d}|A(x,t)|^2 \right) A(x,t),$$

with $g_{1d} = 2\hbar a \omega_\perp \alpha_{nl}$, where α_{nl} is a renormalization factor due to the presence of the periodic potential ($\alpha_{nl} = 1.5$ for $q = \pi/d$ in the limit of weak periodic potentials [13]), and a is the scattering length. The stationary solution for $q_c = \pi/d$ is given by

$$A(x,t) = \sqrt{N/2x_0}\,\mathrm{sech}(x/x_0)\, e^{i\hbar t/2m_{\rm eff}x_0^2},$$

where x_0 is the soliton width and $m_{\rm eff}$ is the effective mass at the band edge. The total number of atoms constituting the soliton is given by

$$N = \frac{\hbar}{\alpha_{nl}\omega_\perp m_{\rm eff} x_0 a}. \tag{1}$$

This quantitative feature of bright solitons can also be deduced by equating the characteristic energies for dispersion $E_D = \hbar^2/m_{\rm eff}x_0^2$ and atom-atom interaction $E_{nl} = g_{1d}|A(x=0,t)|^2$.

A characteristic time scale of solitonic propagation due to the phase evolution can also be identified. In analogy to light optics, the soliton period is given by $T_S = \pi m_{\rm eff} x_0^2/2\hbar$. Solitonic propagation can be confirmed experimentally if the wave packet does not broaden over time periods much longer than T_S.

Our experimental results in Fig. 1 show the evolution of a gap soliton in the negative mass regime for different propagation times. The reproducible formation of a single soliton is observed if the initial wave packet is close to the soliton condition, i.e., a well-defined atom number for a given spatial width. The preparation scheme utilizing the Bragg pulse leads to a wave packet containing 900 atoms with a spatial size of ~2.5 μm (rms). The periodic potential depth was adjusted to $V_0 = 0.70(5)E_r$ leading to $m_{\text{eff}}/m \simeq -0.1$ at the band edge. The soliton can clearly be distinguished from the background after 25 ms, corresponding to three soliton periods. This is consistent with the typical formation time scale of few soliton periods given in nonlinear optics textbooks [14]. After 45 ms of propagation, the density of the radiated atoms drops below the level of detection and thus a pure soliton remains, which has been observed for up to 65 ms. It has been shown that for gap solitons a finite lifetime is expected due to resonant coupling to transversally excited states [15]. In order to understand the background, we numerically integrated the nonpolynomial nonlinear Schrödinger equation [16]. The calculation reveals that the nonquadratic dispersion relation in a periodic potential leads to an initial radiation of atoms. However, the absolute number of atoms in the observed background (~600 atoms) is higher than the prediction of the employed effective one-dimensional model (~250 atoms). Therefore we conclude that transverse excitations have to be taken into account to get quantitative agreement. This fact still has to be investigated in more detail.

In the following, we will discuss the experimental facts confirming the successful realization of gap solitons.

In Fig. 3(a), we compare the spreading of wave packets in the normal and anomalous dispersion regime which reveals the expected dramatic difference in wave packet dynamics. The solid circles represent the width of the gap soliton for $m_{\text{eff}}/m = -0.1$, which does not change significantly over time. We deduce a soliton width of $x_0 = 6.0(9)$ μm ($x_{\text{rms}} = 4.5$ μm) from the absorption images where the measured rms width shown in Fig. 3(a) is deconvolved with the optical resolution of 3.8 μm (rms). In this regime, the wave packet does not spread for more than eight soliton periods [$T_S = 7.7(23)$ ms]. Since our experimental setup allows one to switch from solitonic to dispersive behavior by turning the periodic potential on and off, we can directly compare the solitonic evolution to the expected spreading in the normal dispersion regime. The open circles represent the expansion of a coherent matter wave packet with 300(100) atoms in the normal mass regime $m_{\text{eff}}/m = 1$.

The preparation at the band edge implies that the group velocity of the soliton vanishes. This is confirmed in Fig. 3(b), where the relative position of the soliton with respect to the standing light wave is shown. The maximum group velocity of the lowest band is indicated by the dotted lines. In the experiment, care has to be taken to align the optical dipole trap perpendicular to the gravitational acceleration within 200 μrad. Otherwise the solitons are accelerated in the direction opposite to the gravitational force revealing their negative mass characteristic.

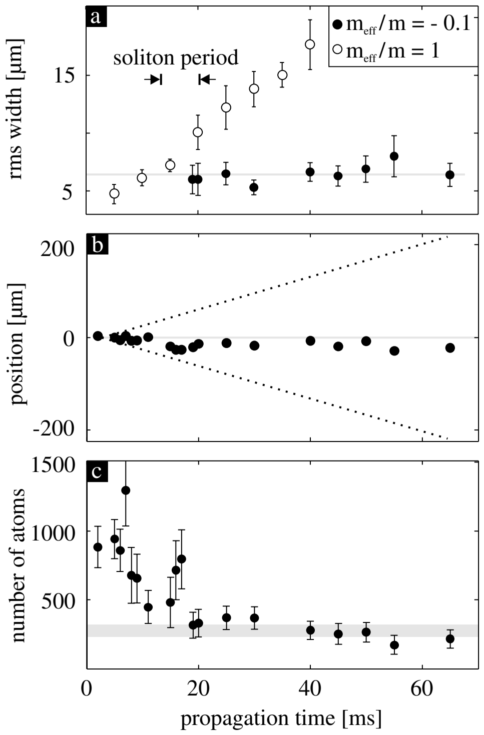

FIG. 3. Characteristic features of the observed gap soliton. (a) Comparison of expansion in the positive and the negative effective mass regime for 300 atoms. While the soliton does not disperse at all over a time of 65 ms, corresponding to more than eight soliton periods (solid circles), a wave packet in the normal mass regime expands significantly (open circles). Each point represents the result of a single realization. The solid line marks the average measured rms width of Gaussian fits to the solitons. Panel (b) shows the position of the soliton in the frame of the periodic potential and reveals that a standing gap soliton has been realized. The dotted lines indicate the positions that correspond to the maximum and the minimum group velocity in the lowest band. (c) Number of atoms in the central peak. The initial atom numbers exhibit large shot to shot fluctuations, which are reduced during the soliton formation. The predicted relation between the number of atoms and the soliton width [Eq. (1)] is indicated by the horizontal bar using the width deduced as shown in (a). Note that this comparison has been done without a free parameter since all contributing parameters are measured independently.

The calculated number of atoms [Eq. (1)] is indicated by the horizontal bar in Fig. 3(c). The width of the bar represents the expectation within our measurement uncertainties. The observed relation between atom number and width, characteristic for a bright soliton, is in excellent agreement with the simple theoretical prediction without any free parameter.

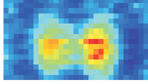

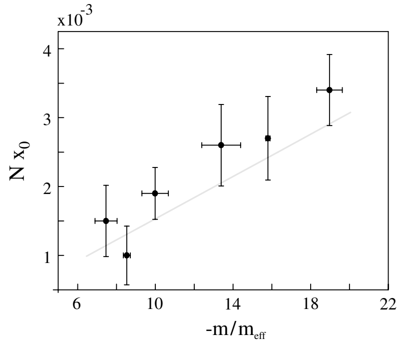

FIG. 4. Scaling properties of a gap soliton. The effective mass was varied experimentally by changing the periodic potential depth. The scaling predicted by Eq. (1) is represented by the solid line and is in good agreement with our experimental observations. The error bars represent the variation of the scaling parameter for different realizations.

As an additional check for soliton formation, we determine the product of atom number and soliton width as a function of the effective mass which is varied by adjusting the modulation depth of the periodic potential. Figure 4 shows the range of effective masses, for which solitons have been observed. For smaller values of $|m_{\mathrm{eff}}|$, corresponding to smaller potential depths, Landau-Zener tunneling does not allow a clean preparation in the negative mass regime, while for larger values the initial number of atoms differs too much from the soliton condition. The observed product of atom number and wave packet width after 40 ms of propagation are shown in Fig. 4 and confirm the behavior expected from Eq. (1). Additionally, our experimental findings reveal that the change of the scaling parameter Nx_0 in Fig. 4 is dominated by the change in the atom number, while the soliton width exhibits only a weak dependence on the effective mass.

The demonstration of gap solitons confirms that Bose condensed atoms combined with a periodic potential allow the precise control of dispersion and nonlinearity. Thus, our setup serves as a versatile new model system for nonlinear wave dynamics. Our experiments show that gap solitons can be created in a reproducible manner. This is an essential prerequisite for the study of soliton collisions. The experiment can be realized by preparing two spatially separated wave packets at the band edge and applying an expulsive potential. Ultimately, atom number squeezed states can be engineered with atomic solitons by implementing schemes analog to those developed for photon number squeezing in light optics [17]. This is interesting from a fundamental point of view and may also have impact on precision atom interferometry experiments.

We wish to thank J. Mlynek for his generous support, and Y. Kivshar, E. Ostrovskaya, A. Sizmann, and B. Brezger for many stimulating discussions. We thank O. Vogelsang and D. Weise for their donation of Ti:sapphire light. This work was supported by the Deutsche Forschungsgemeinschaft, the Emmy Noether Program, and by the European Union, Contract No. HPRN-CT-2000-00125.

[1] J. S. Russell, Report of the 14th Meeting of the British Association for the Advancement of Science, Plates XLVII–LVII (1845), pp. 311–390.
[2] L. Khaykovich *et al.*, Science **296**, 1290 (2002); K. E. Strecker, G. B. Partridge, A. G. Truscott, and R. G. Hulet, Nature (London) **417**, 150 (2002).
[3] S. Burger, K. Bongs, S. Dettmer, W. Ertmer, and K. Sengstock, Phys. Rev. Lett. **83**, 5198 (1999); J. Denschlag *et al.*, Science **287**, 97 (2000).
[4] P. Meystre, *Atom Optics* (Springer-Verlag, New York, 2001), p. 205, and references therein.
[5] A. Trombettoni and A. Smerzi, Phys. Rev. Lett. **86**, 2353 (2001).
[6] B. J. Eggleton, R. E. Slusher, C. M. deSterke, P. A. Krug, and J. E. Sipe, Phys. Rev. Lett. **76**, 1627 (1996); C. M. de Sterke and J. E. Sipe, Prog. Opt. **33**, 203 (1994); D. Neshev, A. A. Sukhorukov, B. Hanna, W. Krolikowski, and Y. Kivshar, nlin.PS/0311059.
[7] H. Saito and M. Ueda, Phys. Rev. Lett. **90**, 040403 (2003); F. Kh. Abdullaev, B. B. Baizakov, and M. Salerno, Phys. Rev. E **68**, 066605 (2003); E. A. Ostrovskaya and Yu. S. Kivshar, Phys. Rev. Lett. **90**, 160407 (2003); V. Ahufinger, A. Sanpera, P. Pedri, L. Santos, and M. Lewenstein, cond-mat/0310042.
[8] S. Burger, F. S. Cataliotti, C. Fort, F. Minardi, M. Inguscio, M. L. Chiofalo, and M. P. Tosi, Phys. Rev. Lett. **86**, 4447 (2001).
[9] B. Eiermann, P. Treutlein, Th. Anker, M. Albiez, M. Taglieber, K.-P. Marzlin, and M. K. Oberthaler, Phys. Rev. Lett. **91**, 060402 (2003).
[10] M. Kozuma, L. Deng, E.W. Hagley, J. Wen, R. Lutwak, K. Helmerson, S. L. Rolston, and W. D. Phillips, Phys. Rev. Lett. **82**, 871 (1999).
[11] B. P. Anderson and M. A. Kasevich, Science **282**, 1686 (1998); O. Morsch, J. Müller, M. Cristiani, D. Ciampini, and E. Arimondo, Phys. Rev. Lett. **87**, 140402 (2001).
[12] N. Ashcroft and N. Mermin, *Solid State Physics* (Saunders, Philadelphia, 1976).
[13] M. Steel and W. Zhang, cond-mat/9810284.
[14] G. P. Agrawal, *Applications of Nonlinear Fiber Optics* (Academic, San Diego, 2001); G. P. Agrawal, *Nonlinear Fiber Optics* (Academic, San Diego, 1995).
[15] K. M. Hilligsøe, M. K. Oberthaler, and K.-P. Marzlin, Phys. Rev. A **66**, 063605 (2002).
[16] L. Salasnich, A. Parola, and L. Reatto, Phys. Rev. A **65**, 043614 (2002).
[17] S. R. Friberg, S. Machida, M. J. Werner, A. Levanon, and T. Mukai, Phys. Rev. Lett. **77**, 3775 (1996).

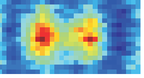

6.4 Macroscopic quantum self-trapping in periodic potentials

An experiment which is very closely related to the Josephson junction experiment is the observation of macroscopic quantum self-trapping in a one-dimensional optical lattice superimposed on a one-dimensional waveguide. This effect has been predicted by A. Trombettoni et al. [106] and is the analog of MQST in bosonic Josephson junctions.

A BEC consisting of a variable number of atoms N_T is formed in the crossed optical dipole trap and subsequently adiabatically loaded into the first energy band of a deep one-dimensional optical lattice ($V_0 \approx 11 E_{\text{rec}}$). After this preparation at zero quasimomentum, the crossed dipole trap beam is switched off, which releases the wavepacket into the one-dimensional waveguide. The subsequent expansion along the waveguide is monitored for observation times up to $t_{\text{max}} = 100\,\text{ms}$.

The tunneling dynamics of a Bose-Einstein condensate in a deep optical lattice can be theoretically modeled by a tight binding approximation, in which the total wavefunction is written as a sum of individual modes localized in the minima of the periodic potential. The neighboring modes are coupled via atomic tunneling. This description is very similar to the two-mode approximation described in chapter 3 and constitutes the generalization to an array of coupled bosonic Josephson junctions. For small atom numbers, which implies small on-site interaction energy differences between adjacent wells, Josephson tunneling can occur between the neighboring sites. This leads to a continuously expanding cloud keeping its gaussian shape. The situation changes drastically, if the total atom number is increased above a critical value $N_{\text{crit}} \approx 3000$. In this case, the wavepacket develops steep edges due to the population of quasi-momenta corresponding to infinite effective masses[3]. Those steep edges lead to a population imbalance between two adjacent wells, which is larger than the critical population imbalance $z(0)$ for macroscopic quantum self-trapping. The local effect of the inhibition of tunneling between two adjacent wells results in a stopping of the expansion of the wavepacket, which is observed in the experiment.

The transition to the macroscopically self-trapped state is characterized by a single parameter, the scaled critical on-site interaction energy Λ_c. The experimental investigation confirms, that all data points for different system parameters (i.e. atom numbers, initial width and periodic potential depth) collapse onto a single curve, which is exclusively determined by Λ_c.

A detailed investigation of self-trapping in periodic potentials will be presented in the PhD thesis of Thomas Anker.

---

[3] The broadening in momentum space during the evolution is dependent on the atom number of the BEC.

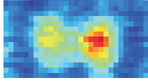

PRL **94,** 020403 (2005) PHYSICAL REVIEW LETTERS week ending 21 JANUARY 2005

Nonlinear Self-Trapping of Matter Waves in Periodic Potentials

Th. Anker,[1] M. Albiez,[1] R. Gati,[1] S. Hunsmann,[1] B. Eiermann,[1] A. Trombettoni,[2] and M. K. Oberthaler[1]
[1]*Kirchhoff Institut für Physik, Universität Heidelberg, Im Neuenheimer Feld 227, 69120 Heidelberg, Germany*
[2]*I.N.F.M. and Dipartimento di Fisica, Universitá di Parma, parco Area delle Scienze 7A, I-43100 Parma, Italy*

(Received 1 October 2004; published 19 January 2005)

We report the first experimental observation of nonlinear self-trapping of Bose-condensed ^{87}Rb atoms in a one-dimensional waveguide with a superimposed deep periodic potential . The trapping effect is confirmed directly by imaging the atomic spatial distribution. Increasing the nonlinearity we move the system from the diffusive regime, characterized by an expansion of the condensate, to the nonlinearity dominated self-trapping regime, where the initial expansion stops and the width remains finite. The data are in quantitative agreement with the solutions of the corresponding discrete nonlinear equation. Our results reveal that the effect of nonlinear self-trapping is of local nature, and is closely related to the macroscopic self-trapping phenomenon already predicted for double-well systems.

DOI: 10.1103/PhysRevLett.94.020403 PACS numbers: 03.75.Lm

The understanding of coherent transport of waves is essential for many different fields in physics. In contrast to the dynamics of noninteracting waves, which is conceptually simple, the situation can become extremely complex as soon as interaction between the waves is of relevance. Very intriguing and counterintuitive transport phenomena arise in the presence of a periodic potential. This is mainly due to the existence of spatially localized stationary solutions.

In the following we will investigate the dynamics of Bose-condensed ^{87}Rb atoms in a deep one-dimensional periodic potential; i.e., the matter waves are spatially localized in each potential minimum (tight binding) and are coupled via tunneling to their next neighbors. This system is described as an array of coupled boson Josephson junctions [1]. The presence of nonlinearity drastically changes the tunneling dynamics [2] leading to new localization phenomena on a macroscopic scale such as discrete solitons, i.e., coherent nonspreading wave packets, and nonlinear self-trapping [3]. These phenomena have also been studied in the field of nonlinear photon optics where a periodic refractive index structure leads to an array of wave guides, which are coupled via evanescent waves [4].

In this Letter we report on the first experimental confirmation of the theoretically predicted effect of nonlinear self-trapping of matter waves in a periodic potential [3]. This effect describes the drastic change of the dynamics of an expanding wave packet when the nonlinearity, i.e., repulsive interaction energy, is increased above a critical value. Here the counterintuitive situation arises that although the spreading is expected to become faster due to the higher nonlinear pressure, the wave packet *stops* to expand after a short initial diffusive expansion. Since we observe the dynamics in real space, we can directly measure the wave packet width for different propagation times. In Fig. 1 we show the experimental signature of the transition from the diffusive to the self-trapping regime. We prepare wave packets in a periodic potential and change only the nonlinear energy by adjusting the number of atoms in the wave packet close to (2000 ± 200 atoms) and above (5000 ± 600 atoms) the critical value. Clearly both wave packets expand initially. At $t \sim 35$ ms the wave packet with higher initial atomic density has developed steep edges and stops expanding (see inset in Fig. 1). In contrast, the wave packet with the lower initial atomic density continues to expand keeping its Gaussian shape.

The coherent matter-wave packets are generated with ^{87}Rb Bose-Einstein condensates realized in a crossed light beam dipole trap ($\lambda = 1064$ nm, $1/e^2$ waist 55 μm, 600 mW per beam). Subsequently a periodic dipole poten-

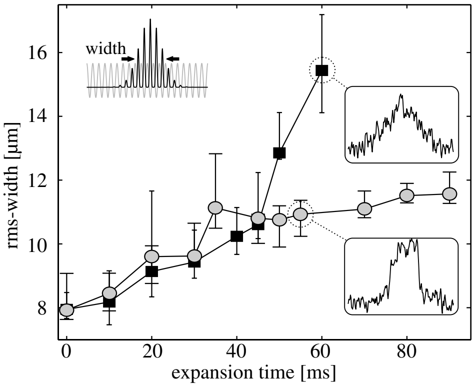

FIG. 1. Observation of nonlinear self-trapping of Bose-condensed ^{87}Rb atoms. The dynamics of the wave packet width along the periodic potential is shown for two different initial atom numbers. By increasing the number of atoms from 2000 ± 200 (squares) to 5000 ± 600 (circles), the repulsive atom-atom interaction leads to the stopping of the global expansion of the wave packet. The insets show that the wave packet remains almost Gaussian in the diffusive regime but develops steep edges in the self-trapping regime. These edges act as boundaries for the complex dynamics inside.

tial $V_p = sE_r \sin^2(kx)$, realized with a far off-resonant standing light wave ($\lambda = 783$ nm) collinear with one of the dipole trap beams is adiabatically ramped up. The depth of the potential is proportional to the intensity of the light wave and is given in recoil energies $E_r = \frac{\hbar^2 k^2}{2m}$ with the wave vector $k = 2\pi/\lambda$. By switching off the dipole trap beam perpendicular to the periodic potential, the atomic matter wave is released into a trap acting as a one-dimensional waveguide $V_{\mathrm{dip}} = \frac{m}{2}(\omega_\perp^2 r^2 + \omega_\parallel^2 x^2)$ with radial trapping frequency $\omega_\perp = 2\pi \times 230$ Hz and longitudinal trapping frequency $\omega_\parallel \approx 2\pi \times 1$ Hz. The wave packet evolution inside the combined potential of the waveguide and the lattice is studied by taking absorption images of the atomic density distribution after a variable time delay. The density profiles $n(x, t)$ along the waveguide are obtained by integrating the absorption images over the radial dimensions and allow the detailed investigation of the wave packet shape dynamics with a spatial resolution of 3 μm.

In Fig. 2 the measured temporal evolution of the wave packet prepared in the self-trapping regime ($s = 10, 7.6(5)$ μm initial rms width, 5000 ± 600 atoms) is shown. The evolution of the shape is divided into two characteristic time intervals. Initially ($t < 20$ ms) the wave packet expands and develops steep edges. This dynamics can be understood in a simple way by considering that the repulsive interaction leads to a broadening of the momentum distribution and thus to a spreading in real space. Since the matter waves propagate in a periodic potential, the evolution is governed by the modified dispersion (i.e., band structure) $E(q) = -2K \cos(dq)$ where $d = \lambda/2$ is the lattice spacing, $\hbar q$ is the quasimomentum, and K is the characteristic energy associated with the tunneling. The formation of steep edges is a consequence of the population of higher quasimomenta around $q = \pm\pi/2d$ where the dispersion is strongly reduced and the group velocity is extremal. In order to populate quasimomenta $|q| > \pi/2d$ the initial interaction energy has to be higher than the characteristic tunneling energy K and thus the critical parameter depends on the ratio between the on-site interaction energy and the tunneling energy as we will discuss in detail. While in the linear evolution the steep edges move with the extremal group velocity [5], in the experiment reported here they stop after their formation. As we will show, this is a consequence of the high atomic density gradient at the edge which suppresses tunneling between neighboring wells. The further evolution is characterized by stationary edges acting as boundaries for the complex internal behavior of the wave packet shape. The formation of the side peaks is an indication that atoms moving outwards are piled up because they cannot pass the steep edge. Finally the pronounced features of the wave packet shape disappear and a square shaped density distribution is formed.

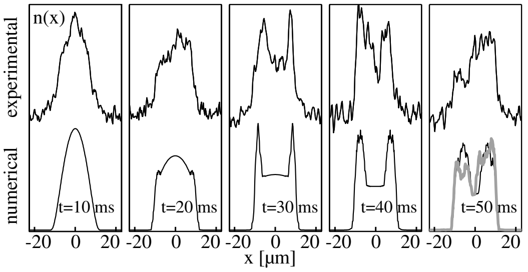

FIG. 2. Comparison between theory and experiment for $s = 10, 7.6(5)$ μm initial rms width and 5000 ± 600 atoms. The upper graphs show the measured density distribution for different propagation times. During the initial expansion in the self-trapping regime the wave packet develops steep edges which act as stationary boundaries for the subsequent internal dynamics. The results of the numerical integration of Eq. (2) (depicted in the lower graphs) are in very good agreement. For $t = 50$ ms a 1.5 mrad deviation of the waveguides' horizontal orientation (consistent with the experimental uncertainty) is taken into account and reproduces the experimentally observed asymmetry (gray line).

In order to understand in detail the ongoing complex self-trapping dynamics we compare quantitatively our experimental findings with numerically obtained solutions (see Fig. 2). For our typical experimental parameters of $s \sim 11$ and $\sim$100 atoms per well, we are in the regime where the dynamics can be described by a macroscopic wave function $\Psi(\vec{r}, t)$ and thus by the Gross-Pitaevski equation [6]. Since we use deep optical lattices, the description can be reduced to a one-dimensional discrete nonlinear equation, which includes the fundamental processes, namely, tunneling between the wells and nonlinear phase evolution due to the interaction of the atoms [3,7]. In our experiment the trapping frequency in a single well along the lattice period is on the order of $\omega_x \approx 2\pi \times 25$ kHz, whereas the transverse trapping frequency of the waveguide is $\omega_\perp = 2\pi \times 230$ Hz. Thus our system can be described as a horizontal pile of pancakes, and the transverse degree of freedom cannot be neglected. In [7] a one-dimensional discrete nonlinear equation (DNL) is derived which takes into account the adiabatic change of the wave function in the transverse direction due to the atom-atom interaction. A generalized tight binding ansatz

$$\Psi(\vec{r}, t) = \sum_j \psi_j(t) \Phi_j[\vec{r}, N_j(t)] \tag{1}$$

is used, with $\psi_j(t) = \sqrt{N_j(t)} e^{i\phi_j(t)}$, where $N_j(t)$ is the atom number and $\phi_j(t)$ is the phase of the jth condensate. Φ_j is normalized to 1 (i.e., $\int d\vec{r} \Phi_j^2 = 1$) and $\Psi(\vec{r}, t)$ is normalized to the total number of atoms N_T (i.e., $\sum_j |\psi_j|^2 = N_T$). The spatial real wave function $\Phi_j[\vec{r}, N_j(t)]$ is centered at the minimum of the jth well and is time dependent through $N(t)$. Integrating over the spatial degrees of freedom, the

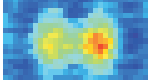

following DNL is obtained from the Gross-Pitaevski equation

$$i\hbar\frac{\partial\psi_j}{\partial t} = \epsilon_j\psi_j - K(\psi_{j+1} + \psi_{j-1}) + \mu_j^{\mathrm{loc}}\psi_j. \qquad (2)$$

K is the characteristic tunneling energy between adjacent sites. $\epsilon_j = \int d\vec{r}\frac{m}{2}\omega_{\|}^2x^2\Phi_j^2$ is the on-site energy resulting from the longitudinal trapping potential, which is negligible in the description of our experiment. The relevant chemical potential is given by $\mu_j^{\mathrm{loc}} = \int d\vec{r}[\frac{m}{2}\omega_{\perp}^2r^2\Phi_j^2 + g_0|\psi_j(t)|^2\Phi_j^4]$ with $g_0 = 4\pi\hbar^2a/m$ (a is the scattering length). It can be calculated approximately for our experimental situation assuming a parabolic shape in transverse direction (Thomas-Fermi approximation) and a Gaussian shape in longitudinal direction for $\Phi_j[\vec{r}, N_j(t)]$ ($\omega_x \gg \mu_j^{\mathrm{loc}}/\hbar > \omega_{\perp}$). This leads to $\mu_j^{\mathrm{loc}} = U_1|\psi_j(t)|$ with

$$U_1 = \sqrt{\frac{m\omega_{\perp}^2g_0}{\sqrt{2\pi}\pi\sigma_x}}. \qquad (3)$$

Here $\sigma_x = \lambda/(2\pi s^{1/4})$ is the longitudinal Gaussian width of Φ_j in harmonic approximation of the periodic potential minima. Please note that if the local wave function Φ_j does not depend on N_j Eq. (2) reduces to the well known discrete nonlinear Schrödinger equation with $\mu_j^{\mathrm{loc}} \propto N_j$ [3,8].

We compare the experimental and numerical results in Fig. 2 and find very good agreement. The theory reproduces the observed features such as steepening of the edges, the formation of the side peaks, and the final square wave packet shape. It is important to note that all parameters entering the theory (initial width, atom number, periodic potential depth, and transverse trapping frequency) have been measured independently. The observed asymmetry of the wave packet shapes (e.g., see Fig. 2, $t = 50$ ms) appears due to the deviation from the perfect horizontal orientation of the wave guide (± 2 mrad) which results from small changes in height of the pneumatic isolators of the optical table during the measurements.

In the following we will use the numerical results to get further insight into the self-trapping dynamics. We investigate the local tunneling dynamics and phase evolution by evaluating the relative atom number difference $\Delta N_j = (N_{j+1} - N_j)/(N_{j+1} + N_j)$ and the phase difference $\Delta\phi_j = \phi_{j+1} - \phi_j$ between two neighboring sites. In Fig. 3(a) the wave packet shapes for $t = 0$ and $t = 50$ ms are shown. In Fig. 3(b) we plot the relative atom number difference ΔN_j averaged over the whole propagation duration of 50 ms. The graph indicates two spatial regions with different characteristic dynamics. While the average vanishes in the central region (shaded in light gray) it has significant amplitude in the edge region (shaded in dark gray). The characteristic dynamics of ΔN_j and $\Delta\phi_j$ in the central region is depicted in Fig. 3(c). The atom number difference as well as the phase difference oscillate around zero. This behavior is known in the context of Bose-Einstein condensation in double-well potentials. It is described as the boson Josephson junction "zero-phase mode" [2] and is characteristic for superfluid tunneling dynamics if the atom number difference stays below a critical value. At the edge in contrast, ΔN_j crosses the critical value during the initial expansion (steep density edge) and locks for long time periods to high absolute values showing that the tunneling and thus the transport is inhibited. At the same time the phase difference winds up. This characteristic dynamics has been predicted within the boson Josephson junction model for a double-well system and is referred to as the "running phase self-trapping mode" [2]. This analysis makes clear that the effect of nonlinear self-trapping as observed in our experiment is a *local* effect and is closely related to boson Josephson junctions dynamics in a double-well system.

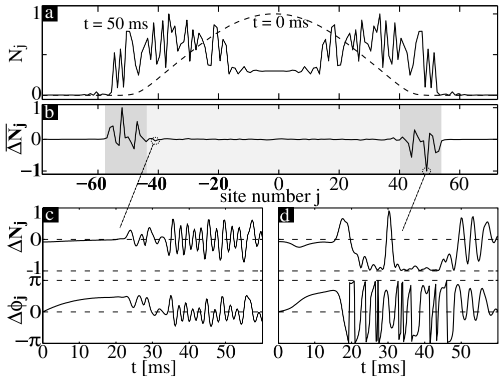

FIG. 3. A numerical investigation of the site-to-site tunneling dynamics. (a) The atomic distribution N_j of the wave packet for $t = 0$ and 50 ms. (b) The relative population difference ΔN_j time averaged over the expansion time indicates two regions with different dynamics. (c) The dynamics of ΔN_j and the phase difference $\Delta\phi_j$ for the marked site oscillate around zero known as the zero-phase mode of the boson Josephson junction. (d) The dynamics in the edge region is characterized by long time periods where $|\Delta N_j|$ is close to 1 while at the same time $\Delta\phi_j$ winds up very quickly (phase is plotted modulo π) known as "running phase self-trapping mode" in boson Josephson junctions. Thus the expansion of the wave packet is stopped due to the inhibited site-to-site tunneling at the edge of the wave packet.

Although the local dynamics just described is very complex, the evolution of the root mean square width of the wave packet, i.e., the global dynamics, can be predicted analytically within a very simple model. In [3], a Gaussian profile wave packet $\psi_j(t) \propto \exp[-(\frac{j}{\gamma(t)})^2 + i\frac{\delta(t)}{2}j^2]$, parametrized by the width $\gamma(t)$ (in lattice units) and the quadratic spatial phase $\delta(t)$, is used as an ansatz for quasimomentum $q = 0$ to solve the discrete nonlinear Schrödinger equation. The time evolution of the width

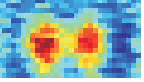

$\gamma(t)$ is obtained analytically applying a variational principle. The result of this simple model is that the dynamics of the wave packet width is solely determined by two global parameters—the density of the atoms and the depth of the periodic potential. Also, a critical parameter Λ/Λ_c can be deduced, which governs the transition from the diffusive to the self-trapping regime. The transition parameter Λ/Λ_c for the 2D case described by Eq. (2) is obtained following the same lines of calculation as in [3]. Assuming that the initial width $\gamma_0 \gg 1$ (in the experiment typically $\gamma_0 \approx 40$) we obtain

$$\Lambda = \frac{U_1\sqrt{N_T}}{2K} \quad \text{and} \quad \Lambda_c = \frac{3}{2}\left(\frac{9\pi}{8}\right)^{1/4}\sqrt{\gamma_0}.$$

A surprising result of this model is the prediction of the following scaling behavior (shown in Fig. 4):

$$\frac{\gamma_0}{\gamma_\infty} = \sqrt{1 - \frac{\Lambda_c}{\Lambda}} \tag{4}$$

for $\Lambda/\Lambda_c > 1$, where γ_∞ is the width of the wave packet for $t \longrightarrow \infty$. For $\Lambda/\Lambda_c < 1$ the width is not bound and thus the system is in the diffusive regime. In the regime $\Lambda/\Lambda_c > 1$ the width is constant after an initial expansion (see inset Fig. 4). Since $\Lambda/\Lambda_c \propto \mu_{av}^{\mathrm{loc}}/K$, the self-trapping regime is reached by either reducing the initial width, increasing the height of the periodic potential, or, as is shown in Fig. 1, by increasing the number of atoms.

Scaling means that all data points (i.e., different experimental settings with the same Λ/Λ_c) collapse onto a single universal curve. In order to confirm the scaling behavior experimentally we measure the width of the wave packet after 50 ms evolution for different system parameters, i.e., atom number, initial width of the wave packet, and depth of the periodic potential. The experimental results shown in Fig. 4 confirm the universal scaling dependence on Λ/Λ_c and follow qualitatively the prediction of the simple model. The dashed line in Fig. 4 is the result of the numerical integration of the discrete nonlinear equation given in Eq. (2) evaluated at $t = 50$ ms. It shows quantitative agreement with the experiment. The difference between the numerical (dashed line) and analytical calculation (solid line) is due to the initial non-Gaussian shape (numerically obtained ground state) and the strong deviation from the Gaussian shape for long propagation times.

Concluding, we have demonstrated for the first time the predicted effect of nonlinear self-trapping of Bose-Einstein condensates in deep periodic potentials. The detailed analysis shows that this is a *local* effect, which occurs due to nonlinearity induced inhibition of site-to-site tunneling at the edge of the wave packet. This behavior is closely connected to the phenomenon of macroscopic self-trapping known in the context of double-well systems. Furthermore, we quantitatively confirm in our experiments the predicted critical parameter which discriminates between diffusive and self-trapping behavior.

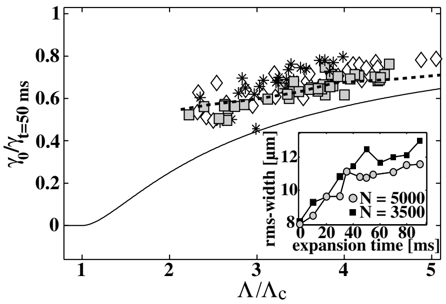

FIG. 4. Experimental investigation of the scaling behavior. The solid line shows the curve given by Eq. (4). Experimentally the parameter Λ/Λ_c was varied by using three different periodic potential depths: $s = 10.6(3)$ (stars), 11.1(3) (squares), and 11.5(3) (diamonds). For each potential depth, wave packets with different atom numbers and initial widths are prepared and the width for $t = 50$ ms is determined. The experimental data show qualitatively the scaling behavior predicted by Eq. (4) and are in quantitative agreement with the results of the numerical integration of the DNL (dashed line). The inset depicts the nature of the scaling: increasing Λ/Λ_c (by, e.g., increasing the atom number) leads to a faster trapping and thus to a smaller final width.

We wish to thank A. Smerzi for very stimulating discussions. This work was supported by the Deutsche Forschungsgemeinschaft, Emmy Noether Programm, and by the European Union, RTN-Cold Quantum Gases, Contract No. HPRN-CT-2000-00125.

[1] F.S. Cataliotti, S. Burger, C. Fort, P. Maddaloni, F. Minardi, A. Trombettoni, A. Smerzi, and M. Inguscio, Science **293**, 843 (2001).

[2] A. Smerzi, S. Fantoni, S. Giovanazzi, and S.R. Shenoy, Phys. Rev. Lett. **79**, 4950 (1997); S. Raghavan, A. Smerzi, S. Fantoni, and S.R. Shenoy, Phys. Rev. A **59**, 620 (1999); G.J. Milburn, J. Corney, E.M. Wright, and D.F. Walls, Phys. Rev. A **55**, 4318 (1997).

[3] A. Trombettoni and A. Smerzi, Phys. Rev. Lett. **86**, 2353 (2001).

[4] For example, D.N. Christodoulides, F. Lederer, and Y. Silberberg, Nature (London) **424**, 817 (2003).

[5] B. Eiermann, P. Treutlein, Th. Anker, M. Albiez, M. Taglieber, K.-P. Marzlin, and M.K. Oberthaler, Phys. Rev. Lett. **91**, 060402 (2003).

[6] W. Zwerger, J. Opt. B **5**, S9 (2003).

[7] A. Smerzi and A. Trombettoni, Phys. Rev. A **68**, 023613 (2003).

[8] D. Hennig and G.P. Tsironis, Phys. Rep. **307**, 333 (1999); P.G. Kevrekidis, K.O. Rasmussen, and A.R. Bishop, Int. J. Mod. Phys. B **15**, 2833 (2001); M. Johansson and S. Aubry, Nonlinearity **10**, 1151 (1997).

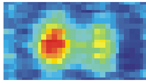

7 Conclusion and outlook

7.1 Conclusion

This thesis describes experiments on nonlinear dynamics of ^{87}Rb Bose-Einstein condensates in multi well and double well potentials. Hereby, I focus on the realization of the first single Josephson junction for BECs.

Experimental results on BECs in periodic potentials

During the first two years of my PhD period at the University of Konstanz, we investigated the dynamics of BECs in weak one-dimensional periodic potentials oriented along a one-dimensional optical waveguide. The first experiments were concerned with the implementation of "dispersion management" for atomic matter waves [23, 24]. This concept, which is known from photon optics, allows to control the sign as well as the magnitude of the dispersion of BECs in a periodic potential. The periodic potential for matter waves is created by a pair of counter-propagating off-resonant laser beams forming a standing light wave. By detuning the frequencies of the two beams, which results in a moving periodic potential, the BEC can be prepared at any position in quasimomentum space. This allows for an adjustment of negative effective masses, which is a prerequisite for the generation of bright gap solitons of atoms with repulsive interaction. Those non-spreading wavepackets which we have subsequently observed [16] form, if the nonlinear atom-atom interaction and the anomalous dispersion cancel.

After moving to the University of Heidelberg, we addressed investigation of Josephson junction arrays for Bose-Einstein condensates. They are experimentally implemented by a deep standing light wave superimposed on a two-dimensional harmonic confinement. The nonlinear dynamics in this system can be theoretically described in the framework of the tight-binding approximation [106], in which nearest neighbours are coupled via interwell tunneling. Two distinct dynamical regimes are theoretically predicted and could be experimentally observed [27]. For small atom numbers, the atomic cloud expands infinitely after turning off the harmonic trapping potential along the optical lattice. A totally different and counterintuitive situation arises if the atom number is increased above a critical value. In this case, the expansion of the wavepacket stops after a short evolution time. This effect, which is caused by the atom-atom interaction is referred to as "macroscopic quantum self-trapping".

Josephson junctions for BECs

A Josephson junction generally consists of two weakly linked macroscopic wavefunctions separated by an energy barrier. A weak link between two Bose-Einstein condensates is provided by an external double well potential. The tunneling dynamics in this new experimental system constitutes the nonlinear generalization of the well-known Josephson tunneling in superconductors and superfluids.

A simple and intuitive theoretical description in terms of only two physical quantities - population imbalance and relative phase between the two wells - is provided in the framework of the two-mode approximation [29], where the tunneling dynamics is mapped onto the motion of a nonrigid pendulum[1]. In this analogy, the relative phase corresponds to the angle and the population imbalance to the angular momentum of the pendulum. For small initial population imbalances of the wells, the atoms tunnel left and right over time, corresponding to an oscillatory motion of the pendulum around the stable equilibrium position. If the initial population is chosen above a critical value, resonant tunneling between the two wells is inhibited because the difference of the interaction energy between the two localized modes exceeds the tunneling energy splitting. In this case, the population imbalance becomes self-locked and the relative phase winds up linearly over time.

Experimental setup for the observation of Josephson tunneling dynamics

The experimental apparatus to reach the quantum degenerate regime is based on standard cooling methods. After loading a laser-cooled atomic sample into a time orbiting potential magnetic trap, a first stage of forced evaporative cooling to a phase space density of $\Omega \approx 5 \cdot 10^{-3}$ is performed. Bose-Einstein condensation is subsequently reached by evaporative cooling in a three-dimensional optical dipole trap created by two crossed off-resonant laser beams. A BEC consisting of approximately 1000 atoms is prepared in an effective double well potential by adiabatically ramping up a one-dimensional standing light wave, which is created by two beams crossing at a relative angle of 9°. This optical lattice has a periodicity of $5.18\,\mu$m and a potential depth which is adjustable by controlling the beam intensities. The resulting double well potential has a well-spacing of $d = 4.4\,\mu$m and a typical potential barrier height of $V_b = h \cdot 260$ Hz. The realization of such small lattice spacings below $10\,\mu$m and atom numbers below 3000 atoms is necessary in order to make both dynamical regimes experimentally accessible.

A relative shift of the harmonic confinement with respect to the optical lattice is used to create an asymmetric double well potential. The degree of asymmetry defines the initial population imbalance between left and right well. A relative position shift of only 350 nm results in a population imbalance corresponding to the self-trapping threshold. In order to be able to clearly experimentally distinguish between Josephson tunneling and self-trapping regime, a relative position stability of below 100 nm is required. This demands high passive stability of the mechanical setup and requires an active stabilization of the phase of the optical lattice. After the preparation, the Josephson tunneling dynamics is initiated by non-adiabatically switching to a symmetric double well potential.

---

[1] The tunneling dynamics of superconducting Josephson junctions can be mapped onto the dynamics of a rigid pendulum in the framework of the RCSJ model [43].

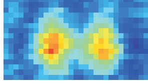

Experimental results on Josephson dynamics

The experimental results show, that both dynamical regimes - Josephson oscillations and self-trapping - are experimentally accessible. In order to completely characterize the ongoing dynamics, the population imbalance as well as the relative phase is determined as a function of the evolution time in the symmetric double well potential. The population imbalance is obtained from absorption images, which are taken after increasing the distance of the two atomic clouds by exciting a collective dipole oscillation inside the individual wells. The high optical resolution $2.7(2)\,\mu$m of our imaging system allows to clearly distinguish the two wavepackets. This allows for a direct in-situ observation of tunneling massive particles for the first time.

The relative phase of the two modes is obtained by releasing the BEC from the double well potential. After time-of-flight, clear atomic double slit interference patterns form unveiling the relative phase of the wavepackets. The knowledge of both dynamical variables allows to determine the complete phase plane trajectories in the different tunneling regimes.

We observe Josephson oscillations for an initial population imbalance $z(0) = 0.28(6)$, which means that 64% of the atoms are initially localized in the left well. This regime is characterized by an oscillating population imbalance and a relative phase around a zero mean value. The observed tunneling timescale of 40(2) ms is much shorter than the tunneling period 500(50) ms expected for non-interacting atoms in the realized potential. This reveals the important role of nonlinear atom-atom interaction in bosonic Josephson junction experiments. The experimental results are in excellent agreement with the numerical solution of the non-polynomial nonlinear Schrödinger equation [73]. It is important to note, that all parameters entering the simulation have been independently calibrated.

At an initial population imbalance of $z(0) = 0.62(6)$ the system evolves in the self-trapped regime. Here, the population is stationary within the experimental errors and the relative phase evolves unbound in time (running phase modes).

The transition between the two regimes is in agreement with the prediction of the numerical solution of the nonlinear non-polynomial Schrödinger equation, which predicts a critical population imbalance[2] $z_{c,NPSE} = 0.375$. However, the two-mode approximation predicts the transition at $z_{c,CTM} = 0.23$, which is inconsistent with the experimental findings. Therefore, recently an extended two-model has been developed [80], which is capable to explain our experimental data quantitatively.

The experimental results on Josephson junctions for Bose-Einstein condensates have been published in Physical Review Letters [100].

7.2 Outlook

The preparation of Bose-Einstein condensates in the groundstate of an external double well potential implies a zero initial phase difference between the two localized modes. Therefore, π-oscillations [30], which are tunneling oscillations around the mean value $\langle\phi\rangle_t = \pi$ of the relative phase, are so far inaccessible experimentally. We are currently setting up an experimental system, which allows to imprint an arbitrary phase on one of

---

[2] The full solution of the three dimensional Gross-Pitaevskii equation yields $z_{c,TDGPE} = 0.39$.

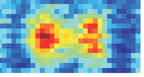

the two modes with a spatial resolution of below $2\,\mu$m . The details of the experimental implementation will be presented in the diploma thesis of Jonas Fölling.

The experimental results show, that self-trapped states decay to the symmetrically populated state with a timescale of approximately 300 ms. This decay is most likely due to the influence of the residual thermal cloud and should allow for a determination of the temperature of the atomic sample. However, this implies a solution of the Gross-Pitaevskii equation for a BEC in the double well potential taking into account of a coupling to the thermal bath, which has not been implemented so far. We are currently investigating the effect of thermal and quantum decoherence on the fluctuations of the relative phase. The visibility $\alpha = \langle \cos\phi \rangle$ of the relative phase is measured as a function of the barrier height. Thermal effects have been shown to significantly affect the transition from the coherent to the incoherent regime even at temperatures far below the critical temperature [101]. This should provide a new thermometry method especially for small BECs. The preliminary results suggest, that the lowest achievable temperatures in our setup are approximately 10 nK, which has to be compared to the critical temperature $T_C \approx 55\,$nK. This would imply that the thermal cloud consists of only about 10 atoms.

Furthermore, our experimental setup could be used to study the tunneling dynamics of a BEC in a double well potential with an oscillating energy barrier. It has been shown by Luca Salasnich [107], that the dynamics of this system critically depends on the driving frequency ω of the oscillating barrier[3]. In the regime of macroscopic self-trapping, where only a small fraction of the atoms tunnels with a frequency ω_J, the dynamics is strongly affected at the parametric resonance condition $\omega = 2\omega_J$. At a sufficiently large perturbation, the system eventually escapes from the self-trapped state. The oscillating barrier can easily be implemented in the current setup by simply periodically varying the height of the potential barrier.

Most of the experiments with Bose-Einstein condensates performed so far can be well described by the Gross-Pitaevskii equation. However, the ground state of a BEC of repulsive atoms in a double well potential of a specific shape has been found to be fragmented, meaning that at least two natural orthogonal orbitals are macroscopically occupied [108, 109]. Therefore, Bose-Einstein condensates of low atom numbers in double well systems can provide a test of the validity of the mean-field description, which assumes a single macroscopically occupied wavefunction.

Furthermore, the combination of a double well potential and an additional one-dimensional optical lattice should allow for the creation of two independent atomic gap-solitons. By applying an additional harmonic external potential, it should be possible to investigate soliton collisions in a very reproducible way. A detailed investigation of this possible future experiment can be found in the diploma thesis of M. Taglieber [110].

During the last years, Bose-Einstein condensates in double well potentials have attracted enormous theoretical and experimental interest. The first experimental implementation presented in this thesis brings the observation of many of the predicted effects into reach. Therefore, one can be anxious to future publications.

---

[3] The time-dependency is modeled by a time-dependent scaled on-site interaction energy Λ.

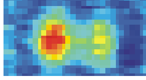

Bibliography

[1] B.D. Josephson. Possible new effects in superconductive tunneling. *Physics Letters*, 1:251–253, 1962.

[2] P.L. Anderson and J.W. Rowell. Probable observation of the Josephson superconducting tunnel effect. *Physical Review Letters*, 10:230, 1963.

[3] A. Barone and P. Paterno. *Physics and Applications of the Josephson Effect.* Whiley and Sons, New York, 1982.

[4] S. Backhaus, S. Pereverzev, A. Loshak, J. C. Davis, and R. E. Packard. Direct measurement of the current-phase relation of a superfluid ^{3}He-b weak link. *Science*, 278:1435, 1997.

[5] S.N. Bose. Plancks Gesetz und Lichtquantenhypothese. *Z.Phys.*, 26(6):178–81, 1924.

[6] A. Einstein. Quantentheorie des einatomigen idealen Gases: Zweite Abhandlung. *Sitzungsber. Preuss. Akad. Wiss.*, page 18ff., 1925.

[7] M. Anderson, J. Ensher, M. Matthews, C. Wieman, and E. Cornell. Observation of Bose-Einstein condensation in a dilute atomic vapor. *Science*, 269:198, 1995.

[8] K. Davis, M.-O. Mewes, M. Andrews, N. van Druten, N. Durfee, D. Kurn, and W. Ketterle. Bose-Einstein condensation in a gas of sodium atoms. *Physical Review Letters*, 75:3969, 1995.

[9] C.C. Bradley, C.A. Sackett, J.J. Tollet, and R.G. Hulet. Evidence of Bose-Einstein condensation in an atomic gas with attractive interactions. *Physical Review Letters*, 75:1687, 1995.

[10] M.R. Andrews, C.G. Townsend, H.-J. Miesner, D.S. Durfee, D.M. Kurn, and W. Ketterle. Observation of interference between two Bose-Einstein condensates. *Science*, 275:637, 1997.

[11] Nature insight: Ultracold matter. *Nature*, 416:6877, 2002.

[12] I. Bloch, T.W. Hänsch, and T. Esslinger. Atom laser with a cw output coupler. *Physical Review Letters*, 82(15):3008–11, 1999.

[13] S. Burger, K. Bongs, S. Dettmer, W. Ertmer, K. Sengstock, A. Sanpera, G.V. Shlyapnikov, and M. Lewenstein. Dark solitons in Bose-Einstein condensates. *Physical Review Letters*, 83(25):5198–5201, 1999.

[14] K.E. Strecker, G.B. Partridge, A.G. Truscott, and R.G. Hulet. Formation and propagation of matter wave soliton trains. *Nature*, 417:150–153, 2002.

[15] L. Khaykovich, F. Schreck, F. Ferrari, T. Bourdel, J. Cubizolles, L.D. Carr, Y. Castin, and C. Salomon. Formation of a matter wave bright soliton. *Science*, 296:1290–93, 2002.

[16] B. Eiermann, T. Anker, M. Albiez, M. Taglieber, P. Treutlein, K.-P. Marzlin, and M. K. Oberthaler. Bright Bose Einstein gap solitons of atoms with repulsive interaction. *Physical Review Letters*, 92:230401, 2004.

[17] K.W. Madison, F. Chevy, W. Wohlleben, and J. Dalibard. Vortices in a stirred Bose-Einstein condensate. *Journal of modern optics*, 47(14/15):2715–23, 2000.

[18] M. Ben Dahan, E. Peik, J. Reichel, Y. Castin, and C. Salomon. Bloch oscillations of atoms in an optical potential. *Physical Review Letters*, 76(24):4508–11, 1996.

[19] S.R. Wilkinson, C.F. Bharucha, K.W. Madison, Q. Niu, and M.G. Raizen. Observation of atomic Wannier-Stark ladders in an accelerating optical potential. *Physical Review Letters*, 76(24):4512–15, 1996.

[20] M. Kozuma, L. Deng, E.W. Hagley, J. Wen, R. Lutwak, K. Helmerson, S.L. Rolston, and W.D. Phillips. Coherent splitting of Bose-Einstein condensed atoms with optically induced Bragg diffraction. *Physical Review Letters*, 82(5):871–75, 1999.

[21] C.F. Bharucha, K.W. Madison, P.R. Morrow, S.R. Wilkinson, B. Sundaram, and M.G. Raizen. Observation of atomic tunneling from an accelerating optical potential. *Physical Review A*, 55(2):R857–60, 1997.

[22] B.P. Anderson and M. Kasevich. Macroscopic quantum interference from atomic tunnel arrays. *Science*, 282:1686–89, 1998.

[23] B. Eiermann, P. Treutlein, Th. Anker, M. Albiez, M. Taglieber, K.-P. Marzlin, and M.K. Oberthaler. Dispersion management for atomic matter waves. *Physical Review Letters*, 91(6):060402, 2003.

[24] Th. Anker, M. Albiez, B. Eiermann, M. Taglieber, and M.K. Oberthaler. Linear and nonlinear dynamics of matter wave packets in periodic potentials. *Optics Express*, 12(1):11–18, 2004.

[25] M. Greiner, O. Mandel, T. Esslinger, T. Hänsch, and I. Bloch. Quantum phase transition from a superfluid to a Mott insulator in a gas of ultracold atoms. *Nature*, 415:39–44, 2002.

[26] F.S. Cataliotti, S. Burger, C. Fort, P. Maddaloni, F. Minardi, A. Trombettoni, A. Smerzi, and M. Ingusio. Josephson junction arrays with Bose-Einstein condensates. *Science*, 293:843–46, 2001.

[27] Th. Anker, M. Albiez, R. Gati, S. Hunsmann, B. Eiermann, A. Trombettoni, and M.K. Oberthaler. Nonlinear self-trapping of matter waves in periodic potentials. *Physical Review Letters*, 94:020403, 2005.

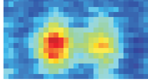

[28] J. Javanainen. Oscillatory exchange of atoms between traps containing Bose condensates. *Physical Review Letters*, 57:3164–3166, 1986.

[29] A. Smerzi, S. Fantoni, S. Giovanazzi, and S.R. Shenoy. Quantum coherent atomic tunneling between two trapped Bose-Einstein condensates. *Physical Review Letters*, 79:4950–4953, 1997.

[30] S. Raghavan, A. Smerzi, S. Fantoni, and S.R. Shenoy. Coherent oscillations between two weakly coupled Bose-Einstein condensates: Josephson effects, π oscillations, and macroscopic quantum self-trapping. *Physical Review A*, 59:620–633, 1999.

[31] G.J. Milburn, J. Corney, E.M. Wright, and D.F. Walls. Quantum dynamics of an atomic Bose-Einstein condensate in a double well potential. *Physical Review A*, 55:4318–4324, 1997.

[32] I. Zapata, F. Sols, and A.J. Leggett. Josephson effect between trapped Bose-Einstein condensates. *Physical Review A*, 57:R28–31, 1998.

[33] M.W. Jack, M.J. Collett, and D.F. Walls. Coherent quantum tunneling between two Bose-Einstein condensates. *Physical Review A*, 54:R4625–4628, 1996.

[34] I. Marino, S. Raghavan, S. Fantoni, S.R. Shenoy, and A. Smerzi. Bose-condensate tunneling dynamics: Momentum-shortened pendulum with damping. *Physical Review A*, 60:487, 1999.

[35] J. Williams, R. Walser, J. Cooper, E. Cornell, and M. Holland. Nonlinear Josephson-type oscillations of a driven, two-component Bose-Einstein condensate. *Physical Review A*, 59:R31–R34, 1999.

[36] D.S. Hall, M.R. Matthews, J.R. Ensher, C.E. Wieman, and E.A. Cornell. Dynamics of component separation in a binary mixture of Bose-Einstein condensates. *Physical Review Letters*, 81:1539, 1998.

[37] T.G. Tiecke, M. Kemmann, Ch. Buggle, I. Shvarchuck, W. von Klitzing, and J.T.M Walraven. Bose-Einstein condensation in a magnetic double-well potential. *J. Opt. B*, 5:119–123, 2003.

[38] Y. Shin, M. Saba, A. Schirotzek, T.A. Pasquini, A.E. Leanhardt, D.E. Pritchard, and W. Ketterle. Distillation of Bose-Einstein condensates in a double-well potential. *Physical Review Letters*, 92:150401, 2004.

[39] J. Estève, T. Schumm, J.-B. Trebbia, I. Bouchoule, A. Aspect, and C.I. Westbrook. Realizing a stable magnetic double-well potential on an atom chip. *arXiv:physics/0503112*, 2005.

[40] Y. Shin, M. Saba, T.A. Pasquini, W. Ketterle, D.E. Pritchard, and A.E. Leanhardt. Atom interferometry with Bose-Einstein condensates in a double-well potential. *Physical Review Letters*, 92:050405, 2004.

[41] S. Inouye, M.R. Andrews, J. Stenger, H.-J. Miesner, D.M. Stamper-Kurn, and W. Ketterle. Observation of Feshbach resonances in a Bose-Einstein condensate. *Nature*, 392:151, 1998.

[42] A. Marte, T. Volz, J. Schuster, S. Dürr, G. Rempe, E.G.M. van Kempen, and B.J. Verhaar. Feshbach resonances in rubidium 87: Precision measurement and analysis. *Physical Review Letters*, 89(28):283202, 2002.

[43] C.P. Poole, H.A. Farach, and R.J. Creswick. *Superconductivity*. Academic Press, San Diego, 1995.

[44] F. London. Macroscopic interpretation of superconductivity. *Proceedings of the Royal Society*, 152:23, 1935.

[45] V.L. Ginzburg and L.G. Landau. On the theory of superconductivity. *Zh. Eksp. Theor. Phys.*, 20:1064, 1950.

[46] J.R. Schrieffer, J. Bardeen, and L.N. Cooper. Theory of superconductivity. *Physical Review*, 108:1175, 1957.

[47] J. Clarke and A.I. Braginski. *The SQUID Handbook*, volume 1. Wiley-VCH, Berlin, 2004.

[48] M.P. Feynman. *Lectures on physics*, volume 3. Addison-Wesley, New York, 1965.

[49] W. Buckel and R. Kleiner. *Supraleitung*. Wiley-VCH, Weinheim, 2004.

[50] H. Ohta. A self-consistent model of the Josephson junction. *IC SQUID*, 76:35–49, 1976.

[51] V. Ambegaokar and A. Baratoff. Tunneling beween superconductors. *Physical Review Letters*, 10:486, 1963.

[52] W.C. Stewart. Current-voltage characteristics of Josephson junctions. *Applied Physics Letters*, 12:277, 1968.

[53] D.E. McCumber. Effect of ac impedance on dc voltage-current characteristics of superconductor weak-link. *Journal of Applied Physics*, 39:3113, 1968.

[54] T. van Duzer. *Principles of superconductive devices and circuits*. Elsevier, New York, 1981.

[55] M.H. Devoret, D. Esteve, and C. Urbina. Single-electron transfer in metallic nanostructures. *Nature*, 360:547, 1992.

[56] D.V. Averin and K.K. Likharev. Single electronics: A correlated transfer of single electrons and Cooper pairs in systems of small tunnel junctions. In B.L. Altshuler, P.A. Lee, and R.A. Webb, editors, *Mesoscopic phenomena in solids*, chapter 6. North-Holland, Amsterdam, 1991.

[57] T. Guénault. *Basic superfluids*. Taylor and Francis, London, 2003.

[58] A. Barone. Weakly coupled macroscopic quantum systems : likeness with difference. In I. O. Kulik and R. Ellialtioğlu, editors, *Quantum mesoscopic phenomena and mesoscopic devices in microelectronics*, volume 559 of *C*, chapter 20. Nato science series, Dordrecht, 1999.

[59] S. Pereverzev, A. Loshak, S. Backhaus, J. C. Davis, and R. E. Packard. Quantum oscillations between two weakly coupled reservoirs of superfluid ^{3}He. *Nature*, 388:449, 1997.

[60] S. Sukhatme, Y. Mukharsky, T. Chui, and D. Pearson. Observation of the ideal Josephson effect in superfluid ^{4}He. *Nature*, 411:280, 2001.

[61] S. Backhaus, S. Pereverzev, R. W. Simmonds, A. Loshak, J. C. Davis, and R. E. Packard. Discovery of a metastalble π-state in a superfluid ^{3}He weak link. *Nature*, 392:687, 1998.

[62] L.N. Bulaevskii, V.V. Kuzii, and A.A. Sobyanin. Superconducting system with weak coupling to the current in the ground state. *JETP Letters*, 25:290, 1977.

[63] D.J. Harlingen. Phase-sensitive tests of the symmetry of the pairing states in high-temperature superconductors: evidenve for $d_{x^2-y^2}$ symmetry. *Review of Modern Physics*, 67:515, 1997.

[64] W. Nolting. *Statistische Physik*. Verlag Zimmermann-Neufang, Ulmen, Germany, 1994.

[65] K. Huang. *Statistical Mechanics*. John Wiley, New York, 2nd edition, 1987.

[66] W. Ketterle, D.S. Durfee, and D.M. Stamper-Kurn. Making, probing and understanding Bose-Einstein condensates. In M. Inguscio, S. Stringari, and C. Wieman, editors, *Bose-Einstein Condensation in Atomic Gases*, Amsterdam: IOS Press, 1999. Società Italiana di Fisica.

[67] F. Dalfovo and S. Giorgini. Theory of Bose-Einstein condensation in trapped gases. *Review of Modern Physics*, 71(3):463–512, 1999.

[68] A.J. Leggett. Bose-Einstein condensation in the alkali gases: Some fundamental concepts. *Reviews of Modern Physics*, 73:307, 2001.

[69] E.P. Gross. Structure of a quantized vortex in boson systems. *Nuovo Cimento*, 20:454, 1961.

[70] E.P. Gross. Hydrodynamics of a superfluid condensate. *Jounal of Mathematical Physics*, 4:195, 1963.

[71] L.P. Pitaevskii. Vortex lines in an imperfect Bose gas. *Sov. Phys. JETP*, 13:451, 1961.

[72] M.L. Chiofalo and M.P. Tosi. Output from Bose condensates in tunnel arrays: the role of mean-field interactions and of transverse confinement. *Physics Letters A*, 268:406, 2000.

[73] L. Salasnich, A. Parola, and L. Reatto. Effective wave equations for the dynamics of cigar-shaped and disk-shaped Bose condensates. *Physical Review A*, 65(4):043614, 2002.

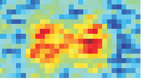

[74] B. Eiermann. *Kohärente nichtlineare Materienwellendynamik - Helle atomare Solitonen-*. PhD thesis, Universität Konstanz, 2004.

[75] E.A. Ostrovskaya, Y.S. Kivshar, M. Liesak, B. Hall, F. Cattani, and D. Anderson. Coupled-mode theory for Bose-Einstein condensates. *Physical Review A*, 61:R031601, 2000.

[76] S. Giovanazzi, A. Smerzi, and S. Fantoni. Josephson effects in dilute Bose-Einstein condensates. *Physical Review Letters*, 84:4521, 2000.

[77] J. Javanainen and M.J. Ivanov. Splitting a trap containing a Bose-Einstein condensate: Atom number fluctuations. *Physical Review A*, 60(3):2351, 1999.

[78] S. Raghavan, A. Smerzi, and V. M. Krenkre. Transitions in coherent oscillations between two trapped Bose-Einstein condensates. *Physical Review A*, 60:R1787, 1999.

[79] J. Ruostekoski and D.F. Walls. Bose-Einstein condensate in a double-well potential as an open quantum system. *Physical Review A*, 58:R50, 1998.

[80] D. Ananikian and T. Bergeman. The Gross-Pitaevskii equation for Bose particles in a double well potential: Two mode models and beyond. *arXiv:cond-mat/0503220*, 2005.

[81] D.T. Colbert and W.H. Miller. A novel discrete variable representation for quantum mechanical reactive scattering via the s-matrix Kohn method. *Journal of Chemical Physics*, 96:1982, 1992.

[82] C.W. Murray, S.C. Racine, and E.R. Davidson. Improved algorithms for the lowest few eigenvalues and associated eigenvectors of large matrices. *Journal of Computational Physics*, 103:382, 1992.

[83] C.J. Myatt, E.A. Burt, R.W. Ghrist, E.A. Cornell, and C.E. Wieman. Production of two overlapping Bose-Einstein condensates by sympathetic cooling. *Physical Review Letters*, 78:586, 1997.

[84] M.R. Matthews, D.S. Hall, D.S. Jin, J.R. Ensher, C.E. Wieman, and E.A. Cornell. Dynamical response of a Bose-Einstein condensate to a discontinuois change in internal state. *Physical Review Letters*, 81:243, 1998.

[85] D.S. Hall, M. Matthews, C.E. Wieman, and E.A. Cornell. Measurements of the relative phase in two component Bose-Einstein condensates. *Physical Review Letters*, 81:1543, 1998.

[86] G. Agrawal. *Nonlinear fiber optics*. Academic Press, San Diego, 2 edition, 1995.

[87] M.L. Chiofalo, S. Succi, and M.P. Tosi. Ground state of trapped interacting Bose-Einstein condensates by an explicit imaginary-time algorithm. *Physical Review E*, 62(5):7438–44, 2000.

[88] S. Hunsmann. Josephson-Effekte in Bose-Einstein Kondensaten. Diplomarbeit, Universität Heidelberg, 2004.

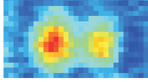

[89] K. Dieckmann, R.J.C. Spreeuw, M. Weidemüller, and J.T.M Walraven. Two-dimensional magneto-optical trap as a source of slow atoms. *Physical Review A*, 58(5):3891–95, 1998.

[90] E.L. Raab, M. Prentiss, A. Cable, S. Chu, and D.E. Pritchard. Trapping of neutral sodium atoms with radiation pressure. *Physical Review Letters*, 59(23):2631–34, 1987.

[91] E. Majorana. Atomi orientati in campo magnetico variabile. *Nuovo Cimento*, 9:43–50, 1932.

[92] D.E. Pritchard. Cooling neutral atoms in a magnetic trap for precision spectroscopy. *Physical Review Letters*, 51(15):1336–39, 1983.

[93] M.-O. Mewes, M.R. Andrews, N.J. van Druten, D.M. Kurn, D.S. Durfee, and W. Ketterle. Bose-Einstein condensation in a tightly confining dc magnetic trap. *Physical Review Letters*, 77(3):416–419, 1996.

[94] W. Petrich, M. Anderson, J. Ensher, and E. Cornell. Stable, tightly confining magnetic trap for evaporative cooling of neutral atoms. *Physical Review Letters*, 74(17):3352–55, 1995.

[95] C. Cohen-Tannoudji, J. Dupont-Roc, and G. Grynberg. *Atom-Photon Interactions*. Wiley-Interscience, New York, 1992.

[96] H.J. Metcalf and P. van der Straten. *Laser Cooling and Trapping*. Springer Verlag, 1999.

[97] D. Cassettari, B. Hessmo, R. Folman, T. Maier, and J. Schmiedmayer. Beam splitter for guided atoms. *Physical Review Letters*, 85:5483, 2000.

[98] J. W. Goodman. *Introduction to Fourier Optics*. McGraw-Hill, Boston, MA, 1998.

[99] E. Hecht. *Optics*. Addison-Wesley, Reading, MA, 1998.

[100] M. Albiez, R. Gati, J. Fölling, S. Hunsmann, C. Matteo, and M. K. Oberthaler. Direct observation of tunneling and nonlinear self-trapping in a single bosonic Josephson junction. *Physical Review Letters*, 95(010402), 2005.

[101] L. Pitaevskii and S. Stringari. Thermal vs. quantum decoherence in double well trapped Bose-Einstein condensates. *Physical Review Letters*, 87:180402, 2001.

[102] N. Ashcroft and N. Mermin. *Solid state physics*. Saunders College Publishing, 1976.

[103] G. Agrawal. *Applications of Nonlinear Fiber Optics*. Academic Press, San Diego, 2nd edition, 2001.

[104] A. Görlitz, J.M. Vogels, A.E. Leanhardt, C. Raman, T.L. Gustavson, J.R. Abo-Shaeer, A.P. Chikkatur, S. Gupta, S. Inouye, T.P. Rosenband, D.E. Pritchard, and W. Ketterle. Realization of Bose-Einstein condensates in lower dimensions. *Physical Review Letters*, 87(13):130402, 2001.

[105] V. Ahufinger, A. Sanpera, P Pedri, L. Santos, and M. Lewenstein. Creation and mobility of discrete solitons in Bose-Einstein condensates. *Physical Review A*, 69:053604, 2004.

[106] A. Trombettoni and A. Smerzi. Discrete solitons and breathers with dilute Bose-Einstein condensates. *Physical Review Letters*, 86(11):2353–56, 2001.

[107] L. Salasnich. Parametric resonant phenomena in Bose-Einstein condensates: Breaking of quantum self-trapping. *arXiv:cond-mat/0208221*, 2002.

[108] A.I. Streltsov and L.S. Cederbaum. Properties of fragmented repulsive condensates. *arXiv:cond-mat/0412222*, 2004.

[109] A.I. Streltsov, L.S. Cederbaum, and N. Moiseyev. Ground-state fragmentation of repulsive Bose-Einstein condensates in double-trap potentials. *Physical Review A*, 70:053607, 2004.

[110] M. Taglieber. Helle atomare Gap-Solitonen. Diplomarbeit, Universität Konstanz, Oktober 2003.

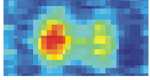

Acknowledgements

During the realization of the presented work, I was collaborating and getting help from many colleagues and friends. To these people I would like to say "thank you":

- I am deeply grateful to my supervisor Markus Oberthaler for his guidance and support throughout my PhD period. Markus is not only an excellent scientist who shared with me his enthusiasm for physics, but also a compassionate human with a concern for my family situation. This was the basis for having a great time in his group. Thanks for everything, Markus!

- Together with Bernd Eiermann and Thomas Anker, who already worked on the experiment when I arrived, I have spent innumerable enjoyable (and from time to time successful) hours in the lab in Konstanz and Heidelberg. Bernd's attention to details, his patience in explaining physical details and helping whenever he was asked for, have made him an invaluable partner. Tom, a brilliant scientist and dancing machine, has always taken care of the suitable music in the lab. We had a lot of fun (not only with physics)! Both of them have continued to contribute to my intellectual and personal development. I am grateful for their friendship!

  After the move to Heidelberg, Rudolf Gati, an excellent scientist and a great asset to the lab, joined our experiment. He made big contributions to the success of the Josephson junction experiments and got never tired during the "datathlon". I wish him all the best for the rest of his PhD period. "Mille grazie" to Matteo Cristiani, who worked in our lab during the first three months spent on the Josephson junction experiment. He is a truly brilliant guy and has been a great source of knowledge and ideas.

- Special mention and thanks go to our diploma students Jonas Fölling, Börge Hemmerling, Stefan Hunsmann, Matthias Taglieber and Philipp Treutlein for their substantial contributions to the success of the experiment. I enjoyed sharing the lab and office, and discussing physical and private problems with great people.

- I also want to thank the other group members who are or were working on other projects: Ramona Ettig, Alex Greiner, Martin Göbel, Anja Habenicht, Thomas Hörner, Igor Mourachko, Dirk Jürgens, Lisa Kierig, Martin Störzer and Ralf Stützle. They contributed substantially to the great atmosphere in the group and to many enjoyable hours during the coffee breaks and the numerous pub-crawls.

- The department of physics of the universities of Konstanz and Heidelberg, who have provided an excellent professional environment for my research.

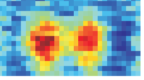

- I would like to thank my parents, my grandparents and my brother for their unconditional never-ending support.
- Finally, I would like to thank my wonderful wife Karen, who performs the most challenging job of taking care of our daughters Clara and Luca. It is through their love, support and encouragement that I have made it through all the steps during the last ten years to reach this point in life.